UNIVERSITÀ DEGLI STUDI DI PARMA

FACOLTÀ DI SCIENZE MATEMATICHE FISICHE E NATURALI

DOTTORATO IN SCIENZA E TECNOLOGIA
DEI MATERIALI INNOVATIVI

XXII CICLO

Cooperativity from charge transfer, phonons and electrostatic interactions in functional molecular materials

Coordinatore: Prof. Anna Painelli

Tutor: Prof. Anna Painelli

Candidato: Gabriele D'Avino

gabriele.davino@gmail.com
Printed in Parma on January 2010

Contents

List of Abbreviations

CT	charge transfer
D/A	(electron) donor/acceptor
N/I	neutral/ionic
NIT	neutral to ionic phase transition
(DM)TTF-CA	(4,4'-dimethyl-)tetrathiafulvalene-chloranil
1D/3D	one/three dimensional
ph/e-ph	phonon/electron-ph
mv/e-mv	molecular vibration/electron-mv
mf	mean field
PES	potential energy surface
IR	infrared
MD	molecular dynamics
TCF	time correlation functions
DXR	diffuse X-ray
MH	modified Hubbard
SF	spinless fermion
BBP	bond-bond polarizability
Fc-PTM	ferrocene-perchlorotriphenylmethyl
Me_9Fc-PTM	nonamethyl-Fc-PTM
SC	spin crossover

General Introduction

The discovery of novel materials with new properties and functionalities has triggered along the centuries the transformation and innovation of the society. The information society we belong to has his roots in the development of the materials for electronics, a field largely dominated by silicon, but where magnetic materials for information storage and optical materials for communications also play an important role. At the same time, the development of chemical synthesis produced an enormous increase of available materials: plastic materials indeed profoundly changed our lifestyle. Traditionally, the research in the fields of materials for electronics (and more recently photonics and spintronics) and on chemical synthesis occurred along parallel tracks. Combining the functionalities of materials for advanced applications with the performances of plastic materials will provide brand new materials opening new technological scenarios. Molecular materials for advanced applications are therefore a very active field of research, stimulated by the possibility to replace traditional functional materials with low-cost molecular-based materials. [1, 2, 3, 4, 5, 6, 7] Moreover, the complexity of molecular systems opens the way to a wide variety of new and multiple functionalities. The fine tuning of the material properties, made possible by chemical synthesis, has no counterpart in the traditional and mature field of silicon-based materials for electronics.

To fully exploit the promise of molecular functional materials, the physics

that governs their complex behavior must be thoroughly understood, with the aim, on one side, to optimize the materials for current needs, on the other side to guide the synthesis of new materials showing brand new behaviors. This thesis represents an effort towards the definition of general models for molecular functional materials. Microscopic quantum mechanical models are developed and applied to investigate the essential physics governing the complex behavior of molecular functional materials. Switchable molecular materials, i.e. systems whose properties can be tuned by applying external stimuli, are the main target. The possibility to switch between two or more stable states is an essential requirement for the realization of intelligent devices, and functional molecular materials are in demand for the realization of ultra-small and ultra-fast switches, whose properties can be controlled by a variety of external stimuli, as temperature, pressure, electric and/or magnetic fields, or, by shading light. [8, 6, 2, 9, 10, 11, 12] The fields of application of switchable molecular materials, include, just to cite a few examples, information storage, photonics, sensoristics, molecular electronics and spintronics. Entering the specific of this thesis, the research activity is mainly focused on the cooperative effects originated from charge transfer (CT), phonons (molecular and lattice vibrations) and electrostatic interactions in mixed stack CT crystals (chapter 1), crystals of valence tautomeric molecules (chapter 2) and spin crossover (SC) complexes (chapter 3).

Bistability, or more generally multistability, is a rare phenomenon that results from a delicate balance of competing interactions. Understanding multistability in molecular materials requires a comprehensive picture of the physics both at the molecular and at the supramolecular scale. Multistability represents the extreme manifestation of nonlinear behavior induced in molecular materials by cooperative interactions. The molecular prerequisite for bi/multistability is the accessibility of two or more different molecular

states. At the molecular level this multistability often results in interesting equilibrium phenomena that can be affected and driven by external stimuli. This is the case of SC complexes and valence tautomeric molecules. In the first case, two stable states are accessible to a metal ion in a ligand field. [13, 14] The two states, corresponding to a low and a high spin electronic configuration, are characterized by different geometries with a sizable variation of the metal-ligand distance. In solution or in solids with weak intermolecular interactions SC complexes equilibrate between the two forms, with different optical and magnetic properties, and the equilibrium is affected by temperature, pressure, light and magnetic fields. In valence tautomeric molecules, instead, the low energy physics is governed by charge resonance between two mesomeric forms, characterized by different charge and spin distribution. Among valence tautomers, DA-based molecules have recently attracted much interest for applications in nonlinear optics [7] and molecular electronics. [15] In these molecules an electron donor (D) and an electron acceptor (A) groups are connected by a π-conjugated bridge. The presence of metallic centers and/or unpaired spins make some of these molecules interesting for magnetic applications and promising candidates for applications in spintronics and quantum computing.

In the lack of cooperative interactions, the exchange between the two (or more) stable molecular states is fast and molecular multistability is not immediately interesting for applications. [11, 16, 11, 17, 18, 19]. Cooperative intermolecular interactions can stabilize higher energy states and, what is more important, can provide kinetic barriers, leading to true bistability (or multistability) in the solid state or, more generally, in meso and macroscopic systems. In truly multistable systems, the interconversion between the stable forms is a slow process, implying the *simultaneous* change of state of a large number of molecules. Bistability always accompanies first order phase transitions and manifests itself in hysteresis loops and/or with the ap-

pearance of coexisting phases. Most interestingly, bistability opens the way to the photoswitching of (meta)stable phases. Photoinduced phase transitions are a clear manifestation of cooperativity in nonequilibrium cascading processes following light absorption. [8]

Multistability in molecular materials can be driven by intermolecular interactions of different kinds. In SC materials, elastic interactions, related to the variation of the molecular size accompanying the spin transition, are the primary cause of cooperativity and are responsible for the appearance of temperature and/or pressure induced first order transitions as well as of photoinduced transitions. A wide variety of SC complexes has been synthesized and characterized showing different properties an behavior. Systems are known showing abrupt transitions, wide hysteresis loops as well as multi-step transitions. In all cases the entanglement between spin degrees of freedom, molecular and lattice vibrations results in a complex cooperative behavior. Valence tautomeric molecules are also good candidates for bistability, driven in this case by the coupling between intramolecular CT and intermolecular electrostatic interactions. Bistability in clusters of valence tautomeric molecules has been theoretically predicted a few years ago in the guest laboratory. [20] In this thesis, the coexistence of two valence tautomers in crystals of ferrocene-perchlorotriphenylmethyl radical (Fc-PTM), an interesting ferrocene-based chromophore, is quantitatively explained in terms of bistability induced by electrostatic intermolecular interactions, offering the first experimental confirmation of the proposed phenomenon.

Multistability in mixed-stack CT crystals has a different, but not unrelated source. In mixed-stack CT crystals planar D and A molecules pack together forming one dimensional stacks with an alternating pattern (. . . DADA . . .). Here the D and A units are distinct molecules whose frontier orbitals overlap to give a system where electrons are delocalized in one spatial dimension. The interplay between the intermolecular CT, electrostatic interac-

tions, lattice phonons and molecular vibrations drives the the so called neutral to ionic phase transitions (NIT), a collective electron transfer from D to A molecules, that is always accompanied by lattice dimerization. NIT can be induced by decreasing temperature and/or applying pressure and, together with SC system, represents one of the most studied photoinduced transitions. [8] Mixed stack CT crystals present a rich phase diagram and phenomenology that include charge ordering, band and Mott-insulating phases, lattice (Peierls and spin-Peierls) instabilities. These systems offer an almost unique opportunity to study, in a reasonably simple system, the coupling between phonons and strongly correlated electrons in 1D and the related charge and spin instabilities. It is worth mentioning that NIT represents one of the few example of ferroelectric transitions in purely organic materials, [2] and the mixed stack CT salts tetratiafulvalene-chloranil (TTF-CA) has been recently recognized as the first organic multiferroic. [21].

This thesis is organized as follows. Chapter 1 is devoted to NIT in mixed stack CT crystals and presents the two contributions offered by this work in the field. In particular section 1.4 reports on the simulation of vibrational (infrared and Raman) spectra of a system undergoing NIT. The spectra are calculated as Fourier transforms of the time autocorrelation functions of the stack polarization and polarizability, quantities that in turn are obtained exploiting the modern theory of polarization in dielectrics. This approach fully accounts for the strong anharmonicity arising in the system from electron-phonon coupling and explains several anomalies observed in the vibrational spectra of mixed stack CT crystals, including new and interesting data obtained in the guest laboratory. Section 1.5 describes a work done in collaboration with Z. G. Soos (Princeton University) and M. H. Lemée-Cailleaux (ILL Grenoble) on the lattice dynamics in mixed stacks. We discuss the development at NIT of a Kohn-like anomaly in the optical phonon branch due to the softening of the Peierls or dimerization mode. This Kohn-like

anomaly and its surprisingly strong dispersion explains the diffuse X-ray signal experimentally observed in the pretransitional regime for two specific systems.

Chapter 2 is devoted to the bistability induced by electrostatic interactions in crystals of valence tautomeric molecules and specifically in Fc-PTM crystals. This work, in collaboration with the group of J. Veciana (ICMAB-CSIC Barcelona) starts with a detailed analysis of optical spectra of Fc-PTM in solution based on essential state models. In a bottom up modeling strategy, we use this information to build a model for Fc-PTM crystals where electrostatic interactions are implemented with the support of quantum chemical calculations. On this basis the temperature dependent valence tautomerism, revealed in Fc-PTM crystals by Mössbauer spectra, is quantitatively explained in terms of bistability induced by electrostatic intermolecular interactions. In the process, the development of two and three state models for Fc-PTM and a related compound shed light on some long-standing problems in the spectroscopic characterization of DA chromophores.

Finally, chapter 3 presents the work done on SC complexes, developed in collaboration with K. Boukheddaden and F. Varret, during a three months stay (April-June 2009) at the University of Versailles (UVSQ). The main target of this work is the development of a microscopic model for SC molecules, accounting for the coupling between the electronic (spin) state and an effective molecular vibration. Exact and adiabatic solutions of the vibronic problem are thoroughly discussed for a physically meaningful set of parameters. The molecular model is then applied to describe intermolecular interactions in SC crystals. Different phenomenological interaction terms, treated within the mean field approximation, are finally considered.

Chapter 1

Neutral-Ionic phase transition in mixed stack charge transfer crystals

1.1 Introduction: NIT in mixed stack CT crystals

Charge transfer (CT) crystals (or salts) are an important class of organic molecular materials constituted by almost planar π-conjugated electron donor (D) and electron acceptor (A) molecules. [22] Some representative examples of D and A molecules are given in figure 1.1. These planar π-conjugated molecules pack face to face forming one dimensional (1D) stacks. Intermolecular distances along the stack imply sizeable overlap between frontiers orbitals on adjacent molecules, and electrons easily hop within the stack. The interactions between molecules belonging to different stacks, are characterized by larger distances and interstack overlap is negligible. Electrons are therefore truly delocalized in 1D and different stacks interact mainly via electrostatic interactions and, in some cases, via site-selective interactions

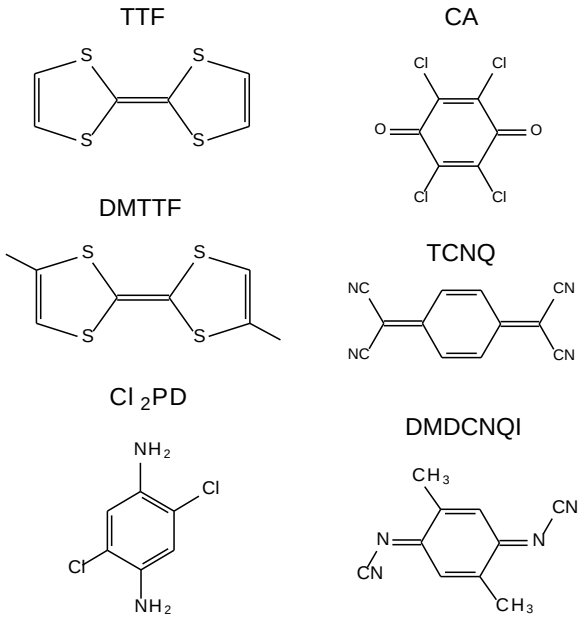

Figure 1.1: Molecular structure of some D (left column) and A (right column) molecules used in CT crystals.

(hydrogen bonding, etc.). As for conjugated polymers, CT crystals represent an experimental realization of an almost-1D system, whose physics, governed by the interplay between electronic correlations and electron-phonon (e-ph) coupling, results in rich and interesting phase diagrams. Different stacking of D and A molecules are possible and CT crystals are conveniently classified as segregated stack CT crystals, where each stack is made up by the same molecule (either ...DDDD... or ...AAAA...) and mixed-stack CT crystals in which D and A molecules alternate on the same stack (...DADA...). [22] In the present work we will concentrate on mixed stack systems.

In mixed stack systems the overlap between frontier orbitals of adjacent molecules causes a CT from D to A, resulting in a fractional molecular ionicity, ρ, so that the stack can be represented as $\ldots \mathrm{D}^{+\rho}\mathrm{A}^{-\rho}\mathrm{D}^{+\rho}\mathrm{A}^{-\rho}\ldots$. The large majority of CT crystals are neutral (N, $\rho \lesssim 0.5$) but a few examples of ionic (I, $\rho \gtrsim 0.5$) systems are known. [23] As originally recognized by Mc Connell [24] the N or I nature of CT crystals depends on the balance between the ionization energy of a DA pair, $I_D - E_A$ (I_D is the ionization potential of the D and E_A the electron affinity of the A), and the electrostatic energy of the ionic lattice, i.e. the Madelung energy M. N crystals are expected for $I_D - E_A > M$, I salts for $I_D - E_A < M$. More interesting are systems where $I_D - E_A \approx M$, where the N-I boundary can be crossed by varying external conditions, realizing the neutral-ionic phase transition (NIT), i.e. a collective electron transfer from D to A sites, as sketched in figure 1.2. NIT is a quantum phase transition that results from the increase of the Madelung energy due to lattice contractions with increasing pressure or decreasing temperature. A brilliant proof of the quantum nature of the NIT was given by Horiuchi *et al.* that, by mean of external pressure and chemical substitution, were able to shift the transition toward zero temperature. [25]. The first observations of pressure and temperature induced NITs were reported for tetratiafulvalene-chloranil (TTF-CA, see figure 1.1) by Torrance

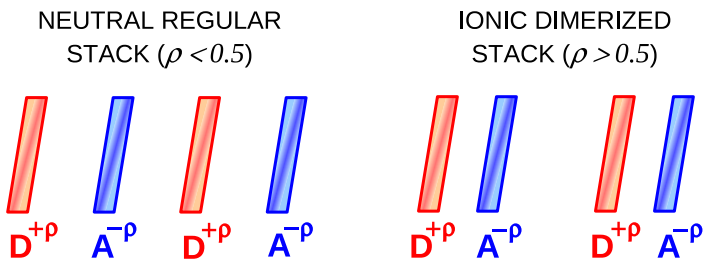

Figure 1.2: A schematic representation of the N regular phase (high temperature/low pressure) and of the I dimerized phase (low temperature/high pressure). The amplitude of dimerization is magnified for clarity.

et al. in 1981 [26, 27]. The left panel of figure 1.3 shows the temperature dependence of the ionicity in TTF-CA, the prototypical and best characterized NIT system. The stack ionicity is estimated spectroscopically from the frequency of the infrared active carbonyl antisymmetric stretching of the CA molecule, which is very sensitive to the molecular charge. At room temperature TTF-CA is largely N ($\rho \sim 0.2$). The ionicity ρ slightly increase upon cooling down to 81 K where a discontinuous jump from $\rho \sim 0.3$ to $\rho \sim 0.5$ occurs. Further cooling increases ρ up to ~ 0.6.

As sketched in figure 1.2 the charge reorganization at NIT is always accompanied by a dimerization of the stack. Dimerization is related to a generalized Peierls instability, due to the coupling of the lattice to both charge (Peierls instability of 1D metals) and spin (spin-Peierls instability of $S = 1/2$ Heisenberg chains) degrees of freedom. Stack dimerization is concomitant with the electronic transition in discontinuous NITs, as occurs in TTF-CA, and defines the critical point of continuous transitions, as relevant for dimethyl-TTF-CA (DMTTF-CA, see figure 1.1). Strictly speaking DMTTF-CA, whose $\rho(T)$ characteristics is reported in the right panel of figure 1.3, does not undergo a true NIT because the ionicity is always lower

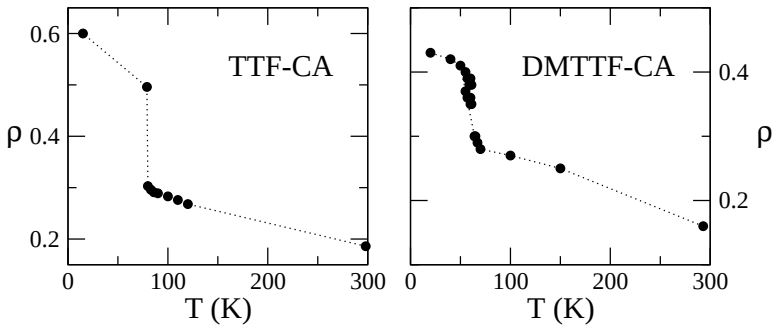

Figure 1.3: Temperature dependence of the ionicity ρ in TTF-CA and DMTTF-CA. Black circles are the value of ρ estimated from the frequency of the carbonyl stretching, dotted lines are guide for the eyes.

that the conventional value $\rho = 0.5$. In fact the transition of DMTTF-CA is more similar to a Peierls transition, occurring at $T = 65\ K$, accompanied by a steep continuous variation of the ionicity [28]. In any case stack dimerization lowers the symmetry, removing the inversion center residing on each molecule, so that the I dimerized stack is ferroelectric. However, such 1D ferroelectricity does not necessarily results in a ferroelectric material, that requires a 3D ordering of polarized chains. In fact, while the I phase of TTF-CA is ferroelectric, the corresponding phase of DMTTF-CA shows an antiferroelectric (or weakly ferrielectric) mutual arrangement of the stacks.

The NIT in mixed stack CT crystals represents one of the most impressive examples of cooperative phenomena in organic solid state physics. Although the scenario of NIT is complex and characterized by a rich phenomenology, a coherent picture of the physics governing the transition is emerging. This chapter of the thesis reports the last steps in this direction. In the following section an overview of the models and methods adopted to describe NIT is given, while a comprehensive experimental and theoretical background about the transition is provided in section 1.3. The specific contributions of

this thesis are described in section 1.4, with the calculation of vibrational spectra of a NIT system, and in section 1.5, that discusses the effects of electron-phonon coupling on the lattice dynamics and its consequences on the diffuse X-ray signal. Conclusions and future perspectives are drawn in section 1.6.

1.2 Models, methods and approximations

1.2.1 The modified Hubbard model

The standard microscopic model for the electronic structure of mixed stack CT crystals is a half filled 1D modified Hubbard model with 3D Coulomb interactions. [29, 30, 31, 32, 33] Alternating on-site energies $\pm\Delta$ account for the energy difference between the highest occupied molecular orbital for the D (odd sites) and the lowest unoccupied orbital for the A (even sites). The electronic Hamiltonian reads

$$\begin{aligned} H_{el} = \Delta \sum_i (-1)^i \ \hat{n}_i \ + \ \frac{U}{2} \sum_i \hat{n}_i(\hat{n}_i - 1) \\ - \sum_{i,\sigma} t_i \left(a^\dagger_{i,\sigma} a_{i+1,\sigma} + H.c. \right) \ + \ \sum_{i,j} V_{ij} \ \hat{\rho}_i \hat{\rho}_j \end{aligned} \tag{1.1}$$

where $\hat{n}_i$ counts the electrons on site i, U is the electron-electron on-site repulsion term, the operator $a^\dagger_{i,\sigma}$ ($a_{i,\sigma}$) creates (annihilates) an electron with spin σ in the i-th site and t_i is the hopping integral between adjacent sites. The last term accounts for electrostatic interactions: the operator $\hat{\rho}_i$, defined as $\hat{\rho}_i = 2 - \hat{n}_i$ on odd (D) sites and $\hat{\rho}_i = \hat{n}_i$ on even (A) sites, measures the molecular charge and V_{ij} is the electrostatic interaction energy between fully ionic ($\rho = 1$) molecules on sites i and j. It is worth noting that the index i runs on the N sites of the stack, while j runs over all the sites of the crystal. The average charge transferred from D to A is measured by the ionicity operator

$$\hat{\rho} = \frac{1}{N} \sum_i \hat{\rho}_i \tag{1.2}$$

The energetic cost of doubly ionized $D^{2+}A^{2-}$ pairs is very large so that the corresponding states give a negligible contribution to the low energy properties of the system. Doubly ionized states can be excluded by imposing a finite $\Gamma = \Delta - U/2$ and taking the limit $U, \Delta \to \infty$. Within this well

established approximation, [34] doubly ionized states have infinite energy and the Hamiltonian becomes:

$$H_{el} = \Gamma \sum_i (-1)^i \ \hat{n}_i + \sum_{i,\sigma} t_i \left(a^\dagger_{i,\sigma} a_{i+1,\sigma} + \ H.c. \right) + \sum_{i,j} V_{ij} \ \hat{\rho}_i \hat{\rho}_j \quad (1.3)$$

where 2Γ represent the energy required to ionize a DA pair and implicitly accounts for the energy difference between D and A orbitals and for on-site electronic repulsion.

In the absence of Coulomb interactions ($V_{ij} = 0$) the Hamiltonian (1.3) describes a continuous NIT upon decreasing Γ. Although ρ varies smoothly from 0 to 1 with decreasing Γ, a true quantum phase transition takes place at $\Gamma_c = -0.666$. The N and I phases can in fact be identified due to their different excitation spectrum. The N phase ($\Gamma > \Gamma_c$, $\rho < 0.686$) is a diamagnetic band insulator presenting finite charge and spin gaps, while in the I phase ($\Gamma < \Gamma_c$, $\rho > 0.686$) the spin gap vanishes. The I phase describes a paramagnetic Mott insulator phase and in the $\Gamma \to -\infty$ limit the system reduces to a Heisenberg $S = 1/2$ antiferromagnet. [35, 21] At the critical point the system presents a metallic state, in which both charge and spin gap vanishes. [36] Coulomb interactions qualitatively affect the nature of the transition, leading to discontinuous N-I crossover. [33, 37]

1.2.2 From 3D to 1D: mean field treatment of electrostatic interactions

Three dimensional electrostatic interactions are very important, since NIT is driven by the increase of the Madelung energy. However treating correlated electrons in 3D is a hard task. On the other hand mixed stack CT crystals present delocalized electrons in 1D and both theoretical and experimental evidences strongly support the view that the basic physics of NIT is governed by the interaction between correlated electrons and phonons in 1D. Hamiltonian (1.3) describes electron delocalized along the stack, interacting

via electrostatic interactions with electrons on different sites on the same and on different stacks. To maintain the problem tractable, interstack electrostatic interactions must be treated in the mean field (mf) approximation, factorizing the problem into single stacks. [33, 37] The resulting Hamilonian has the same form of (1.3), but with both i and j indexes running on a single chain and with a renormalized Γ parameter, that self-consistently depends on the ground state ρ. [37] Correlated electrons in 1D can be treated exactly with real space diagonalization techniques (see section 1.2.4) by explicitly accounting for intrastack electrostatic interactions. Exact diagonalizations on single stack have already been discussed [33, 38] and show that the mf approximation works well for intrastack electrostatic interactions. Here intrastack electrostatic interactions are conveniently splitted in two parts. [37] A first term $\sum_{i,odd} \hat{\rho}_i \ \hat{\rho}_{i+1}$, corresponding to the intra dimer interactions, is treated exactly. This term simply enters the Hamiltonian with a renormalization of the ionization energy, i.e. $\Gamma \rightarrow \Gamma - V/2$, where V is the nearest neighbors electrostatic interaction. The remaining electrostatic interactions are included in the mf treatment leading to the Hamiltonian [38, 37]

$$H = (\Gamma - V/2 - \varepsilon_c \rho) \sum_i (-1)^i \ \hat{n}_i - \sum_{i,\sigma} t_i \left(a^\dagger_{i,\sigma} a_{i+1,\sigma} + \ H.c. \right) + \frac{N}{2} \varepsilon_c \rho^2 \ - \ N \varepsilon_c \rho \tag{1.4}$$

where $\varepsilon_c = V(\mathcal{M} - 1)$ and $\mathcal{M}V = \sum_j V_{ij}$ measures the Madelung energy. While V fixes the scale of electrostatic interactions, $\mathcal{M}V$ measures the overall strength of 3D interactions. Within this mf treatment, electrostatic interactions enters the Hamiltonian as a self consistent renormalization of the ionization energy Γ.

1.2.3 Electron-phonon coupling

Lattice phonons and molecular vibrations play a fundamental role in the NIT and must be included in the picture. Hereafter we will focus on a sin-

gle stack, in the hypothesis that the physics of NIT is well described in 1D. Lattice phonons are needed to rationalize the stack dimerization that always accompanies NIT. To describe lattice phonons, we introduce a set of cartesian vibrational coordinates x_i, measuring the displacement along the stack direction of the i-th site from its equilibrium position in the regular chain. The coupling to the electronic system arises from the modulation of the hopping integrals due to the variation of the distance between adjacent sites. Following Su, Schrieffer and Heeger [4, 39] a linear coupling is considered

$$t_i = t_0 + \gamma(x_i - x_{i+1}) \tag{1.5}$$

where γ is the coupling constant. In the following t_0 will be used as energy unit. Out of the N longitudinal vibrational degrees of freedom, the optical mode at Brillouin zone center plays a special role, as it corresponds to the Peierls mode:

$$x_P = \frac{1}{\sqrt{N}} \sum_i (-1)^i x_i \tag{1.6}$$

The Peierls coordinate x_P measures the relative shift of D and A sublattices and drives the stack dimerization. The Peierls or dimerization mode is the more strongly coupled lattice mode and, as a Brillouin-zone center mode, is optically active. In many cases the relevant physics of NIT can be described by explicitly accounting for just x_P out of the N longitudinal modes. In the adiabatic approximation the Hamiltonian accounting for Peierls coupling reads

$$\begin{aligned} H \;=\; & (\Gamma - V/2 - \varepsilon_c\rho) \sum_i (-1)^i \; \hat{n}_i - \sum_{i,\sigma} \left[1 + (-1)^i \delta\right] \left(a^\dagger_{i,\sigma} a_{i+1,\sigma} + \; H.c. \right) \\ & + \; \frac{N}{2} \varepsilon_c \rho^2 \; - \; N \varepsilon_c \rho + \; \frac{N}{2\varepsilon_d} \delta^2 \end{aligned} \tag{1.7}$$

where $\delta = (2\gamma/\sqrt{N}) x_P$ is the dimensionless dimerization amplitude, $\varepsilon_d = \gamma^2/K$ is the lattice relaxation energy, a measure the strength of e-ph coupling, and K is the harmonic force constant of the lattice. [40] Peierls

coupling provides also a way to distinguish between N and I phases: the N phase is conditionally stable with respect to dimerization, the I phase is unconditionally unstable. [32]

Totally symmetric molecular vibrations (mv) couple to the electronic system trough a modulation of on-site energies, originated in the relaxation of molecular geometry upon ionization. [33] The mode driving the charge instability is also in this case a Brillouin-zone center mode, corresponding to the in-phase vibration of the molecules of one of the two (D or A) sublattices. A linear dependence on the mv coordinate of the DA ionization energy (Holstein coupling) is assumed. The electronic adiabatic Hamiltonian, including Peierls and Holstein coupling reads

$$H = (\Gamma + q - V/2 - \varepsilon_c\rho)\sum_i (-1)^i \hat{n}_i - \sum_{i,\sigma}\left[1 + (-1)^i\delta\right]\left(a^\dagger_{i,\sigma}a_{i+1,\sigma} + \ H.c.\right) + \frac{N}{2}\varepsilon_c\rho^2 \ - \ N\varepsilon_c\rho + \ \frac{N}{2\varepsilon_d}\delta^2 + \ \frac{N}{2\varepsilon_{sp}}q^2 \tag{1.8}$$

where q is the mv dimensionless coordinate with characteristic relaxation energy ε_{sp}.

1.2.4 Diagrammatic valence bond method

The modified Hubbard Hamiltonian presented in the previous sections is studied via real space diagonalizations on clusters of N sites, varying N in order to extrapolate the behavior in the thermodynamic limit. Born-Von Karman periodic boundary conditions (PBC) are imposed to minimize end effects. The real space technique that we use is called diagrammatic valence bond (DVB), a specific implementation of the valence bond method developed by Soos and Ramasesha. [41, 42] In a generic real space approach the Hamiltonian is represented on a basis set constituted by all possible configurations of N electrons on N sites, leading to a basis dimension of roughly increasing as 4^N. The exponential growth of the dimension of the

basis makes impossible to treat systems with large N. The DVB basis is obtained from the full real space basis, combining the functions to obtain the eigenstates of the (squared) total spin operator $\hat{S}^2$ and of its z-axis projection $\hat{S}_z$. Following Pauling, singlet wavefunctions are expressed as the product of wavefunctions of singlet-coupled electrons lying on the same or in different sites and have a clear and intuitive graphical representation, the DVB diagrams. [41, 42] The choice of the DVB basis is particularly convenient for our purposes because the Hubbard Hamiltonian conserves the total spin and the ground state of the systems is always a singlet. A drastic reduction of the dimension of the basis set is therefore obtained working in the $S^2 = S_z = 0$ subspace.

A further reduction of the basis set is obtained working in the high correlation limit (see section 1.2.1). In fact in this limit the diagrams with doubly ionized DA pairs present infinite energy and can be eliminated from the basis set. Moreover the rotational symmetry of finite size rings has been exploited to obtain a further factorization of the problem.

The DVB diagrams form a complete but not orthogonal basis set. To overcome this problem, the eigenfunctions of the Hamiltonian H are expressed as linear combinations of the DVB diagrams

$$\psi_n = \sum_k c_{kn} \; |k\rangle \tag{1.9}$$

and a matrix h is introduced, whose elements h_{kj} are defined as follows:

$$H|k\rangle = \sum_i h_{kj} \; |j\rangle \tag{1.10}$$

The matrix h provide a unsymmetrical but sparse representation of the original Hamiltonian H. h has the same eigenvalues of H and its left eigenvectors correspond to the coefficients c_{kn} in equation (1.9). [41, 42] We therefore work with the matrix h to exploit the advantages due to its sparse nature. Diagonalization of sparse and non symmetric matrix is efficiently performed

using the Rettrup algorithm, to obtain the ground state and eventually few excited states. [43]

Expectation values of a generic operator $\hat{A}$ are calculated as follows

$$\langle \hat{A} \rangle_n = \frac{\langle \psi_n | \hat{A} | \psi_n \rangle}{\langle \psi_n | \psi_n \rangle} = \frac{\sum_{k,j} c^*_{jn} c_{kn} \ \langle j | \hat{A} | k \rangle}{\sum_{k,j} c^*_{jn} c_{kn} \ \langle j | k \rangle} = \frac{\sum_{k,j} c^*_{jn} c_{kn} \ A_{jk}}{\sum_{k,j} c^*_{jn} c_{kn} \ S_{jk}} \tag{1.11}$$

where $S_{jk} = \langle j | k \rangle$ are the elements of the symmetrical overlap matrix. The overlap matrix is necessary since we are dealing with a non orthogonal basis and enters also in the calculation of A_{jk} in equation (1.11). In the common case of an operator diagonal on the DVB basis one obtains

$$A_{jk} = \langle j | \hat{A} | k \rangle = \langle j | \sum_l A_l | l \rangle = \sum_l A_l \ S_{jl} \tag{1.12}$$

1.2.5 Polarization and Polarizability in rings

As it will be discussed in section 1.4, the simulation of IR and Raman spectra requires the calculation of the electric polarization P and polarizability α. The definition of P and α is not trivial, because the dipole moment operator is not compatible with PBC, and only in recent times a theoretical framework for the calculation of these quantities has been developed. [44, 45, 38] In the modern theory of polarization in insulators P is formulated as a Berry phase [44]:

$$P = \frac{1}{\pi} \ \mathrm{Im} \left[\ln \langle \psi | \ \exp \left(i \frac{2\pi \hat{M}}{N} \right) \ | \psi \rangle \right] = \frac{1}{\pi} \ \mathrm{Im} [\ln(Z)] \tag{1.13}$$

where ψ is the ground state wavefunction and $\hat{M}$ is the open-chain dipole moment operator

$$\hat{M} = \sum_j \ j(-1)^{j+1} \ \hat{\rho}_j \tag{1.14}$$

expressed in units with $e = 1$ and $a = 1$, where e is the electronic charge and a is the intermolecular distance. P in equation (1.13) is expressed in ea

units per DA pair. In this formulation, P is not related to the amplitude of the wavefunction (charge density), but rather to its phase (current). P is not a true observable, its absolute value has no physical meaning and only its variation are relevant. Notice that the definition of $\hat{M}$ in equation (1.14) strictly applies to a regular chain. It possible to account for different spacings in dimerized stack by slightly modifying equation (1.14), but this will lead to more complex expressions without significantly altering the results. [38]

The polarizability is defined as the first derivative of P with respect to a static electric field F

$$\alpha = \left(\frac{\partial P(F)}{\partial F} \right)_{F=0} \tag{1.15}$$

Much as with P, in systems with PBC the polarizability cannot be evaluated using the standard approaches because, without an explicit expression for the dipole moment operator, the Hamiltonian in the presence of an electric field is not defined. The problem has been overcome trough the definition of the wavefunction in the presence of an electric field ψ_F as the wavefunction that minimizes the functional [45, 38]

$$E(F, \psi_F) = \langle \psi_F | H_0 | \psi_F \rangle - NFP(\psi_F) \tag{1.16}$$

where H_0 is the ordinary Hamiltonian at $F = 0$ and $P(\psi_F)$ the polarization in the presence of an electric field, defined trough the wavefunction ψ_F, according to equation (1.13). It has been demonstrated that the wavefunction that minimize the functional (1.16) correspond to the ground state of the effective Hamiltonian in the presence of an electric field: [38]

$$H(F, \psi_F) = H_0 - F\ \Delta M(\psi_F) \tag{1.17}$$

where ΔM is the ψ_F-dependent induced dipole moment operator defined as

$$\Delta M(\psi_F) = \frac{N}{2\pi}\ \mathrm{Im}\left[\frac{\exp(2\pi i \hat{M}/N)}{Z(\psi_F)} \right] \tag{1.18}$$

where

$$Z(\psi_F) = \langle \psi_F | \exp\left(i \frac{2\pi \hat{M}}{N} \right) | \psi_F \rangle \tag{1.19}$$

Although the problem is formally solved, the effective Hamiltonian (1.17) depends on ψ_F and a self-consistent iterative approach is needed. The wavefunction in the absence of the field, ψ_0, is used to build the effective Hamiltonian (1.17) and its diagonalization gives the ψ_F, and hence $P(\psi_F)$, correct to the first order in F. For the calculation of the polarizability, i.e. the first F derivative of P, no more iterations are needed; higher order derivatives of P would require more iterations. [38]

1.2.6 Uncorrelated models for NIT

CT crystal are a prototypical example of a strongly correlated electronic system as evidenced by the presence of the (intrinsically correlated) Mott insulator I phase. Calculations on correlated models are computationally demanding and stacks with more than 20 sites can hardly be treated (see section 1.2.4). Uncorrelated models represent therefore the only viable alternative if results on long chains are needed. Uncorrelated models have recently been applied to NIT for the calculation of the infrared intensity of the Peierls mode [46] and for the evaluation of the energetic cost of metastable I domains (LR-CT). [37] Here long chains are required for the calculation of lattice phonons dispersion laws with a high resolution in the reciprocal space, as required to rationalize the diffuse X-ray data (see section 1.5).

Specifically we will make resort to a spinless fermion (SF) model. SF Hamiltonian for a stack with dimerization amplitude δ is formally obtained from equation (1.7) by omitting the spin degrees of freedom and neglecting electrostatic interactions ($V = \varepsilon_c = 0$). Holstein coupling is not considered here because we are only interested in the dimerization instability. The model describes $N/2$ SF, or spinless electron, on N sites with alternating

energy $\pm\Gamma$. The uncorrelated NIT is governed by the parameter Γ: fermions occupy D sites for $\Gamma \gg 0$ (N phase) and A sites for $\Gamma \ll 0$ (I phase). The uncorrelated N and I phases are however equivalent, and can be obtained by simply exchanging D and A sites. Quite obviously, the SF model cannot describe a true I phase (Mott insulator), but provides a reliable description of the Peierls instability upon approaching NIT. In fact uncorrelated models have already been successfully applied to NIT, demonstrating that, at least in the proximity of the lattice instability, a proper modeling of e-ph coupling is more important than a detailed description of electronic correlations. [46]

Non-interacting Hamiltonians can be diagonalized analytically. The wavefunction of the system is the product of single particle orbitals whose energies are

$$\epsilon_k = \pm\sqrt{\Gamma^2 + 4\cos^2 k + 4\delta^2 \sin^2 k} \tag{1.20}$$

where k labels the wavevectors in the first Brillouin zone. The ground state of the system is obtained by filling the valence band with $N/2$ SF. The ground state energy per site is

$$E = -\frac{1}{N}\sum_k \sqrt{\Gamma^2 + 4\cos^2 k + 4\delta^2 \sin^2 k} \tag{1.21}$$

Since we are dealing with $N/2$ particles, the stack ionicity operator is slightly modified respect to equation (1.2), resulting

$$\hat{\rho} = \frac{1}{2} + \frac{1}{N}\sum_i (-1)^i \hat{n}_i \tag{1.22}$$

and its expectation value can be calculated from the Γ derivative of GS energy

$$\rho = \frac{1}{2} + \frac{\partial E}{\partial \Gamma} = \frac{1}{2} - \frac{1}{N}\sum_k \frac{\Gamma}{\sqrt{\Gamma^2 + 4\cos^2 k + 4\delta^2 \sin^2 k}} \tag{1.23}$$

In the infinite chain limit the sums can be expressed in terms of complete elliptic integrals, [47] so that in the $N \to \infty$ limit:

$$\rho = \frac{1}{2} - \frac{\Gamma}{\pi\sqrt{\gamma^2 + 4}}\ \mathrm{cel}(q_c, p = 1, a = 1, b = 1) \tag{1.24}$$

with $q_c^2 = \frac{\Gamma^2+4\delta^2}{\Gamma^2+4}$ and

$$\mathrm{cel}(q_c, p, a, b) = \int_0^{\pi/2} \frac{a\cos^2 k + b\sin^2 k}{(\cos^2 k + p\sin^2 k)\sqrt{\cos^2 k + q_c^2 \sin^2 k}}\, dk \qquad (1.25)$$

1.3 State of art

1.3.1 The phase diagram: potential energy surfaces and multistability

The modified Hubbard Hamiltonian with Peierls and Holstein coupling in equation (1.8), despite its simplicity, catches the main features of the phase diagram of mixed stack CT salts. In this section the (zero temperature) phase diagram of Hamiltonian (1.8) is qualitatively discussed, pointing attention on the potential energy surfaces (PES), associated with the different phases. Results and figures of this section are adapted from reference [37].

Hamiltonian (1.8) is the sum of an effective electronic part (the first two terms) plus constant terms (mf constants and elastic energy of the coupled modes). The effective electronic Hamiltonian is defined in terms of just two parameters $\Gamma_{eff} = \Gamma - V/2 + q - \varepsilon_c \rho$ and δ. Diagonalizing this Hamiltonian on a mesh of Γ_{eff} and δ values, we calculate the ground state energy $E(\Gamma_{eff}, \delta)$ and ionicity $\rho(\Gamma_{eff}, \delta)$. For fixed model parameters (Γ, V, $\mathcal{M}$, ε_d and ε_{sp}) we can extract for each Γ_{eff} the corresponding q value ($q = \Gamma_{eff} - \Gamma + V/2 + \varepsilon_c \rho$). With this procedure we calculate the total energy (per DA pair) $E(\delta, q)$, as a function of the two vibrational coordinate. This function is the ground state adiabatic potential energy surface (PES), whose minima locate the equilibrium geometries of the system. [37]

Reliable estimates of the parameters entering Hamiltonian (1.8) are available for TTF-CA. [48] The values of model parameters are expressed in units of the CT integral t. For TTF-CA was estimated $t \sim 0.21\ eV$. [33] Current estimates for the strength of electron-phonon (e-ph) and electron-molecular vibration (e-mv) coupling are $\varepsilon_d \sim 0.2 - 0.3$ and $\varepsilon_{sp} \sim 1.8$. [33, 48] The Madelung constant is in the range $\mathcal{M} \sim 1 - 1.5$. [49] More delicate are estimates of V, the nearest neighbor electrostatic interaction. Quantum chemical calculations, obtained neglecting dielectric screening, set an upper

limit for $V \sim 10t$. [49] Direct estimates of Γ also seem to be large. [49] For the sake of simplicity, here we fix all model parameters, with the exception of V. In fact NIT will be induced by increasing V, to mimic the increase of electrostatic interactions due to volume contraction.

We consider first the case of a discontinuous NIT, similar to that observed in TTF-CA. Figure 1.4 reports the equilibrium dimerization δ_0 and ionicity ρ_0 (ionicity calculated for the equilibrium geometry of the system), calculated as a function of V for parameters in the figure caption. The transition is clearly discontinuous: ρ_0 smoothly increases from ~ 0.25 to ~ 0.4 with increasing V and then abruptly jumps toward I values ($\rho_0 > 0.6$). The stack remains regular ($\delta_0 = 0$) on the N side and dimerizes in the I regime ($\delta_0 \sim 0.12$). In the proximity of the transition a bistability region appears, marked in figure 1.4 by dotted lines, where two non-equivalent minima are found. Bistability is a typical feature of discontinuous transitions.

Figure 1.5 shows ground state PESs $E(\delta, q)$ (left column) and relative contour plots (right column) calculated for the system described in figure 1.4 at three different V values (marked by arrows in figure 1.4). The PES in the top panels, calculated for $V = 2.26$, is representative of a N regular system, whose equilibrium is found at $\delta_0 = 0$. The PES in the bottom panels ($V = 2.42$) is instead characteristic of an I dimerized stack, which, unconditionally unstable to dimerization, presents two equivalent minima at finite $\pm\delta_0$, corresponding to I dimerized phases with opposite polarization. Central panels, calculated for $V = 2.34$, i.e. a value within the bistability region, show a PES with three minima, as can be better appreciated from the contour plot. The minimum at $\delta_0 = 0$, is relative to a N regular system, while the two equivalent minima at finite $\pm\delta_0$ describe two equivalent I phases. It is worth noting the large anharmonicity of all PES shown in figure 1.5, due to the coupling of harmonic phonons with delocalized electrons.

The nature of the transition can be modified by a slight adjustment of

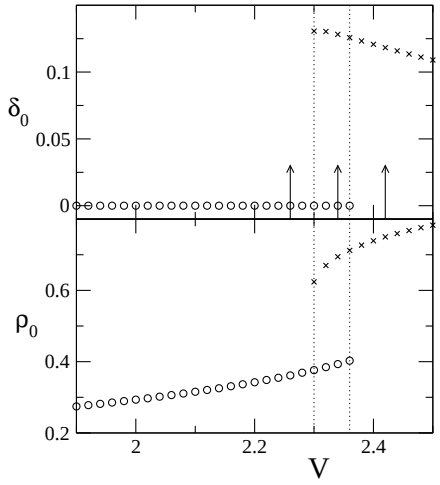

Figure 1.4: Equilibrium dimerization δ_0 and ionicity ρ_0 for a discontinuous NIT, calculated with $\Gamma = 0.5$, $\varepsilon_d = 0.28$, $\varepsilon_{sp} = 1.8$ and $\mathcal{M} = 1.4$ for $N = 16$ sites (results for $N = 14$ are analogous and not shown). For clarity the two phases are shown with different symbols. Dotted lines marks the limits of the bistability region. Arrows in the upper panel marks the V values for which PES are drawn in figure 1.5.

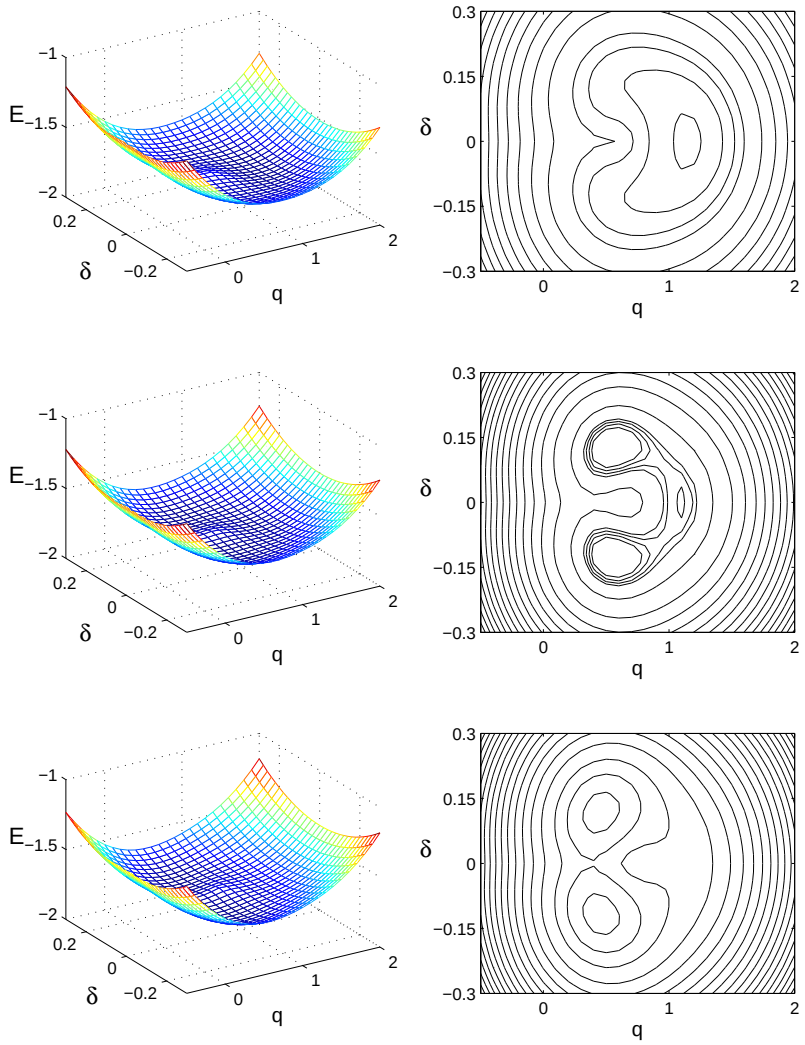

Figure 1.5: PESs (left column) and respective contour plots (right column) relevant to the system in figure 1.4, calculated for $V = 2.26$ (upper panels), $V = 2.34$ (central panels) and $V = 2.42$ (lower panels).

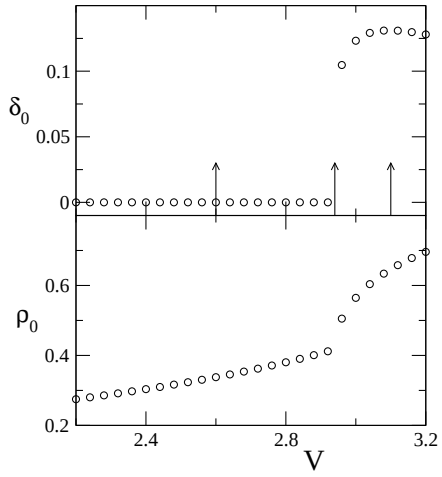

Figure 1.6: Equilibrium dimerization δ_0 and ionicity ρ_0 for a continuous dimerization (Peierls) transition, calculated with same parameters in figure 1.4 and $\mathcal{M} = 1.1$ for $N = 16$ sites (results for $N = 14$ are analogous and not shown). Arrows in the upper panel marks the V values for which PES are drawn in figure 1.7.

model parameters. [37] Equilibrium dimerization and ionicity for a continuous (second order) transition are reported in figure 1.6 and are obtained for the same parameters of figure 1.4, but a smaller $\mathcal{M} = 1.1$. In this case dimerization occurs on the N side at $\rho_0 \sim 0.4$, where a steep but continuous increase of the ionicity occurs, as observed in DMTTF-CA. At variance with DMTTF-CA, where ionicity remains always lower than ~ 0.45, we calculate $\rho_0 \sim 0.7$ in the I limit. This disagreement is not too much surprising because of the simplicity of the model. In fact we induce NIT by simply tuning V, but also the CT integral t is expected to increase upon lattice contraction, favoring states with intermediate ionicity. A quantitative simulation of all the features of NIT clearly goes beyond the scope of the present analysis.

Figure 1.7 shows the ground state PESs and relative contour plots (left

and right columns respectively) calculated for the system of figure 1.6 at three different V values (marked by arrows in figure 1.6). The PES in the top panel ($V = 2.6$) is representative of a N regular system, with a single minimum at $\delta_0 = 0$, while the PES in the bottom panel ($V = 3.1$) describes an I dimerized stack with $\delta_0 \sim 0.12$. At variance with the discontinuous transition discussed above, in this case the PES smoothly evolves from a single minimum in the N phase to a double minimum in the I phase. The PES in the central panels, calculated for $V = 2.94$, represents a system just at a continuous N-I interface.

In mixed stack CT crystals the coupling to both lattice phonons and molecular vibrations is amplified by the proximity of both valence and lattice instability, as proved by the softening of the relevant frequencies and by the largely anharmonic PES in figure 1.5 and 1.7. Both Peierls and Holstein vibrations enter the Hamiltonian (1.8) as purely harmonic, therefore the anharmonicity is due to the coupling to the electronic system. The nature of the transition is governed by the competition between a discontinuous crossover, coupled to on-site vibrations and a continuous dimerization transition, driven by the softening of the Peierls phonon. When moving from the N to the I phase, the coupling to delocalized electrons causes a decrease of the curvature of the PES along the δ direction so that a softening of the Peierls mode develops in any case. However, in systems with a large enough ε_{sp} or $\mathcal{M}$, a discontinuous NIT occurs *before* the complete softening of the Peierls mode, with the condensation of the Holstein phonon. This is the case of figure 1.4, where a discontinuous NIT takes place, accompanied by lattice dimerization. On the opposite, when ε_{sp} or $\mathcal{M}$ are small, a *complete softening* of the Peierls mode drives the dimerization transition, as for the system in figure 1.6. In this case, the frequency of the Peierls mode decreases approaching the transition and vanishes at the dimerization, where the PES is locally flat (see central panels of figure 1.7).

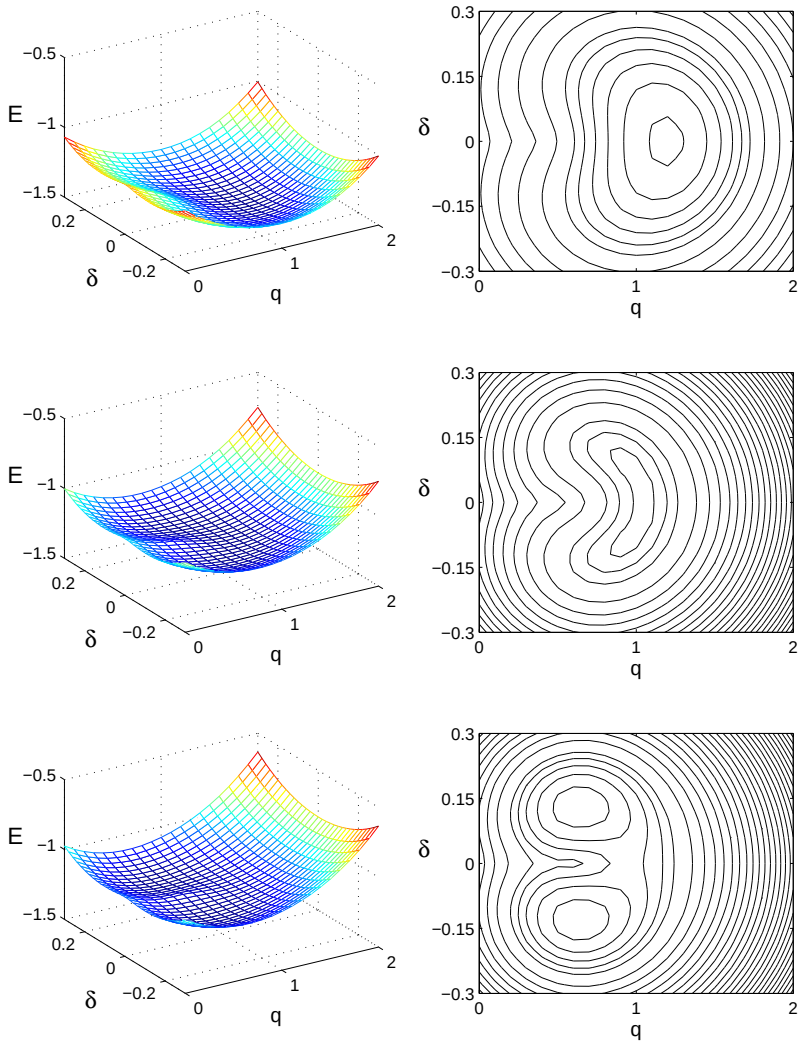

Figure 1.7: PESs (left column) and respective contour plots (right column) relevant to the system in figure 1.6, calculated for $V = 2.6$ (upper panels), $V = 2.94$ (central panels) and $V = 3.1$ (lower panels).

We conclude this section remarking two aspects: first, multistability is only expected at discontinuous transition, when PES with multiple non-equivalent minima indicate the presence of multiple (meta)stable phases. The coexistence of N and I phases is then expected only in the close proximity of a discontinuous NIT when the energy difference of respective minima is comparable with thermal energy. [37] An example of coexistence at ambient temperature is given by the pressure induced NIT of TTF-CA [50, 51]. The second remarkable fact is that softening and anharmonicity are common features of both continuous and discontinuous transitions and are originated by electron-phonon coupling. Experimental evidences of anharmonicity were clearly recognized in vibrational spectra of TTF-CA, DMTTF-CA and other CT salts [52, 53, 54, 55, 28].

1.3.2 The phenomenology of NIT

The phenomenology of NIT is fairly rich and we shorty summarize here some of the most interesting experimental results. The static dielectric constant presents a quasi divergent behavior at NIT with peak values higher than 500. Such anomalous dielectric response, extensively studied by Horiuchi *et al.* on TTF-CA and DMTTF-CA derivatives, is a characteristic feature of the ferroelectric transition of systems undergoing NIT [53, 54].

Anomalous features were observed in mid-infrared (IR) absorption spectra polarized parallel to the stack axis, in systems approaching NIT from the N side. [52] As shown in figure 1.8, where mid-IR (dashed line) and Raman (continuous line) spectra of TTF-CA at different temperatures are reported, couples of broad and intense absorptions (marked with asterisks) appear around the Raman bands associated with the totally symmetric molecular vibrations (mv). Specifically, for each Raman band the two absorption peaks are observed almost symmetrically located at lower and higher frequency. The two sidebands approach each other when the system moves

toward NIT and collapse in a single band, superimposed to the Raman band in the I dimerized phase. The coincidence of mid-IR and Raman spectra was the first evidence of dimerization in TTF-CA, [52] later confirmed by neutron scattering. [56] Similar features were observed in many CT salts [52, 53, 54, 55, 28] and remained unassigned for a long time.

An intense signal has been recently observed in our laboratory in the lattice phonon region of the Raman spectrum of DMTTF-CA in the close proximity of the NIT. [57] Raman spectra of DMTTF-CA measured with incident and scattered light polarized perpendicular to stack axis at different temperatures are shown in figure 1.9. The lattice phonon region of the Raman spectrum (below 150 cm^{-1}) of DMTTF-CA is characterized, both in the N and in the I phase, by the presence of a single narrow band, located around 80 cm^{-1}, stemming out from a flat background. However, a few degree Kelvin before the transition temperature (65 K) a broad and intense signal grows below 100 cm^{-1}. The scattered intensity reaches its maximum around 60 K and completely disappears below 40 K. A similar behavior, although less pronounced, has been observed in TTF-CA. [57]

An intense diffuse X-ray signal has been observed in DMTTF-CA and TTF-CA when approaching the transition from the N side [58, 59]. The scenario is similar for both compounds: the DXR signal is observed in the $(\mathbf{b}^*, \mathbf{c}^*)$ planes of the reciprocal space around Bragg reflections with integer values of the Miller index h. As an example, figure 1.10 (from ref. [59]) shows the intensity of the diffuse X-ray signal around the $(3\ 1\ \overline{1})$ reflection of TTF-CA at 84 K [59]. The presence of diffuse planes is a clear indication that pretransitional fluctuations are mainly restricted to stack direction and confirm the 1D nature of the transition. DXR profile, measured scanning the reciprocal space along $\mathbf{a}^*$ far enough from the Bragg reflection, present an almost Lorentzian shape and become more intense and sharper upon approaching the transition. The experimental picture is completed by the

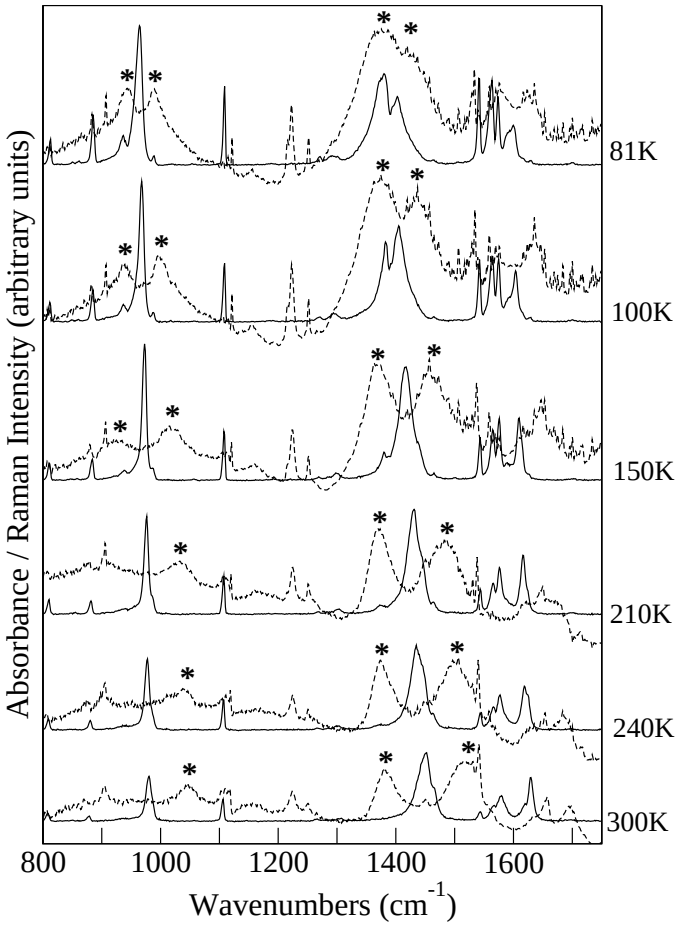

Figure 1.8: IR (dashed line) and Raman (continuous line) spectra of TTF-CA at different temperatures from ref. [55]. Mid-IR sidebands are marked with asterisks. Similar features were observed in DMTTF-CA (figure 1.20, page. 60) and other CT salts [53, 54].

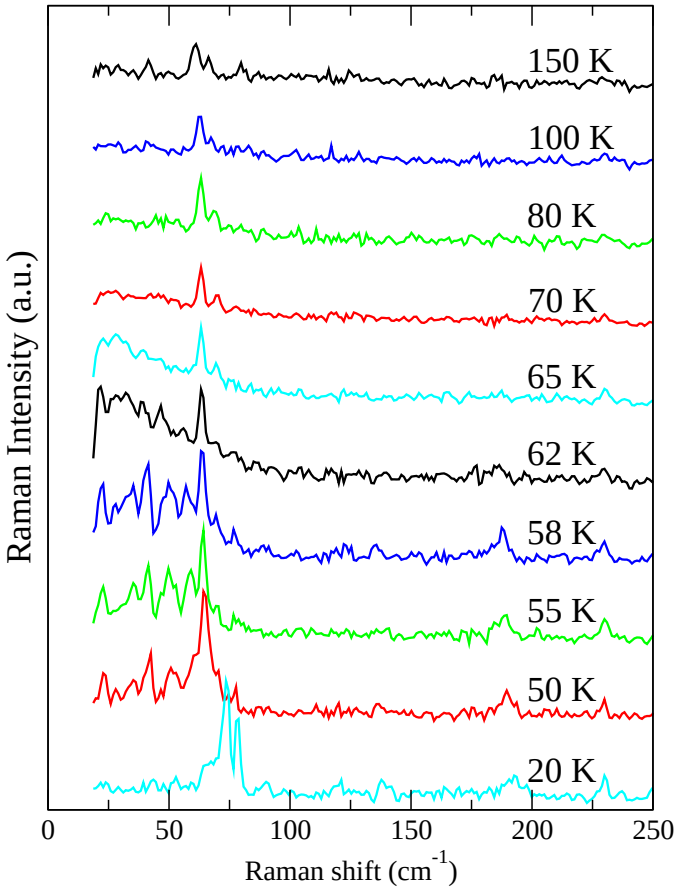

Figure 1.9: Raman spectra of DMTTF-CA at different temperatures. Data collected with incident ($\lambda_{exc} = 647\ nm$) and scattered light polarized perpendicular to stack axis. [57]

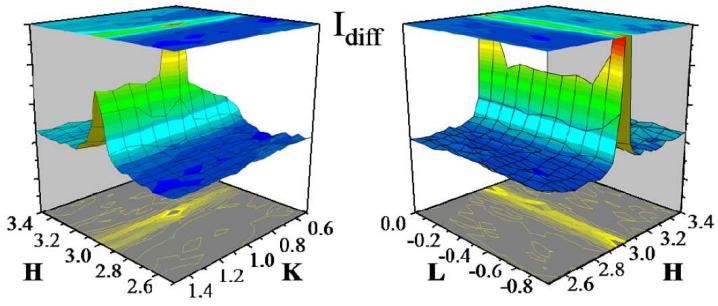

Figure 1.10: Diffuse X-ray planes around the (3 1 $\bar{1}$) Bragg reflection of TTF-CA at 84 K. Image from reference [59].

one order of magnitude increase of the d.c. electrical conductivity, just a few degrees above the TTF-CA temperature induced NIT. [60]

Different interpretations of this complex scenario were proposed. Tokura, Horiuchi, Collet *et al.* attributed most of these experimental data to the presence of metastable I dimerized domains, the so called lattice relaxed CT exciton strings (LR-CT) and to the dynamic of their boundaries, the N-I domain walls (NIDW) [53, 54]. LR-CT and NIDW were originally introduced by Nagaosa [31, 61] as typical excitations of 1D systems with a mixed stack motif. Although these concepts are surely fascinating, the proposed interpretation must be reconsidered. First, the discussion is based only on qualitative arguments and no detailed modelization of experimental data was offered. Moreover, while LR-CT and NIDW were invoked to explain the phenomenology of both continuous and discontinuous transitions, these excitations, as earlier recognized by Nagaosa, are expected only in the close proximity of a discontinuous transition [31, 61] and in most cases the energy of the domains is too large for appreciable thermal population [37].

Soos, Painelli, Girlando *et al.* explained some of the unconventional

features of NIT as due to the dramatic effects of e-ph coupling in a 1D system presenting both a structural and a valence instability. Specifically, the anomalous dielectric peaks were explained as a manifestation of e-ph coupling and were *quantitatively* reproduced using the Peierls-Hubbard model and the Berry phase formulation of polarization in dielectrics [46, 38]. In that works the authors evidenced the role of the soft Peierls phonon that acquires huge infrared (IR) intensity at the transition, inducing large charge fluctuations that are responsible for the dielectric anomaly. The presence of the Peierls phonon is of fundamental importance also for the interpretation of mid-IR spectra. Girlando *et al.*, from an analysis of the temperature dependence of IR and Raman spectra of TTF-CA and DMTTF-CA, showed that unassigned sidebands in mid-IR spectra can be interpreted as sum and difference combinations of the Raman active mvs and a lattice mode that softens approaching the transition. [55, 28] The appearance of intense combination bands is a clear indication of a strong anharmonicity as confirmed by the theoretical results presented in the previous section. [37] The direct observation of the Peierls mode proved difficult because of experimental limitations and of the complex lattice phonons structure of molecular crystals [62]. In a recent paper Girlando *et al.* reported far-IR reflectivity measurement on TTF-CA, that allowed the direct observation of lattice modes involved in the Peierls mechanism. [63] From the analysis of experimental spectra an average or effective Peierls mode was defined. This effective mode softens upon approaching NIT in quantitative agreement with mid-IR spectra. Moreover, frequency and IR intensity of the effective Peierls mode agrees with theoretical results obtained with the Peierls-Hubbard model and justify the single mode picture.[63]

We can anticipate that the vibrational spectra presented in section 1.4, obtained fully relaxing the harmonic approximation, give the definitive confirmation of the interpretation of mid-IR bands as combinations. Moreover,

we will show also the Raman signal, observed in the lattice phonon region in DMTTF-CA, is another manifestation of the strong anharmonicity of this system. Finally, the diffuse X-ray signal observed in TTF-CA and DMTTF-CA can be explained as another manifestation of the soft Peierls mode and of the related Kohn-like anomaly, as it will be discussed in section 1.5.

1.4 Modeling vibrational spectra at NIT

1.4.1 Time correlation functions and spectroscopy

The fluctuation dissipation theorem states that the dissipative processes originated from the weak coupling between two physical systems can be described in terms of the equilibrium fluctuations of the uncoupled systems. Equilibrium fluctuations are formally expressed by time autocorrelation functions (TCF) of the appropriate physical quantities. TCF are therefore extremely useful in the context of spectroscopy, since they offer a general method to calculate the response of a material system to external stimuli. [64] Qualitatively, a TCF describes how long a given property of a system persists, until it is averaged out by microscopic fluctuations. Formally, the TCF of a quantity A is defined by the ensemble average

$$C(t) = \langle A(0)A(t)\rangle \tag{1.26}$$

In ergodic systems, assuming A defined with zero average, TFC approaches zero for long times.

In the case of absorption of radiation, as for IR spectroscopy, the imaginary (dissipative) part of the dielectric constant of the material is obtained from the Fourier transform of the TCF of the dielectric polarization $\vec{P}$: [64]

$$\varepsilon''(\omega) = \frac{1 - e^{-\frac{\hbar\omega}{k_B T}}}{4\varepsilon_0 V\hbar} \int_{-\infty}^{\infty} e^{i\omega t}\ \langle \hat{\epsilon}\cdot\vec{P}(0)\ \hat{\epsilon}\cdot\vec{P}(t)\rangle\ dt \tag{1.27}$$

where $\hbar$ is the reduced Planck constant, k_B is the Boltzmann constant, ε_0 is the vacuum permittivity, V is the volume and $\hat{\epsilon}$ sets the direction of the incident light. Similarly, the TCF of the polarizability tensor $\boldsymbol{\alpha}$ is related to the intensity of the Raman scattering: [64]

$$I_R(\omega) = \int_{-\infty}^{\infty} e^{i\omega t}\ \langle(\hat{\epsilon}_I\cdot\boldsymbol{\alpha}(0)\cdot\hat{\epsilon}_S)(\hat{\epsilon}_I\cdot\boldsymbol{\alpha}(t)\cdot\hat{\epsilon}_S)\rangle\ dt \tag{1.28}$$

where $\hat{\epsilon}_I$ and $\hat{\epsilon}_S$ are the versors of the incident and scattered light respectively. Expressions 1.27 and 1.28 results from a quantomechanic treatment of the interaction between light and matter in the weak coupling regime.

While equations (1.27) and (1.28) are exact, approximations are introduced in the calculation of TCF. A common approach considers the vibrational dynamics of the system governed by the Newton equations of motion. TCF calculated with molecular dynamics (MD) simulations, with empirical force fields, provided much insight in the optical properties of liquids and solutions (see, for example, refs. 39-48 of ref. [65]).

In recent times, MD simulations have been combined with quantum mechanics first principle electronic structure calculations. The most popular among these methods is the Car-Parrinello MD, [66] in which electrons are treated within the density functional formalism while nuclei are treated classically. The forces experimented by the nuclei are obtained as derivatives of the ground state electronic energy with respect to the vibrational coordinates, assuming the validity of the adiabatic approximation. The application of first principle MD to the calculation of vibrational spectra of crystals [67, 68, 69] has been made possible by the major advances in the modern theory of polarization in dielectrics, that overcame the problem in the definition of polarization and polarizability in systems with periodic boundary conditions (see section 1.2.5).

A similar semiclassic approach to time correlation functions is provided here, with the vibrational motion governed by classical equations of motion in the quantomechanic potential obtained from the model Hamiltonian in equation (1.8). The two effective vibrational coordinates q and δ, defined in section 1.2.3, are considered. The vibrational dynamics of our system is governed by the potential energy surface (PES) $E(q, \delta)$ presented in section 1.3.1. The electronic contribution (fluctuating charges) to the stack polarization and polarizability are calculated according to equations (1.13) and

(1.15). The contribution from the frozen molecular charges is negligible, at least in the proximity of NIT, and is not considered. [46, 38]

According to equation (1.27), the TCF of the stack polarization, P, gives the IR absorption spectra polarized along the stack axis. The stack polarizability α, following equation (1.28), is related to the Raman signal obtained with both incident and scattered light parallel to stack axis. Most of the available Raman data are however obtained with polarization of incident and scattered light perpendicular to the stack axis (parallel to the molecular plane) and in the (pre-)resonant regime with molecular electronic excitations. These spectra can be modeled in terms of molecular polarizability that is not described by our model. To simulate perpendicularly polarized Raman spectra in the region of mv we approximate the molecular polarizability by a linear expansion on q:

$$\alpha_{mol} = \alpha_0 + \left(\frac{\partial \alpha_{mol}}{\partial q}\right)_{q=0} q \tag{1.29}$$

It is worth noting that Raman spectra are calculated in the low frequency limit for the incident light (non resonant Raman scattering). In fact our calculation is based only on the ground state properties. For simplicity in the following we will refer to parallel (incident and scattered light) and to perpendicular (incident and scattered light) Raman spectra, where the polarization is defined with respect to the direction of the stack axis.

1.4.2 Details of the calculation

The simulation of vibrational spectra consists of three basic steps: (a) the integration of the Newton equations of motion, (b) the calculation of TCF and (c) the Fourier transform of TCF to obtain the spectra.

Newton equations of motion for the vibrational dynamics are

$$\begin{aligned}\ddot{q}(t) &= -\frac{\varepsilon_{sp}\Omega_H^2}{2}\, F_q(q,\delta) \\ \ddot{\delta}(t) &= -\frac{\varepsilon_d\Omega_P^2}{2}\, F_\delta(q,\delta)\end{aligned} \tag{1.30}$$

where $F_q(q,\delta)$ and $F_\delta(q,\delta)$ are the q and δ components of the force (partial derivatives of $E(q,\delta)$) in the point $(q(t),\delta(t))$, Ω_P and Ω_H are the unperturbed harmonic frequencies of the Peierls and of the Holstein mode respectively. These frequencies are set to $\Omega_P = 90\ cm^{-1}$ and $\Omega_H = 1540\ cm^{-1}$ to reproduce experimental data. The relaxation energies ε_d and ε_{sp} were defined is section 1.2.3. For a given set of initial values $\mathbf{r_0} = (q(0),\delta(0),\dot{q}(0),\dot{\delta}(0))$ equations (1.30) are integrated to obtain the laws of motion $(q(t;\mathbf{r_0}),\delta(t;\mathbf{r_0}))$. The numerical integration of equations (1.30) is performed using the leapfrog algorithm. [70] Simulations are performed for a total time $t_{max} = 10\ ps$ with a time step of 25 fs. Forces $F_q(q,\delta)$ and $F_\delta(q,\delta)$ are calculated as partial derivatives of the PES $E(q,\delta)$ using numerical 5-point stencil formula. The numerical steps for the calculation of derivatives are $h_q = 0.05$ and $h_\delta = 0.01$. The calculation of forces with numerical derivatives requires the evaluation of the electronic ground state energy in many (q,δ) points. While in Car-Parrinello MD the electronic adiabatic Hamiltonian is diagonalized on the flight, [66] i.e. for each molecular geometry, in our case a different approach is preferable. Since we deal with a system with only two vibrational degrees of freedom, we can calculate $E(q,\delta)$ once and for all on a dense mesh of q and δ values. Other electronic quantities of interest, as polarization and polarizability, are calculated in the same mesh points. Optimal values for the steps of the mesh are 0.05 and 0.01 for the q and the δ coordinate respectively. Bilinear interpolation algorithm is used to obtain the values of the electronic quantities outside the mesh points. Dynamics calculated with the leapfrog algorithm have been compared with dynamics calculated with more sophisticated numerical methods for solving initial value problems for

ordinary differential equations (Runge-Kutta methods, `ode*` MATLAB functions). The leapfrog algorithm provides an accurate solution of equations of motion (1.30), and our implementation in `fortran 95` code is about one order of magnitude faster than the MATLAB code.

The TCF of the generic quantity A is calculated performing an ensemble average over the initial conditions: [71]

$$\langle A(0)A(t)\rangle = \frac{1}{Z}\int \mathcal{P}(\mathbf{r_0})A(0;\mathbf{r_0})A(t;\mathbf{r_0})\ d\mathbf{r_0} \tag{1.31}$$

where $A(t;\mathbf{r_0})$ is the value of A at the time t obtained from a dynamic with initial conditions $\mathbf{r_0}$, $\mathcal{P}(\mathbf{r_0})$ is the Boltzmann probability distribution of initial conditions, Z is the canonical partition function and the integral is performed over the whole phase space. In principle, TCF can be calculated with an alternative procedure. In fact, assuming the validity of the ergodic hypothesis, the ensemble average over initial conditions can be substituted by an average over time intervals of a single long trajectory. [71] However, this long trajectory must results from a isothermal dynamics, as obtained by coupling the system to a thermostat, i.e. introducing an additional degree of freedom that reacts to the time evolution of the system to keep constant the total kinetic energy. [72, 73] This approach is well established and widely adopted in molecular dynamics simulations, where systems with many degrees of freedom are treated, but cannot be used in our system, where only two degrees of freedom are considered.

The time evolution of electronic quantities, as polarization and polarizability, is calculated propagating adiabatically the electronic wavefunction ψ on the classical trajectories:

$$A(t;\mathbf{r_0}) = A[\psi(q(t;\mathbf{r_0}),\delta(t;\mathbf{r_0}))] \tag{1.32}$$

Polarization and polarizability are recorded each ten time steps. Ensemble average over initial condition, expressed by integral in equation (1.31), is

approximated by a discrete sum. The phase space is evenly sampled with steps $dq = 0.025$, $d\delta = 0.003$, $d\dot{q} = 5.3\,10^{12}\ s^{-1}$, $d\dot{\delta} = 2.3\,10^{11}\ s^{-1}$. Such a fine sampling over initial values is required for the calculation of the TCF of the stack polarizability, since the $\alpha(q, \delta)$ surface is characterized by a sharp peak (see figure 1.16 at page. 53). TCF of the stack polarization or of the molecular polarizability can be calculated also with coarser sampling. Fixed as unit the probability of the dynamic starting at the PES minimum with zero velocity, thermal averages are calculated only accounting for dynamics with initial values, $\mathbf{r}_0$, such that $\mathcal{P}(\mathbf{r}_0) > 0.01$. No appreciable effects on the calculated spectra are observed by lowering this threshold. TCF are not calculated with the bare polarization and polarizability, but with their deviation from the corresponding average values. This ensures proper convergence of TCF to zero in the $t \to \infty$ limit and eliminates spurious low frequency tails in the Fourier transforms.

The TCF are multiplied by a Gaussian damping factor $e^{-k\,t^2}$, with $k = 5\ 10^{-23}\ s^{-2}$, in order to smooth numerical noise in the calculated spectra. Fourier transforms are calculated using the fast Fourier transform algorithm (`fft` MATLAB function).

1.4.3 The anharmonicity of the model system

The system considered here is a mixed stack undergoing a second order transition, described by the model Hamiltonian in equation (1.8) and characterized by the same model parameters as the system in figure 1.6, apart from a readjustment of the vibrational relaxation energies ε_{sp} and ε_d. To allow for a direct comparison with experimental spectra, we focus on a single mv and specifically on the mode responsible for the band observed at about 1450 cm^{-1} in the room temperature Raman spectra of TTF-CA (see figure 1.8) and DMTTF-CA (see figure 1.20). The vibrational relaxation energy $\varepsilon_{sp} \approx 1.8$, estimated in section 1.3, measures the overall strength of

coupled modes. Since here we are concentrating on a specific mode, its value is reduces to $\varepsilon_{sp} = 0.7$. The contribution from other modes to the charge instability can be accounted for by increasing the strength of electrostatic interactions. [33] The lattice relaxation energy is set to $\varepsilon_d = 0.4$, in order to better reproduce experimental spectra. Results are presented for a 16 sites chain, results for $N = 14$ and $N = 18$ are similar. As in section 1.3.1, all model parameters are fixed apart V, that is tuned to induce NIT, in order to mimic the increase of electrostatic interactions upon lattice contraction. Figure 1.11 shows equilibrium dimerization (top panel) and stack ionicity (central panel), calculated as a function of V, for the new set of parameters.

Calculated spectra will be compared with experimental data collected for the DMTTF-CA T-induced NIT. Temperature is a delicate parameter in our simulation and strongly affects the calculated spectra. In fact temperature determines the amplitude of thermal fluctuations and therefore sets the explored portion of the PES $E(q, \delta)$, and hence of the $P(q, \delta)$ and $\alpha(q, \delta)$ surfaces. The $V(T)$ dependence is therefore chosen as to best reproduce experimental spectra and the resulting relation in shown in the bottom panel of figure 1.11. A smooth and monotonous dependence is found.

The basic ingredients in the simulation of vibrational spectra are the PES, $E(q, \delta)$, that governs the time evolution, and the dependence of polarization and polarizability on the two vibrational coordinates, i.e. $P(q, \delta)$ and $\alpha(q, \delta)$ surfaces. The intimate entanglement between electrons and vibrations makes the physics of NIT is very interesting. In fact, in addition to the strong anharmonicity of the PES, already discussed in section 1.3.1, major effects are due to the electrical anharmonicity, defined as the deviation of $P(q, \delta)$ and $\alpha(q, \delta)$ functions from a linear behavior. Figure 1.12 shows the PES calculated for $V = 1$ with the relevant color map in the right panel. The PES is clearly anharmonic and presents a single minimum (marked by white cross in right panel) that describes a N regular ($\delta_0 = 0$) stack. While

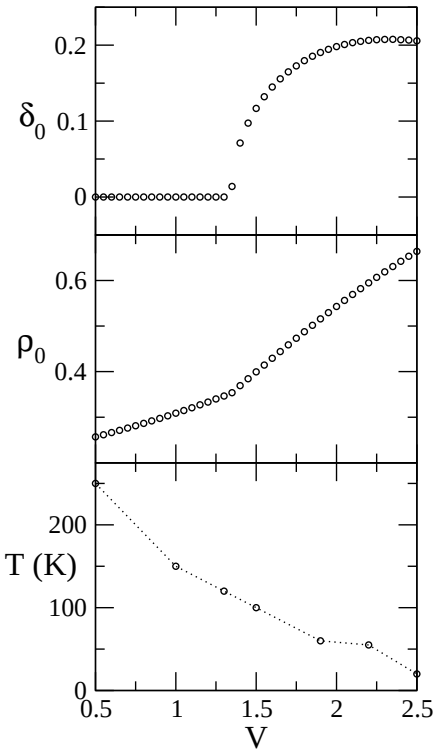

Figure 1.11: Equilibrium dimerization δ_0 (top panel) and ionicity ρ_0 (central panel) for a continuous dimerization (Peierls) transition, calculated with same parameters of figure 1.6, with the exception of $\varepsilon_{sp} = 0.7$ and $\varepsilon_d = 0.4$ for $N = 16$ sites. Lower panel: empiric relation between temperature and nearest neighbor electrostatic interaction V.

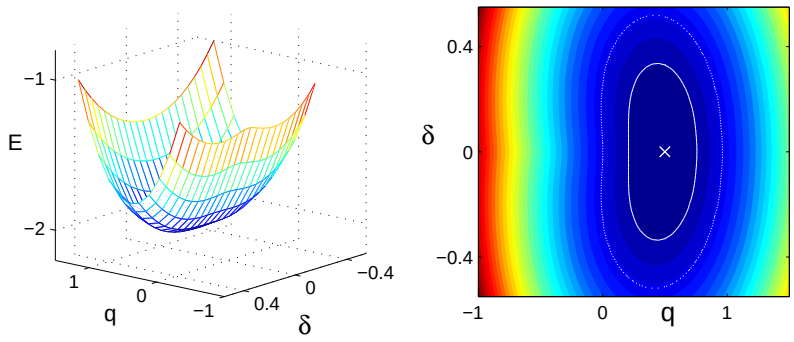

Figure 1.12: PES calculated for parameters of figure 1.11 and $V = 1$ (left panel) and relative color map (right panel). White cross marks the PES minimum. Continuous and dotted curves are PES isolines at $E_{1/2}$ and E_{lim} according to equation (1.33) with $T = 150\ K$ (see text).

at $T = 0$ only the equilibrium position is relevant, at finite temperature wide portions of the PES are explored because of thermal fluctuations. Explored regions of the PES are delimited by the white curves in the right panel of figure 1.12. Specifically, the continuous (inner) line and the dotted (outer) line are the PES isolines at

$$\begin{aligned} E_{1/2} &= E_0 + 1.5\ k_B T \\ E_{lim} &= E_0 - k_B T \log 0.01 \approx E_0 + 4.6\ k_B T \end{aligned} \tag{1.33}$$

where E_0 is the PES value in the minimum and (for $V = 1.0$, as for figure 1.12) $T = 150\ K$. The dotted curve limits the region explored by thermal fluctuations, the continuous curve marks the boundary of the region explored by the dynamics characterized by an energy lower than $1.5\ k_B T$. These dynamics weight for about one half ($\pm 5\%$ depending on the specific PES and T) of the total probability.

The color maps of the PES, calculated for $V = 1.3$, 1.5, 1.9 and 2.2 are shown in figure 1.13. With increasing V the harmonic frequency of

the Peierls mode softens and vanishes at $V = 1.3$ where the PES is locally flat (left upper panel, figure 1.13). For larger V, two minima develop, corresponding to equivalent I dimerized phases with opposite dimerization. While at $T = 0$ the presence of a double minimum signals the dimerization, at finite T the key quantity is the ratio $\Delta E/k_B T$, where ΔE measures the energy barrier between the two dimerized phases. In fact for $V = 1.5$ (right upper panel, figure 1.13) the PES presents two minima, but the energy barrier is much smaller than thermal energy ($\Delta E = 5\ K$, $T = 100\ K$) and the stack is macroscopically regular. For $V = 1.9$ (left lower panel,figure 1.13) the energy barrier becomes comparable to thermal energy ($\Delta E = 58\ K$, $T = 60\ K$) and the system sets in the two minima. Finally, for $V = 2.2$ (right lower panel, figure 1.13) the energy barrier is higher than thermal energy ($\Delta E = 120\ K$, $T = 55\ K$ for $V = 2.2$) and the system is almost completely localized within the two minima.

The electronic stack polarization, calculated for $V = 1.0$, is shown in figure 1.14. P is expressed in ea per DA pair units, where e is the electronic charge and a the intermolecular distance. Polarization is an odd functions of δ and vanishes for symmetry in the regular stack ($\delta = 0$). For $q \gtrsim -0.5$ the δ-dependence of the polarization is smooth and, P stays relatively small in magnitude ($|P| < 0.3$). On the contrary for $q \lesssim -0.5$, P changes its sign abruptly at $\delta = 0$ and assumes large values at finite δ ($|P| > 0.6$). This behavior is not surprising, since the DA ionization energy Γ is linearly modulated by q, and for $q \approx -0.5$ the electronic system undergoes NIT. The steep behavior of P is therefore a manifestation of the dimerization instability of the NIT: tiny variations of the dimerization amplitude around $\delta = 0$ produce large reorganization of electronic charges resulting in highly polarized phases. The steep behavior of P is related to the huge IR intensity of the Peierls mode at NIT: in fact, within the harmonic approximation, the IR intensity is related to the squared δ derivative of the polarization

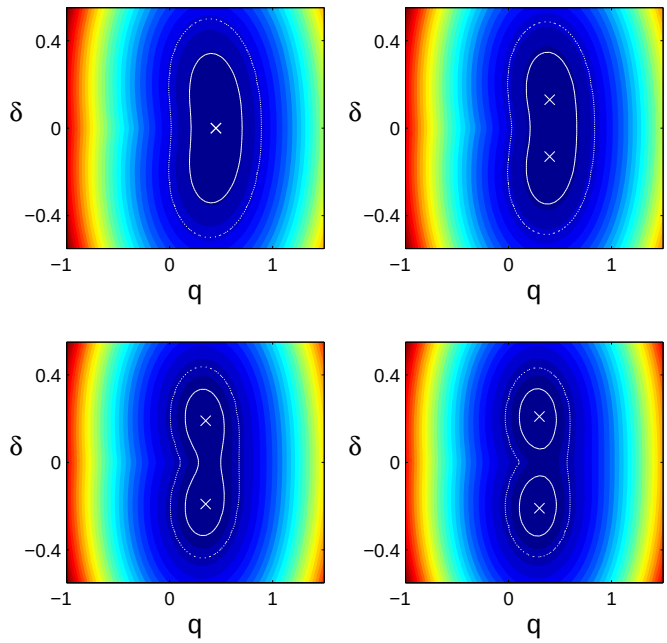

Figure 1.13: PES color maps calculated for parameters of figure 1.11 and $V = 1.3$, 1.5, 1.9 and 2.2, from left to right and top to bottom. White crosses mark PES minima. White curves are PES isolines at $E_{1/2}$ (continuous) and E_{lim} (dotted) according to equations (1.33), calculated for $T = 120$, 100, 60 and 55 K with increasing V.

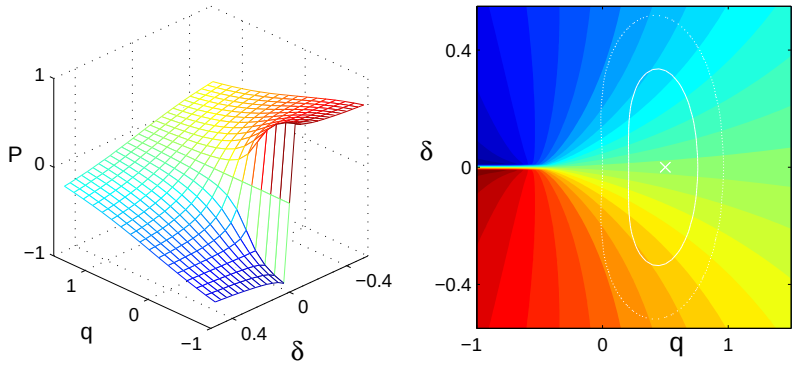

Figure 1.14: $P(q,\delta)$ function (left panel, *ea* per DA pair units) calculated for parameters in figure 1.11 and respective color map (right panel). White cross and curves report same quantities as in figure 1.12.

$\left(\frac{\partial P}{\partial \delta}\right)_0^2$. As it can be seen from the right panel of figure 1.14, for $V = 1$ and $T = 150\ K$ the system explores only the smooth region of P.

The $P(q,\delta)$ functions, calculated for $V = 1.3$, 1.5, 1.9 and 2.2, shown in figure 1.15, are similar to those observed in the $V = 1$ case (cf. figure 1.14), but the explored regions of the $P(q,\delta)$ surface vary considerably upon approaching NIT. With increasing V, the equilibrium point(s) of the PES approach the steep region of P that is explored by the system with important consequences on IR spectra. After the transition, however, the system localizes within the two wells and the steep region of P is visited with lower probability (see right lower panel of figure 1.15).

Figure 1.16 shows the adiabatic dependence of the electronic stack polarizability (e^2a^2/t per DA pair units) on the two vibrational coordinates, calculated for $V = 1$. The polarizability is an even function of δ and presents a peak at $\delta = 0$ and $q \approx -0.5$. The α peak is another consequence of the NIT, as previously discussed for the steep behavior of the polarization surface, and is strictly related to the dielectric anomaly. For $V = 1$, the peak of

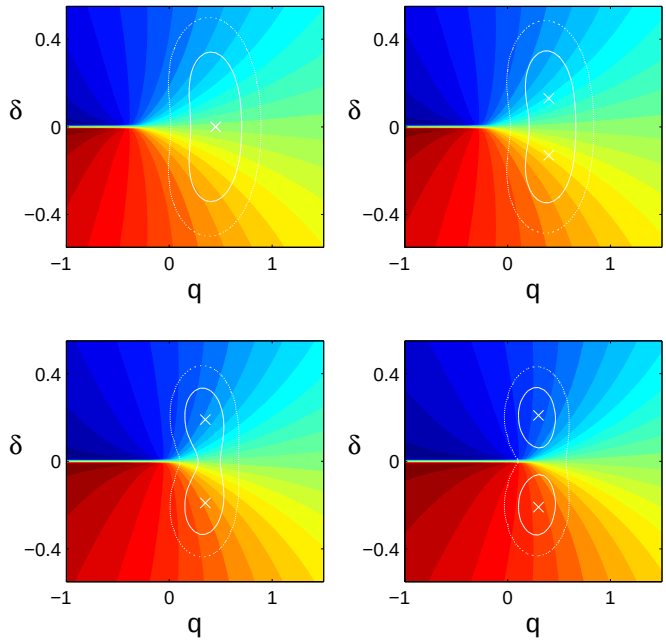

Figure 1.15: $P(q, \delta)$ color maps calculated for parameters in figure 1.11 and $V = 1.3$, 1.5, 1.9 and 2.2, from left to right and top to bottom. White crosses and curves reports PES minima and PES isolines as in figure 1.13.

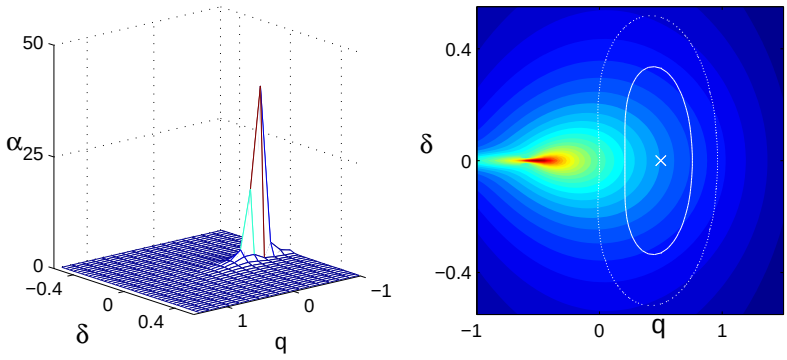

Figure 1.16: $\alpha(q, \delta)$ function (left panel, e^2a^2/t units per DA pair) calculated for parameters in figure 1.11 and respective color map on a logarithmic scale (right panel). White cross and curves report same quantities as in figure 1.12.

the polarizability is located, far from the equilibrium point of the PES (white cross in right panel), so that it is practically unexplored at $T = 150\ K$.

The $\alpha(q, \delta)$ functions, calculated for $V = 1.3$, 1.5, 1.9 and 2.2, are presented in figure 1.17. As for P, with increasing V, the α surface does not changes much, but, because of the changes of the PES and of T, the system explores the α peak. The very sharp peak in the $\alpha(q, \delta)$ is responsible for important effects in Raman spectra polarized parallel to the stack axis when approaching NIT.

1.4.4 Results and comparison with experiments

We begin the discussion with the results relevant to a N regular stack ($V = 1$ and $T = 150\ K$). Figure 1.18 shows the calculated TCF and spectra. The TCF of the stack polarization (left top panel) is characterized by an oscillation with a period of about 0.65 PS, but presents a higher frequency oscillation of much smaller amplitude, shown in the figure inset (enlargement

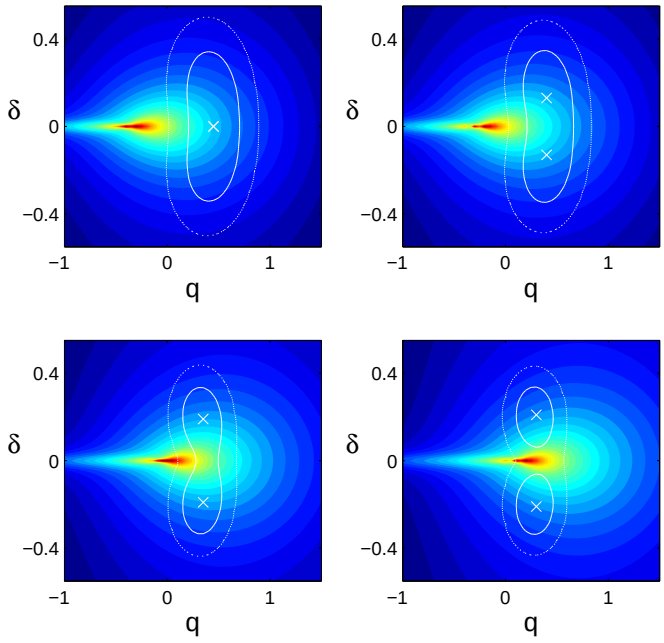

Figure 1.17: $\alpha(q, \delta)$ color maps (logarithmic scale) calculated for parameters in figure 1.11 and $V = 1.3$, 1.5, 1.9 and 2.2, from left to right and top to bottom. White crosses and curves reports PES minima and PES isocurves as in figure 1.13.

of the dashed box in the main figure). The same information contained in the P TCF (time domain) is found in its Fourier transform (frequency domain), corresponding to IR spectra, presented in the right top panel. The main oscillation is responsible for the intense absorption band in the low frequency region, that corresponds to the Peierls mode at $\omega_P = 55\ cm^{-1}$. The higher frequency oscillation, indeed, results in the two small bands located around 1400 cm^{-1} and enlarged in the figure inset. We anticipate that these bands correspond to sum and difference combinations of the Peierls mode with the totally symmetric mv (Holstein mode, with frequency ω_{mv}), i.e. $\omega_{mv} \pm \omega_P$.

TCF of the molecular polarizability, shown in the left middle panel, is dominated by a oscillation with a period of about 0.023 PS. This oscillation corresponds to the intense peak of the Holstein mode at $\omega_{mv} = 1420\ cm^{-1}$ in the perpendicular Raman spectrum, reported in the right middle panel.

The TCF of the stack polarizability and its Fourier transform, corresponding to the parallel Raman spectrum, are reported in left and right bottom panels, respectively. The scenario is more complex than in the previous case since the stack polarizability, explicitly dependent on δ, is sensitive to lattice oscillations. In fact, the TCF of the stack polarizability is characterized by a low frequency profile that modulates the high frequency oscillation of the Holstein mode. The mv region of the parallel Raman spectrum presents a main peak, corresponding to the Holstein mode at $\omega_{mv} = 1420\ cm^{-1}$, and two smaller combination bands at $\omega_{mv} \pm 2\omega_P$. In the region of lattice phonons, a band at $2\omega_P$ has a comparable intensity with the mv band (the Peierls mode is Raman forbidden by symmetry in the regular stack). A weak $4\omega_P$ band is also detected (see figure inset).

Now we turn attention to selected spectral regions, in order to follow the evolution of the spectra upon approaching NIT and perform direct comparisons with experimental data. We start from the region of mvs. IR and Raman spectra in this region are of primary importance, since they signal

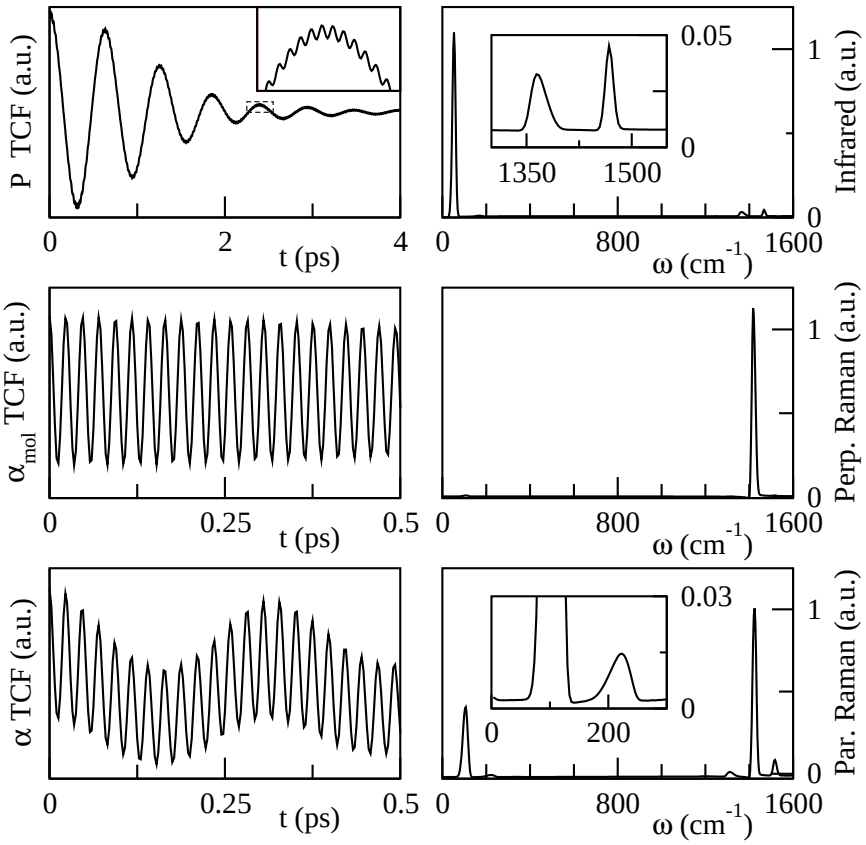

Figure 1.18: Left panels show (from top to bottom) TCF of the stack Polarization, molecular polarizability and stack polarizability. Right panels show the corresponding Fourier transforms, proportional to (from top to bottom) IR, perpendicular and parallel Raman spectra. Results are calculated for parameters in figure 1.11 and $V = 1$. Insets report enlargements of selected regions of the main panels (see text).

the stack dimerization. In fact, in the N regular phase each molecule stays on an inversion center and mvs modulate (molecular and stack) polarizability but not the polarization, so that they appear only in the Raman spectra. Dimerization removes the inversion symmetry and mv appear both in Raman and in IR spectra polarized parallel to stack axis. Moreover, mvs have in the dimerized phase a huge IR intensity because they borrow intensity from the electronic system (mvs move electronic charges). [52] The appearance of mvs in IR spectra polarized parallel to stack axis, or equivalently, the coincidence of mv's bands in Raman and IR spectra, is the spectroscopic signature of the the transition. Experimental Raman spectra in this region are available only for polarization perpendicular to the stack and in pre-resonant regime with molecular excitations. [55, 28] Attempts to measure non-resonant parallel Raman spectra in the mv region in our laboratory were unsuccessfully.

Figure 1.19 shows the calculated IR and perpendicular Raman spectra in the spectral region of mvs. Both IR and Raman spectra are rescaled for graphical reasons. The perpendicular Raman spectra (black line) is characterized by the softening of approximately 100 cm^{-1} of the totally symmetric mv band upon approaching NIT. In the N phase (see $V = 0.5$, $T = 250\ K$), the IR spectrum (red line) is characterized by the presence of the combination bands $\omega_{mv} \pm \omega_P$. Combination bands naturally result from the coupling to the electronic system that is responsible for the PES anharmonicity. Upon approaching the transition (see $V = 1.0$, $T = 150\ K$ and $V = 1.3$, $T = 120\ K$) combination bands broaden and, because of the softening of the Peierls mode, their spacing from the Raman band reduces. We observe that the hot band ($\omega_{mv} - \omega_P$) is generally broader ad more intense than the cold band ($\omega_{mv} + \omega_P$). For $V = 1.3$ the PES (reported in the left upper panel of figure 1.13) is locally flat, and the harmonic frequency of the Peierls mode vanishes. However, the frequency obtained from our finite temperature simulation ($T = 120\ K$) as half the difference of the position of the two bands,

is about 45 cm^{-1}. The IR spectra calculated for $V = 1.5$ at $T = 100\ K$ presents both the combination bands and a weaker central peak located midway, corresponding to the mv absorption. The simultaneous presence of the signals characteristic of the N regular phase and of the I dimerized phase can be easily understood. The PES for $V = 1.5$ (reported in the right upper panel of figure 1.13) presents two minima, separated by an energy barrier of only 5 K. When performing the thermal average over initial values to calculate the P TCF according to equation (1.31), there are dynamics that have enough energy to cross the barrier (that are in the $V = 1.5$ at $T = 100\ K$ case are the large majority), as well as dynamics that remain trapped in the wells. The former dynamics are responsible for the signal of the N regular stack (combinations), the latter for the I dimerized signal (mv absorption). Upon increasing the energy barrier and lowering T, the system is progressively trapped into the wells and for $V = 1.9$ ($\Delta E = 58\ K$) and $T = 60\ K$ we calculate the IR spectrum of a pure I dimerized phase.

The comparison with experimental spectra of DMTTF-CA, reported in figure 1.20, in the region of the Raman active mode located around 1440 cm^{-1} at 250 K is very good. The model describes well the softening of the Raman active mv as well as the evolution of the related IR combination bands upon approaching NIT. The major difference between calculated and experimental spectra concerns the broader combination bands of IR experimental spectra. This difference has two main origins: first of all, we just consider a single lattice phonon. In fact, the lattice phonon structure of a real molecular crystal is more complex and the picture of a single Peierls mode is obviously an idealization. As an example, in TTF-CA at least 6 phonon bands taking part to the Peierls mechanism of the transition have been detected in far-IR spectra [63]. Moreover, we only consider the optically active (Brillouin zone center) vibration, while also lattice modes at $q \neq 0$ (c.f. figure 1.27) enter the combinations.

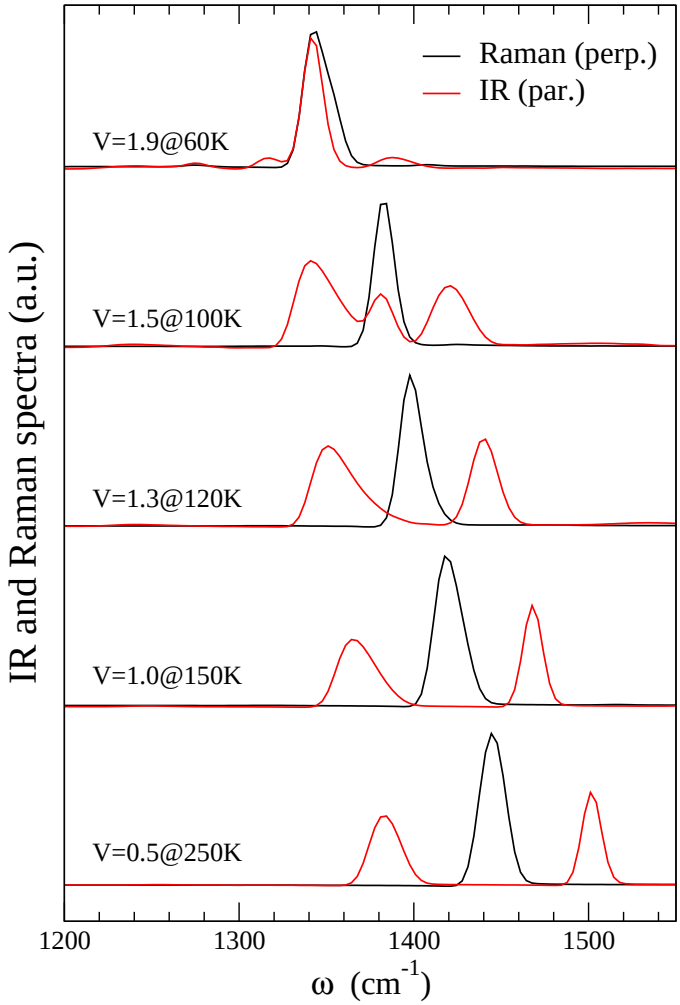

Figure 1.19: Calculated Raman spectra polarized perpendicular to stack axis (black curves) and IR spectra polarized parallel to stack axis (red curves).

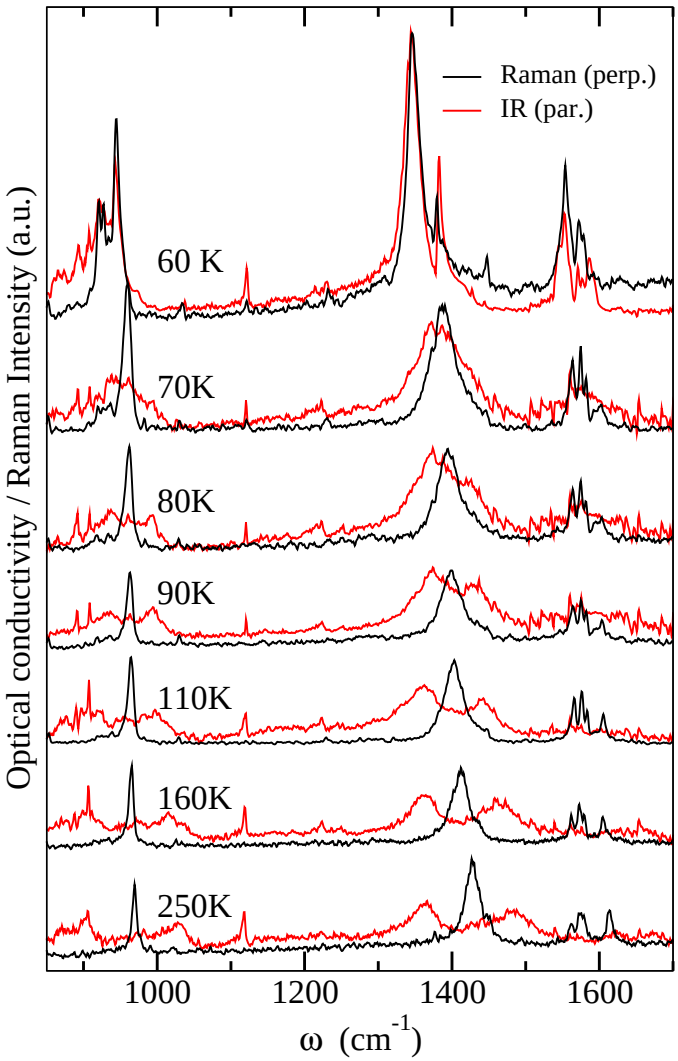

Figure 1.20: Temperature dependence of DMTTF-CA Raman spectra (black curves) and IR conductivity spectra polarized parallel to the stack axis (red curves). Data from ref. [28]

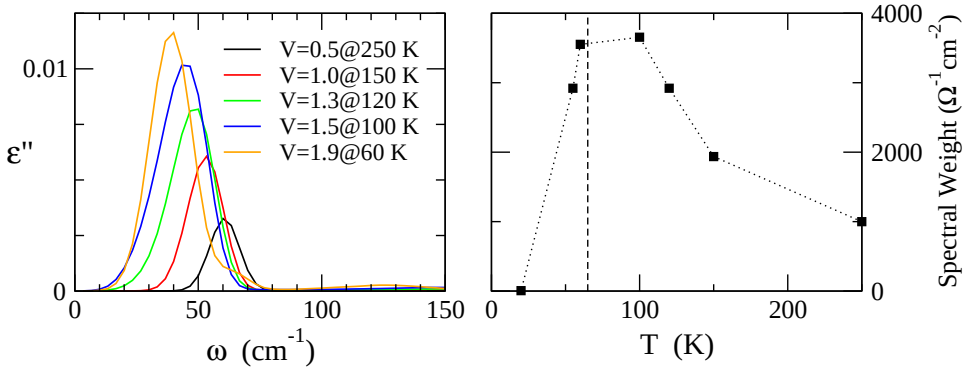

Figure 1.21: Left panel: Evolution of the IR absorption spectra, expressed as the imaginary part of the dielectric constant, with approaching NIT. Right panel: calculated spectral weight of the 0-100 cm^{-1} interval. The dotted line is a guideline for the eye.

We now turn our attention to the region of lattice phonons. Left panel of figure 1.21 shows the IR spectra, largely dominated by the absorption band of the Peierls mode. The Peierls mode softens upon approaching NIT from about 60 cm^{-1} ($V = 0.5, T = 250\ K$) to 40 cm^{-1} ($V = 1.9, T = 60\ K$). This softening is consistent with the half difference between combination bands in figure 1.19. The intensity of the Peierls mode grows upon approaching NIT as can be better appreciated in term of the 0-100 cm^{-1} spectral weight (integrated optical conductivity spectra), shown in the right panel of figure 1.21. The spectral weight grows by approximately a factor 4 upon approaching the transition (marked by a dashed line) and decreases in the I phase. The softening and the large IR intensity of the Peierls mode at NIT have already been theoretically predicted, in a treatment based on the harmonic approximation. [46, 38] These results were recently experimentally confirmed for TTF-CA [63]. Although the model is optimized to describe the continuous transition of DMTTF-CA, it is interesting to note that both the absolute values and the relative increase of the intensity of the Peierls mode are con-

sistent with the measurements on TTF-CA, where the 0-100 cm^{-1} spectral weight grows from 600 $\Omega^{-1}cm^{-2}$ at 300 K to 2000 $\Omega^{-1}cm^{-2}$ at the transition temperature of 81 K (approximated values, from figure 7 of ref. [63]). The growing intensity of the Peierls mode can be easily understood from the evolution of the explored regions of the $P(q,\delta)$ surface reported in figure 1.15. Moving toward the transition, the system approaches the region of steep P variation where oscillations along the δ coordinate induce large electronic charge fluctuations along the stack. The anharmonic simulation provided here confirms the results of the harmonic calculation [46, 38], that catches the main physics of the phenomenon, simply relating the IR intensity to the squared δ derivative of the polarization at the equilibrium $\left(\frac{\partial P}{\partial \delta}\right)_0^2$.

Figure 1.21 shows clearly that the Peierls phonon does not soften completely, as expected for a second order displacitive transition. To clarify this point we consider in detail the system with $V = 1.3$. The relevant PES (see left top panel of figure 1.13) has a single minimum at $\delta = 0$ with a vanishing curvature along δ, or, in other terms, the harmonic frequency of the Peierls mode is exactly zero. Figure 1.22 shows the IR spectra calculated with variable temperature from 120 to 5 K. The figure clearly shows that, by lowering T, the frequency of the Peierls mode shifts toward zero. This softening, obtained for spectra calculated for the same PES, is due the reduction of the amplitude of thermal fluctuations upon decreasing temperature. In fact, for vanishing T, the system explores smaller and smaller regions of the PES in the proximity of its minimum, where the surface is flat. Upon increasing T, the amplitude of thermal fluctuations widens and the system experiments finite restoring forces. This analysis demonstrates that in a displacitive transition a complete phonon softening can be observed only if the transition occurs at zero temperature. However, it is worth remembering that TCF functions are calculated in the framework of classical mechanics, while, at least at low temperature, quantum fluctuations are surely impor-

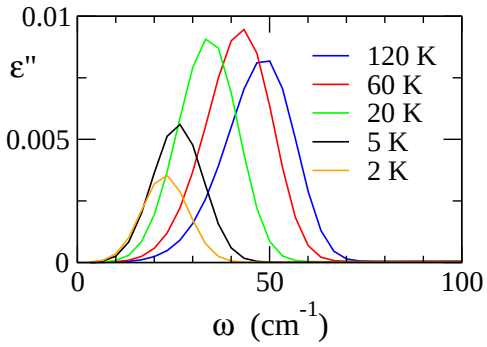

Figure 1.22: Evolution of IR absorption spectra, expressed as the imaginary part of the dielectric constant, calculated for a system with $V = 1.3$ and temperatures in the figure legend.

tant.

If the lattice phonon region of the IR spectra is adequately described within the harmonic approximation, the same spectral region of Raman spectra is dominated by anharmonicity effects. In this case we discuss the parallel Raman, related to the stack polarizability. Calculated parallel Raman spectra are shown in the left panel of figure 1.23. For $V = 0.5$ and $T = 250\ K$ (black line) the spectra is characterized by the presence of a single band around 120 cm^{-1} corresponding to twice the frequency of the Peierls mode. The Peierls mode is Raman forbidden by symmetry in the N regular phase, but overtones $n\omega_P$ with even n are Raman active. The Raman spectra for $V = 1.5$ and $T = 100\ K$ (blue line) shows a broad and highly asymmetric band, with the maximum located at 90 $cm^{-1} \approx 2\omega_P$; the anomalous bandshape is due to the large anharmonicity upon approaching NIT. A broad asymmetric band is also observed for $V = 1.9$ and $T = 60\ K$ (green line) but the frequency of the maximum, located at 63 cm^{-1}, is considerably smaller than the $2\omega_P \approx 80\ cm^{-1}$. For $V = 2.2$ and $T = 55\ K$ we notice the presence of two bands: the sharper band at lower frequency corre-

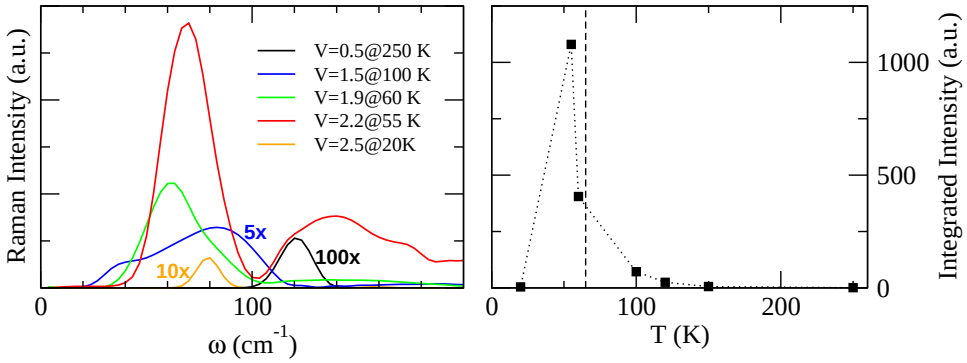

Figure 1.23: Left panel: evolution of parallel Raman spectra with approaching NIT, calculated for the parameter in the figure caption. The spectra are not on the same scale, notice multiplicative factors. Right panel: integrated Raman intensity between 0 and 150 cm^{-1} of parallel Raman spectra, normalized at the value obtained for $T = 250\ K$ ($V = 0.5$). The dotted line is a guide for the eye.

spond, even if redshifted, to $2\omega_P$. The higher frequency broad band presents a maximum at the twice of the frequency of the lower frequency one and can be interpreted as the $4\omega_P$ overtone. For larger V and smaller T, the system localizes completely within the two wells and the probability to cross the barrier vanishes. The localization within the wells implies a lowering of the symmetry and the change of the selection rules. In fact, for $V = 2.5$ and $T = 20\ K$ Raman (orange line in figure 1.23) and IR spectra (not shown) coincide and the single band observed around 90 cm^{-1} corresponds to the hardened Peierls mode.

The T-dependence of the integrated Raman intensity between 0 and 150 cm^{-1} is reported in the right panel of figure 1.23. The intensity of the parallel Raman scattering, normalized to the value obtained for $T = 250\ K$ ($V = 0.5$), increases by three orders of magnitude upon approaching NIT. The intensity of the parallel Raman spectra is related to the amplitude of

the oscillation of the α TCF and hence to $\alpha(q, \delta)$ surface and in particular to its sharp and intense peak (see figure 1.16). In fact, upon approaching NIT, the system explores larger and larger portions of the α peak as can be seen in figure 1.17. The maximum of the Raman intensity is calculated at $T = 55\ K$ ($V = 2.2$) and corresponds to a system that fully explore the polarizability peak (see right lower panel of figure 1.17). When the system localizes around the two minima, as for $V = 2.5$ and $T = 20\ K$, it explores only smooth regions of the $\alpha(q, \delta)$ surface and the parallel Raman intensity drops.

This theoretical result explains the recent observation of a growing intensity in the Raman signal below 100 cm^{-1} in DMTTF-CA [57] reported in figure 1.9. This observation, that triggered the theoretical study presented here, is however related to the perpendicular Raman, that we cannot model with the stack polarizability. Measurement in the parallel polarization are still in progress in the guest laboratory and preliminary results confirm a growing Raman intensity in the lattice phonons region below 100 cm^{-1} upon approaching NIT.

1.5 Diffuse X-ray and anomalous dispersion of lattice phonons

1.5.1 Diffuse X-ray data and theirs interpretation

In X-ray diffraction experiments any deviation from the periodic crystalline structure produces an extra diffuse scattering near Bragg peaks. Diffuse X-ray (DXR) scattering is therefore a powerful tool to study pretransitional fluctuations and/or occupational disorder. [74] An intense DXR signal was observed in the N phase of both TTF-CA and DMTTF-CA, in $(\mathbf{b}^*, \mathbf{c}^*)$ planes of the reciprocal space around Bragg reflections with integer values of the Miller index h [58, 59]. The DXR planes measured in TTF-CA at 84 K are shown in figure 1.10 at page. 37. A scan in the perpendicular direction of the reciprocal space with respect to DXR planes, reveals that the planes profiles, at least in the proximity of NIT, present an almost Lorentzian shape. DXR profiles, measured in TTF-CA at different temperatures, are shown in figure 1.24. In the original papers, DXR peaks were fitted with Lorentzian profiles to extract the intensity of the maximum I_M and the half width at half maximum $q_{1/2}$. Temperature dependence of I_M and $q_{1/2}$ in TTF-CA and DMTTF-CA are reported in figure 1.25. The intensity of DXR signal grows upon approaching NIT in both compounds but sharper peaks were observed in DMTTF-CA.

The presence of diffuse planes clearly indicates that pretransitional fluctuations occur in the stack direction, further confirming the quasi 1D nature of the transition [74, 75]. The microscopic origin of 1D fluctuations, and therefore the physical mechanism of the transition, is the subject of this section. The authors of references [58, 59] attributed the DXR signal to the presence of nanoscopic domains with characteristic length $\xi = q_{1/2}^{-1}$. These domains were identified as lattice relaxed CT exciton string (LR-CT, i.e. nanoscopic strings of a few I dimerized DA pairs embedded in the N reg-

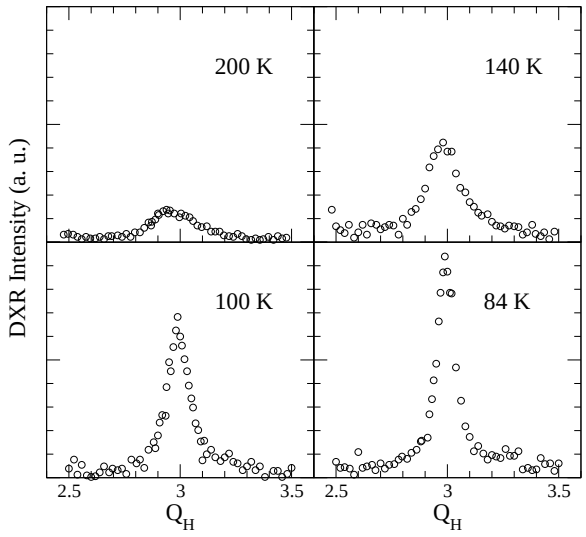

Figure 1.24: DXR profiles of TTF-CA measured with a scan along $\mathbf{a}^*$ around the (3 1 $\overline{1}$) Bragg reflection. DXR intensity is in arbitrary units but same scale is used in different panels. Data from ref. [59].

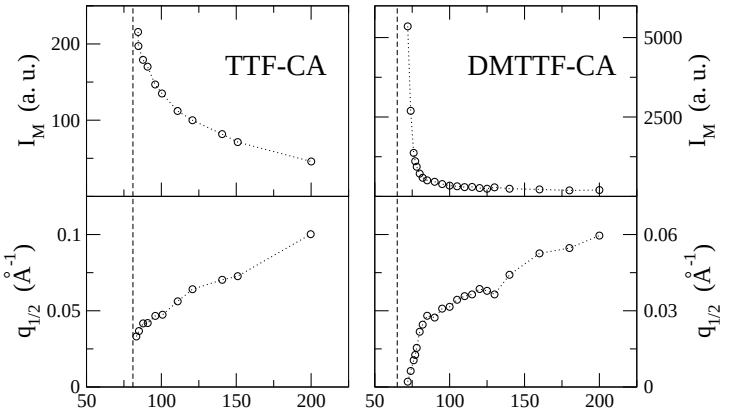

Figure 1.25: Temperature dependence of I_M (upper panels) and $q_{1/2}$ (lower panels) obtained from a Lorentzian fit of DXR profiles. Dashed lines are the transition temperature, 81 K for TTF-CA (left column) and 65 K for DMTTF-CA (right column). Dotted lines are guidelines for eye. Data from refs. [58, 59].

ular phase) and the DXR signal was presented as the first experimental observation of these excitations. The growing intensity of DXR peaks upon approaching NIT was ascribed to an increase of LR-CT concentration, while the sharpening of the peaks was interpreted as a growth of their size. From such an analysis the authors estimated that in TTF-CA LR-CT extend over 3 DA pairs at 200 K (6 DA pairs in DMTTF-CA at the same T) and over 10 DA pairs at 84 K (12 in DMTTF-CA, same T) [58, 59].

An alternative explanation of the origin of the DXR planes is however possible and attributes the 1D fluctuations to the wide molecular oscillations in the stack direction in the presence of a soft lattice mode. In fact the DXR technique was widely used in the 80's to study the soft mode that drives lattice instabilities in 1D molecular conductors. [74, 75] In this context the intensity of the DXR signal $I(q)$, is related to the dispersion law of the soft

phonon $\omega(q)$ by the simple relation [74, 75]

$$I(q,T) \propto \frac{k_B T}{\omega^2(q,T)} \tag{1.34}$$

where q is the $\mathbf{a}^*$ component of the wavevector, k_B the Boltzmann constant and T the absolute temperature. The sharp DXR profiles observed in TTF-CA and DMTTF-CA require however a strong dispersion of the relevant phonon, that is anomalous for the Peierls mode, that is the Brillouin zone center mode ($q = 0$) of an *optical* branch. This was the basis for rejecting the soft mode interpretation in favor of LR-CTs in one of the original papers [59]. However electron-phonon (e-ph) coupling is extremely effective in 1D systems with delocalized electrons and an anomalous dispersion of optical phonons is well known in polyacetylene [39].

The soft-mode interpretation of DXR data is strongly supported by a comparison between DXR data and vibrational spectra. In fact equation (1.34) relates the frequency of the Peierls mode $\omega(0,T)$ to the height of DXR peaks $I(0,T)$. Reliable estimates of the frequency of the Peierls mode were obtained from the analysis of combination bands in mid-IR spectra [55, 28]. The estimated temperature dependence of the frequency of the Peierls mode in DMTTF-CA and TTF-CA is reported in figure 1.26 (circles). On the same figure red diamonds show (on an arbitrary scale) the T-evolution of the height of the DXR profiles, from data in references [58, 59]. The striking agreement between these two independent sets of data strongly supports the soft mode interpretation of the DXR data. However, to confirm this hypothesis, a detailed modeling of the lattice dynamics in the presence of e-ph coupling is required to address the issue of the anomalous dispersion of the optical phonon branch around the Brillouin zone center.

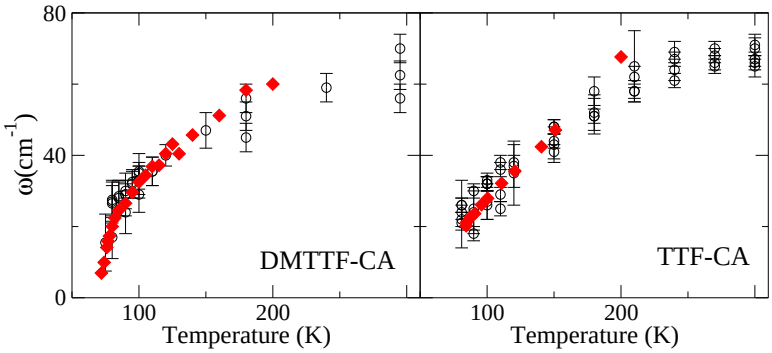

Figure 1.26: Temperature dependence of the soft mode frequency in TTF-CA (left panel) and in DMTTF-CA (right panel), obtained from mid-IR and Raman spectra (circles) [55, 28] and from DXR data (diamonds) [58, 59].

1.5.2 Anomalous dispersion of optical phonons at NIT

To calculate the lattice phonons dispersion we adopt the classical theory of harmonic crystals. We consider a linear chain of N sites ($N_c = N/2$ cells) and lattice constant a. A set of vibrational coordinates, x_i, measures site displacements from the equilibrium position of the regular chain and different masses $m_{D/A}$ are assigned to D (odd sites) and A (even sites) molecules. In the absence of e-ph coupling the vibrational problem reduces to the well known problem of a linear chain with a diatomic basis. [76] The potential energy of the chain reads

$$V_{ph} = \frac{1}{2} K \sum_i (x_i - x_{i+1})^2 \tag{1.35}$$

where K is the elastic constant of the regular lattice.

The squared frequencies of the normal modes of the chain are obtained from the eigenvalues of the dynamical matrix

$$F_{ij} = \frac{\partial^2 V_{ph}}{\partial \tilde{x}_i \, \partial \tilde{x}_j} \tag{1.36}$$

where $\tilde{x}_i = \sqrt{m_i}\ x_i$ are the mass weighted cartesian coordinates, with

$m_i = m_D$ on odd (D) sites and $m_i = m_A$ on even (A) sites. In order to obtain the dispersion relation of phonon frequencies we combine the cartesian coordinate according to the wavevectors of the reciprocal space:

$$\begin{aligned} \xi_q^D &= \sqrt{\frac{2}{N}} \sum_j^{odd} e^{-iq\frac{j+1}{2}} \tilde{x}_{\frac{j+1}{2}} \\ \xi_q^A &= \sqrt{\frac{2}{N}} \sum_j^{even} e^{-iq\frac{j}{2}} \tilde{x}_{\frac{j}{2}} \end{aligned} \tag{1.37}$$

where $q = (0, \pm 1, \pm 2 \cdots \pm (N_c - 1)/2) 2\pi/N_c$ are the wavevectors (N_c is odd for simplicity) in the first Brillouin zone. Because of the lattice translational symmetry, only modes labelled by the same wavevector are mixed and the dynamical matrix factorizes in $N/2$ two-dimensional blocks F_q:

$$\begin{aligned} F_q &= \begin{pmatrix} \frac{\partial^2 V_{ph}}{\partial \xi_q^D \partial \xi_q^D} & \frac{\partial^2 V_{ph}}{\partial \xi_q^D \partial \xi_q^A} \\ \frac{\partial^2 V_{ph}}{\partial \xi_q^A \partial \xi_q^D} & \frac{\partial^2 V_{ph}}{\partial \xi_q^A \partial \xi_q^A} \end{pmatrix} = \\ &= \begin{pmatrix} \frac{2K}{m_D} & -\frac{K}{\sqrt{m_D m_A}}(1 + e^{iq}) \\ -\frac{K}{\sqrt{m_D m_A}}(1 + e^{-iq}) & \frac{2K}{m_A} \end{pmatrix} \end{aligned} \tag{1.38}$$

The eigenvalues of F_q are the squared frequencies of the normal modes with wavevector q. Lattice phonons dispersion laws are therefore calculated diagonalizing matrix (1.38) for each wavevector in the first Brillouin zone. Optical and acoustic branches for the linear chain with diatomic basis, calculated for the molecular masses of DMTTF-CA and K fixed as to get $\omega(0) = 110\ cm^{-1}$, are plotted in the upper panel of figure 1.27. Since the Peierls phonon is the $q = 0$ optical mode, we are interested in the optical branch (red curve), characterized by an almost dispersionless behavior around the zone center.

We now introduce the coupling between lattice and electronic systems, described by the modified Hubbard (MH) Hamiltonian with Peierls coupling

$$H = \Gamma \sum_i (-1)^i \ \hat{n}_i + \sum_{i,\sigma} [t_0 + \gamma(x_{i+1} - x_i)] \ (a^\dagger_{i,\sigma} a_{i+1,\sigma} + \ H.c.) \tag{1.39}$$

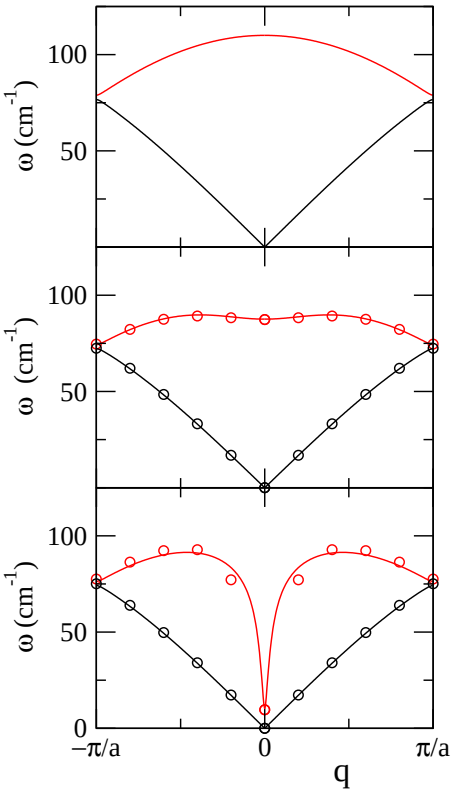

Figure 1.27: Acoustic (black) and optical (red) phonon branches of a mixed stack with masses relevant to DMTTF-CA and $\omega_0(0) = 110\ cm^{-1}$. Upper panel reports the dispersion laws of an unperturbed lattice ($\varepsilon_d = 0$), central and middle panels refer to system with e-ph coupling with $\rho = 0.22$ and $\rho = 0.46$ respectively. Circles are MH results, calculated for $N = 20$ and $\varepsilon_d = 0.27$ and $\varepsilon_d = 0.2$ in middle and lower panels, respectively. Continuous curves are SF results obtained for $N = 902$ and $\varepsilon_d = 0.4$ in both panels.

where t_0 is the CT integral of the regular chain (adopted as the energy unit) and γ the e-ph coupling constant, related to the relaxation energy upon dimerization by the relation $\gamma^2 = \varepsilon_d K$. At variance with e-ph Hamiltonians presented in chapter 1.2.3, where only the coupling to the Peierls mode was considered, here all the lattice modes are included in the picture, in order to calculate phonons dispersion laws. Holstein coupling and intersite Coulomb interactions are implicitly included in a renormalization of Γ, that will be considered as the parameter that induce the NIT.

In the framework of the harmonic approximation, e-ph coupling introduces an additional contribution to the force constant matrix corresponding to the second derivatives of the electronic ground state energy E versus sites displacements:

$$F_{ij}^{e-ph} = \frac{\partial^2 E}{\partial \tilde{x}_i \, \partial \tilde{x}_{i+j}} = \frac{\gamma^2}{\sqrt{m_i \, m_{i+j}}} (\Pi_{j-1} - 2\Pi_j + \Pi_{j+1}) \tag{1.40}$$

where the bond-bond polarizabilities Π_j (BBP) are purely electronic quantities, defined as

$$\Pi_j = -\frac{\partial^2 E}{\partial t_i \, \partial t_{i+j}} \tag{1.41}$$

The BBPs of the MH model, calculated as numerical derivatives of the ground state energy of a 20 sites chain, are shown in the left upper panel of figure 1.28. BBPs oscillates between positive and negative values, reflecting the tendency of delocalized electrons to push the system toward dimerization. Black and red circles refer to systems with $\rho = 0.22$ ($\Gamma = 1$) and $\rho = 0.46$ ($\Gamma = -0.2$) respectively. In a system relatively far from NIT, as for $\rho = 0.22$, e-ph coupling is mild and Π_j decrease rapidly with j. Closer to NIT, for $\rho = 0.46$, BBPs are larger in magnitude and acquire a long tail, that can be only partially appreciated with a 20 sites chain.

Much as in polyacetylene, [4] the coupling to delocalized electrons leads to long range BBPs, resulting in long-range force constants. The effect of BBPs

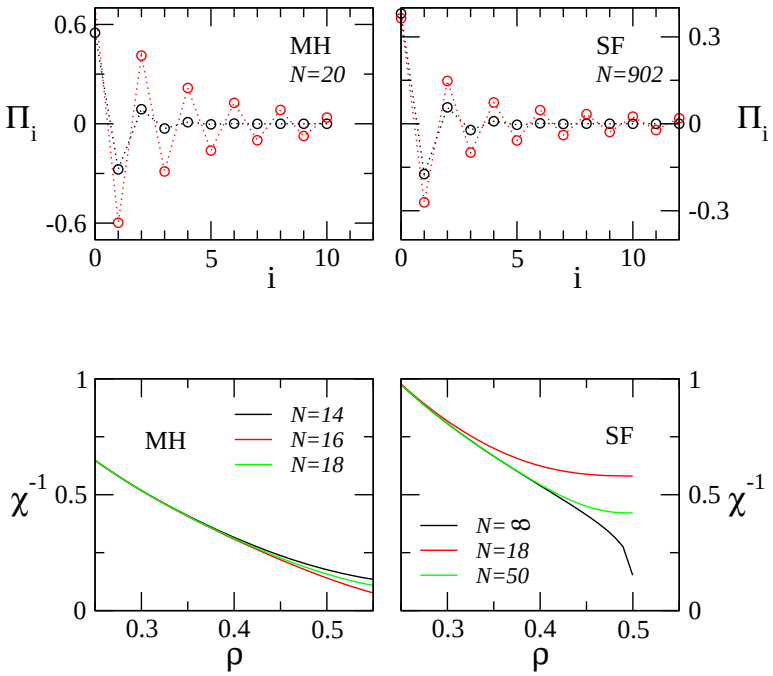

Figure 1.28: Upper panels: BBPs of MH (left) and SF (right) model, calculated for systems with $\rho = 0.22$ (black circles) and $\rho = 0.46$ (red circles). Dotted lines are guides for the eye. Lower panels: inverse electronic susceptibility of MH (left) and SF model (right panel). Size of the systems are indicated in respective the legends.

in figure 1.28 on the phonon dispersion is shown in middle and lower panels of figure 1.27 for systems with $\rho = 0.22$ and $\rho = 0.46$ respectively. Acoustic and optical branch frequencies of a 20 sites MH chain are marked with black and red circles respectively. Minor effects are observed in the acoustic branch, while upon approaching NIT, an anomalous dispersion (Kohn-like anomaly) develops in the optical branch. The largest softening occurs at $q = 0$ (Peierls mode) where a simple relation holds for the optical branch frequency:

$$\omega(0) = \omega_0(0)\sqrt{1 - \varepsilon_d \chi(\Gamma)} \tag{1.42}$$

where $\chi(\Gamma)$ is the electronic susceptibility defined as

$$\chi(\Gamma) = - \left. \frac{\partial^2 E(\Gamma, \delta)}{\partial \delta^2} \right|_{\delta=0} \tag{1.43}$$

where δ, as usual, is the amplitude of dimerization. The susceptibility is a purely electronic quantity that governs the lattice instability and the related softening of the Peierls mode. [32] The (inverse) susceptibility of MH chains of $N = 14$, 16 and 18 sites is plotted in the left lower panel of figure 1.28. Size effects are evident for $\rho > 0.4$, signaling the increasing electronic delocalization upon approaching NIT. The susceptibility grows moving toward NIT and diverges at the metallic N-I boundary of an infinite chain, where the system is unconditionally unstable to dimerization. According to equation (1.42), the growth of χ results in the softening of the Peierls mode up to $\varepsilon_d = \chi^{-1}$, where the frequency vanishes and the system dimerizes. The inverse susceptibility corresponds therefore to the critical value of ε_d.

The softening of the Peierls mode and the related anomalous dispersion of the optical branch around $q = 0$ are direct consequences of the coupling between phonons and delocalized electrons. This result is obtained within the MH model, the reference model for CT salts, that fully accounts for electronic correlations. However, MH calculations are computationally very demanding and chains longer than 20 sites cannot be treated, resulting in

dispersion laws with only few points in the first Brillouin zone, as in figure 1.27. To obtain a higher q-space resolution, as required to fit DXR data, longer chains must be considered. We therefore adopt an uncorrelated model for the electronic system, i.e. the spinless fermion (SF) model described in section 1.2.6. SF model is the uncorrelated counterpart of the MH model and describes a collective CT from D and A sites with decreasing Γ. The SF model is exactly soluble and relevant quantities, as stack ionicity or electronic ground state energy, can be calculated trough analytic expressions (see section 23). BBP in the SF model can be calculated using the following sum over state expression:

$$\Pi_j = 2 \sum_{k,l} \frac{\langle GS|\hat{b}_i|kl\rangle\langle kl|\hat{b}_{i+j}|GS\rangle}{\epsilon_l - \epsilon_k} \tag{1.44}$$

where GS is the ground state, $|kl\rangle$ is the excited state created from the GS by promoting a fermion from the k-th filled orbital to the l-th empty orbital, $\hat{b}_i = (a_i^\dagger a_{i+1} + \text{H.c.})$ is the bond order operator and ϵ_k is k-orbital energy (see section 1.2.6). BBPs for a SF model with 902 sites chain are shown in the right upper panel of figure 1.28. Results refer to a systems with $\rho = 0.22$ ($\Gamma = 0.75$, black circles) and $\rho = 0.46$ ($\Gamma = 0.06$, red circles). The comparison with the MH counterpart (left upper panel of the same figure) is straightforward. As for MH model, BBP obtained with the SF model oscillates between positive and negative values and show a slower decrease with the intersite distance in the system closer to NIT. The smaller absolute values of SF BBPs with respect to the MH counterpart indicates a stronger e-ph coupling in the correlated model. [77]

The electronic susceptibility toward dimerization is expressed in the SF model as:

$$\chi = -\left.\frac{\partial^2 E}{\partial \delta^2}\right|_0 = \frac{1}{N}\sum_k \frac{\sin^2 k}{\sqrt{\Gamma^2 + 4\cos^2 k}} \tag{1.45}$$

where the sum runs over the k wavevectors of the first Brillouin zone. In

the $N \to \infty$ limit, the susceptibility is expressed in term of complete elliptic integrals as follows

$$\chi = \frac{4}{\pi\sqrt{\gamma^2+4}}\ \mathrm{cel}(q_c, p=1, a=0, b=1) \tag{1.46}$$

with $q_c^2 = \Gamma^2/(\Gamma^2+4)$ and $\mathrm{cel}(q_c, p, a, b)$ defined in equation 1.25 (page. 25). [47] The inverse electronic susceptibility of the SF model is reported in the right lower panel of figure 1.28, and presents a qualitatively similar behavior as observed for the MH model (left lower panel): χ grows with approaching NIT and diverges at $\rho = 0.5$ ($\Gamma = 0$) for an infinite chain, marking the unconditional Peierls instability of a half filled 1D metal. Since in the SF model the I phase is equivalent to a N phase with exchanged D and A sites, results for $\rho > 0.5$ are not shown. Again, the smaller values of the SF susceptibility with respect to the MH analogous confirm the stronger e-ph of the correlated model. [77] Finite size effects are more important than in the correlated model.

The phonon dispersion laws, calculated with the SF model for a 902 sites chain, are presented in middle and lower panels of figure 1.27, for systems with $\rho = 0.22$ and $\rho = 0.46$, respectively. Black and red continuous lines correspond to optical and acoustical branches and are in excellent agreement with MH results (black and red circles), calculated for same values of ρ, and with $\varepsilon_d = 0.4$ (the same $\omega(0)$ is imposed in both models). The softening of the Peierls mode and the related Kohn-like anomaly in the optical phonon branch around $q = 0$ are therefore manifestations of the coupling between delocalized electrons and phonons in a 1D system. Electronic correlation quantitatively alter the picture, generally enhancing the effect of e-ph coupling, [77] but the basic physics governing the dimerization instability is grasped by the uncorrelated SF model.

A summary of the effects of the e-ph coupling on the optical branch upon approaching NIT, is provided in figure 1.29. For $\Gamma = 1$ the system is

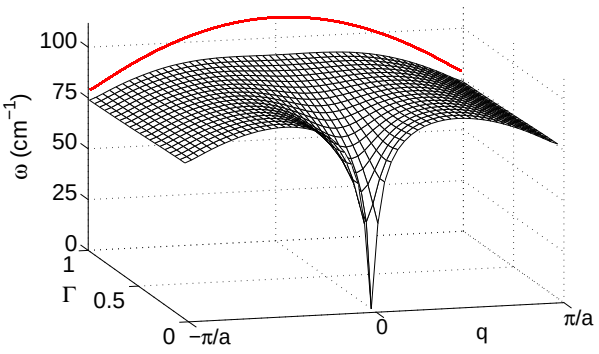

Figure 1.29: Γ dependence of the optical branch calculated for molecular masses relevant for DMTTF-CA, $\varepsilon_d = 0.4$, $\omega_0 = 110\ cm^{-1}$ on 902 sites. The continuous red line is the dispersion curve of the unperturbed harmonic lattice ($\varepsilon_d = 0$).

still far from NIT ($\rho = 0.22$) but the Peierls mode is already considerably softer than in the uncoupled lattice ($\varepsilon_d = 0$, red line in background). Upon approaching NIT, the Peierls mode undergoes a progressive and complete softening according to equation (1.42) and a sharp Kohn-like anomaly in the optical branch develops at $q = 0$.

1.5.3 Fit of diffuse X-ray profiles

With the dispersion relation of the optical branch $\omega(q)$ in hand, we can model the DXR profiles. DXR profiles $I(q)$ are measured as a function of T, while SF dispersion laws are computed as a function of Γ. In both cases the profile is characterized by the peak height, $I_M = I(0)$, and by the half-width at half-maximum $q_{1/2}$, reported for TTF-CA and DMTTF-CA in figure 1.25. The calculated DXR profiles $I(q)$ in figure 1.30 are based on equation (1.34) with $\omega(0)$ taken from vibrational data and the best-fit parameters, ε_d and $\omega_0(0)$ in the caption. Insets b and e specify $\Gamma(T)$ for DMTTF-CA and TTF-

CA, respectively. An almost linear $\Gamma(T)$ relation is obtained in both cases. The measured and calculated values of $q_{1/2}$, shown in insets c and f are in excellent agreement, especially close to the transition.

DXR profiles in mixed-stack CT salts close to NIT are quantitatively explained by the softening of the dimerization mode and the related anomaly in the optical phonon branch. The sharp DXR peaks observed in DMTTF-CA were previously assigned to the presence of long LR-CT excitations [58], whereas the broader signals in TTF-CA were ascribed to shorter domains [59]. Here the difference between the two systems is naturally related to their different transitions. DMTTF-CA undergoes a continuous (or almost continuous) dimerization transition [28]: $\rho(T)$ presents a continuous evolution, the Peierls phonon frequency $\omega(0)$ softens to zero (or almost so [28]), and the related deep anomaly in the dispersion law leads to sharp DXR peaks. On the other hand, only incipient soft-mode behavior is observed in TTF-CA, whose discontinuous NIT at 81 K interrupts the softening [55]. As a result, the dispersion anomaly does not fully develop and relatively broad DXR peaks are observed.

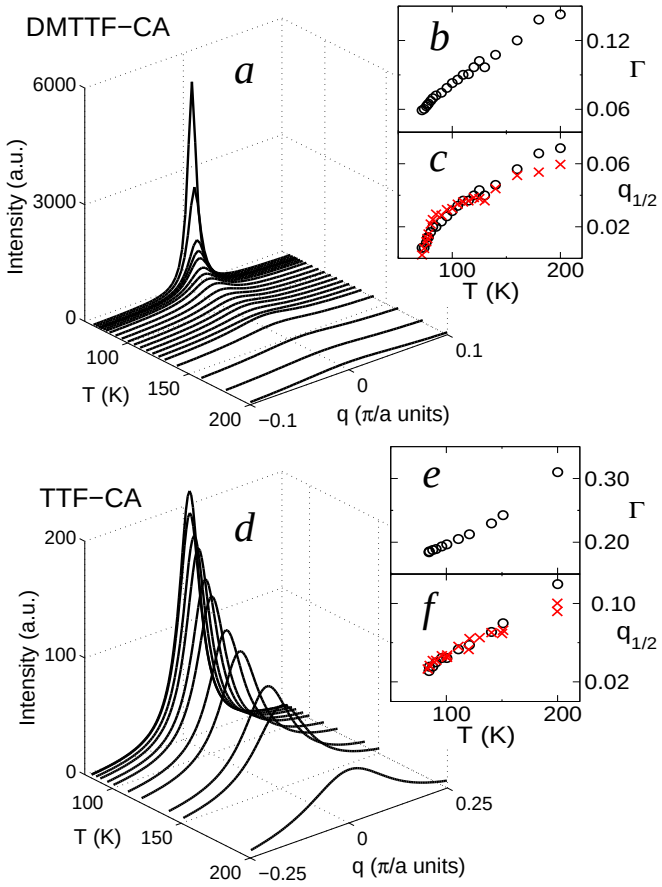

Figure 1.30: Main panels (a, d): Temperature evolution of DXR peaks as calculated in the SF model. Panel a: DMTTF-CA, $\varepsilon_d = 0.4$, $\omega_0(0) = 110\ cm^{-1}$; panel d: TTF-CA, $\varepsilon_d = 0.55$, $\omega_0(0) = 130\ cm^{-1}$. Insets d and e show the $\Gamma(T)$ relation. Insets c and f compare the calculated (black circles) and experimental (red crosses) values of $q_{1/2}$.

1.6 Conclusions

Although the scenario of NIT is a very complex one, a coherent picture of the physics governing the transition in now emerging. This picture is provided by the modified Hubbard model accounting for Peierls coupling to lattice phonons and Holstein coupling to molecular vibrations. [33, 46, 38, 37] The model, despite its simplicity, gives a quantitative explanation of the rich phenomenology related to NIT, as thoroughly discussed in this chapter.

The modified Hubbard model describes a system where delocalized electrons in 1D are responsible for a nonlinear behavior related to a collective CT from the D to the A molecules of the stack. Electrostatic interactions and Holstein coupling to molecular vibrations confer cooperativity to the system and enhance its nonlinearity, leading to a discontinuous N-I crossover (charge instability) and to the related phenomenon of multistability. [33, 37] At the same time, the coupling between electrons and lattice phonons results in a spontaneous symmetry breaking phenomenon, fairly common in 1D systems, the stack dimerization (generalized Peierls instability). [32, 33, 37] The interplay between the charge instability, leading a discontinuous crossover, and the intrinsically second-order dimerization instability, explains the main features of the phase diagram of mixed stack CT crystals. [37] In these systems the intimate entangling between electronic and vibrational degrees of freedom is amplified by the presence of electronic instabilities. In fact, upon approaching NIT, the electronic system becomes largely susceptible, and vibrations are responsible for most of the, only apparently, anomalous features observed around NIT. The modified Hubbard model with coupling to adiabatic vibrations offers a reliable tool to rationalize this complex behavior.

The large values of the static dielectric constant observed at NIT in many CT crystals [53, 54] represent a clear manifestation of the effectiveness of

e-ph coupling. As recognized by Painelli, Soos *et al.*, [46, 38] the dielectric anomaly is originated by the electronic charge fluxes along the stack induced by the oscillations of the soft Peierls mode and to its huge IR intensity.

The soft Peierls mode is also responsible for the presence of the DXR signal observed in TTF-CA and DMTTF-CA. [59, 58] In section 1.5 we reported the calculations of the phonon dispersion laws of a mixed stack in the presence of e-ph coupling. The coupling between lattice phonons and delocalized electrons, quite irrespectively on electronic correlations, is responsible for the appearance of long-range force constants resulting in an anomalous dispersion (Kohn-like anomaly) of optical phonons around the Brillouin zone center. The Kohn-like anomaly quantitatively explains the sharp DXR profiles experimentally observed.

The most striking effects of e-ph coupling are seen in vibrational spectra. [52, 55, 28, 53, 54, 63, 57] In fact, e-ph coupling is responsible for the softening of the coupled modes and for their strong anharmonicity, with nontrivial effects in IR and Raman spectra. In section 1.4 a detailed simulation of IR and Raman spectra of a mixed stack CT crystal undergoing a continuous NIT is presented. The simulation is based on an original implementation of the approach of TCF to spectroscopy. The method consists in a sort of minimal molecular dynamics simulation, where the vibrational dynamics of the system is governed by the ground state PES. Minimal because the (intrinsically anharmonic) ground state PES, obtained from the modified Hubbard model with Peierls and Holstein coupling, describes just two relevant coordinates. Polarization and polarizability, whose TCF are directly related to the IR and Raman spectra, are calculated within the modern theory of polarization in dielectrics. Despite its simplicity, this approach allows to fully relax the harmonic approximation and satisfactorily reproduce the complex and interesting behavior of mixed stack CT crystals at NIT.

The results of the simulations further confirm previous theoretical results

based on the harmonic approximation, as the softening of the frequency of Holstein and of Peierls modes, and the increasing IR intensity of the latter upon approaching NIT. [46, 38] The simulations definitively confirm the interpretation of the mid-IR sidebands as combinations of a Raman active mv and of an effective soft Peierls mode. [55, 28] More interestingly, this approach is able to catch new and interesting phenomena, fully governed by anharmonicity, as the appearance of intense features in the lattice phonon region of Raman spectra in the close proximity of NIT. [57] The enhancement of the low-frequency Raman signal is due to vibrations, that in the close proximity of NIT efficiently modulate the electronic properties, leading to a orders of magnitude increase of the polarizability.

We conclude emphasizing the fact that the method here developed for the simulation of vibrational spectra of mixed stack CT crystal provides a reliable and simple way to get an insight in extremely complex behaviors. This method is extremely general and can be applied in systems where charge, spin and vibrational degrees of freedom are strongly coupled, as charge ordering systems, ferroelectrics or multiferroics.

Chapter 2

Bistability in Crystals of Valence Tautomeric Molecules

2.1 Introduction: the valence tautomerism of Fc-PTM

Ferrocene-perchlorotriphenylmethyl (Fc-PTM) is a valence tautomeric radical where the Fc group, a good electron donor (D), is linked trough a vinylenic π-bridge to PTM, a very stable radical with electron acceptor (A) properties [78, 79]. Figure 2.1 shows the two resonating structures (or mesomeric forms) of Fc-PTM and a view of the crystal structure of this compound. Fc-PTM radical combines a fully reversible electrochemical switchability with the high nonlinear optical responses of DA dyads [78, 80]. Moreover, the presence of an unpaired spin confers to Fc-PTM a magnetic interest. In view of its chemical, optical and thermal stability, Fc-PTM is therefore an interesting system for the development of multifunctional

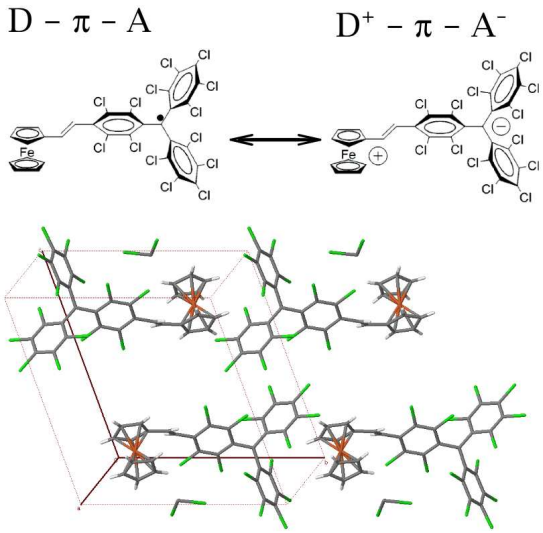

Figure 2.1: The two mesomeric forms of Fc-PTM (top panel) and a view of the crystal structure of Fc-PTM crystal (bottom panel).

molecular materials.

Optical absorption spectra of Fc-PTM collected in solution, reported in figure 2.2, reveal that solvated Fc-PTM is a largely neutral DA molecule, i.e. it resembles the D-π-A resonating structure [78]. The CT absorption band, located in the near infrared region around 11000 cm^{-1}, is related to the photoexcitation towards a largely ionic (or zwitterionic) D^{+}-π-A^{-} state. In other terms, in solution the D^{+}-π-A^{-} mesomeric form of Fc-PTM is more than 1.3 eV higher in energy than the D-π-A.

However, Mössbauer spectra on Fc-PTM polycrystalline samples, reported in figure 2.9, reveal an interesting temperature dependence valence tautomerism [79]: the Mössbauer spectrum recorded at 4.2 K shows only the typical doublet of Fc [81], but with increasing temperature a new dou-

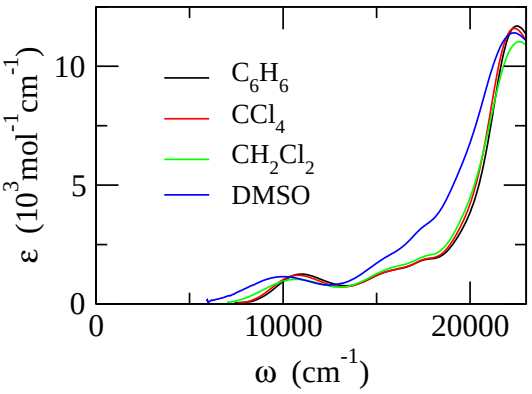

Figure 2.2: Fc-PTM absorption spectra of in organic solvents of different polarity (see legend) from ref. [78].

blet with smaller splitting, characteristic of the ferrocinium cation Fc^+ [81], grows in at the expense of the Fc doublet. The conversion is gradual and fully reversible up to room temperature, as also confirmed by subtle changes in the magnetization data [79]. Although hysteresis was not observed, it is worth mentioning that the Mössbauer spectrum taken of a rapidly cooled sample at 70 K reveals about a 30% of trapped Fc^+ component [79]. These findings demonstrate that at room temperature both the D-π-A and D^+-π-A^- forms of Fc-PTM coexist in similar proportions [79], suggesting an energy gap between the two forms not larger than the thermal energy.

The simultaneous stability of the two mesomeric D-π-A and D^+-π-A^- forms in crystals of DA molecules, resulting from cooperative electrostatic interactions, was theoretically predicted a few years ago by Terenziani and Painelli [20, 82]. However, an experimental proof of the predicted mechanism was lacking. Here a detailed modeling of Fc-PTM crystal strongly supports the suggestive hypothesis that the coexistence shown by Mössbauer spectra can be explained in term of bistability induced by electrostatic interactions. In the next section the general bottom up modeling strategy for crystal of

DA molecules is presented. Two alternative approaches to the bottom up modeling of Fc-PTM are then proposed in sections 2.3 and 2.4. Conclusions and guidelines for the synthesis of bistable crystals of valence tautomeric molecules are finally provided in section 2.5.

2.2 Bottom up modeling of molecular crystals

The bottom up modeling strategy was developed in the guest laboratory to describe linear and nonlinear optical properties of supramolecular architectures (including crystals, films, aggregates and clusters) of DA-bases chromophores. [83] DA-based chromophores (or dyes) are a class of organic molecules characterized by the presence of D and A groups connected by a π-conjugated bridge. These molecules are actively investigated since 90's due to their large nonlinear optical responses. [7] DA-based chromophores include, besides the most popular dipolar DA molecules, as Fc-PTM, also multibranched system as quadrupolar (DAD or ADA)[84] and octupolar (DA_3 or AD_3) chromophores. [85] The bottom up approach was originally developed for the study of excited states, but it can surely be applied to describe ground state properties, as relevant for Fc-PTM. Before discussing its application to Fc-PTM crystal, we shortly describe the bottom up modeling strategy.

We consider supramolecular architectures where intermolecular distances are larger than Van der Waals radii, that the overlap between molecular orbital of different molecules is negligible. The general Hamiltonian of a crystal of non-overlapping molecules can be written as: [20, 82]

$$H = \sum_i \hat{h}_i + \frac{1}{2} \sum_{i,j} \hat{V}_{ij} \tag{2.1}$$

where the sums run on molecular sites, $\hat{h}_i$ is the Hamiltonian of the i-th molecule, and $\hat{V}_{ij}$ is the operator that describes the interaction between molecules at i and j sites.

Different levels of approximation are possible for the molecular Hamiltonian. The most detailed description of the molecular unit is offered by quantum chemical Hamiltonians. However, these molecular Hamiltonians leads to a very complex problem for the molecular crystal, which moreover applies

only to the specific compound at hand. In order to keep the model as simple and general as possible, we adopt an essential state picture for the molecular units. The low energy physics of DA-based molecules is in fact governed by intramolecular CT and can be approximately described accounting only for a few relevant basis states, corresponding to the molecular resonance structures. In the simple case of the DA molecules the basis states correspond to the D-π-A and D^+-π-A^-mesomeric forms, while more states are needed for multibranched chromophores. [83] Few states models, extended to account for molecular vibrations and solvation interaction, are validated by reproducing the evolution of absorption and/or fluorescence spectra in solvent of different polarity. Even more important, a set of *environmentally independent* molecular parameters can be extracted from the analysis of the optical spectra of the relevant compound. This specific molecular information can then be used to describe the molecule in the crystal. [86, 87, 83, 88]

In traditional molecular crystals intermolecular interactions are generally weak, leading most often to additive behavior. This is not the cases of DA-based chromophores where the presence delocalized π electrons resonating between D and A groups, confer (multi)polar and (hyper)polarizable properties, resulting in strong electrostatic intermolecular interactions. Electrostatic interactions, represent an additional and powerful source of nonlinearity in these materials, resulting in important collective and cooperative effects that show up in nonlinear optical responses, multielectron transfer and, as we will see in detail here, bistability [89, 20, 90, 83, 88]. Common pictures for interactions in molecular crystals account electrostatic interaction between molecular point dipoles. This approximation, however, necessarily fails when intermolecular distances are comparable with the molecular size, as in common DA dyes. An alternative approach is adopted here, that assumes electrostatic interactions between extended charge distribution. This approach presents the further advantage that, as we will see in the case

of Fc-PTM, quantum chemical calculations can be directly mapped on few state models, leading to reliable evaluation of the interaction strength.

The work on Fc-PTM represents an interesting development of a research activity carried on in the host laboratory in the field of CT molecular materials. In particular the bottom up modeling of supramolecular system of organic quadrupolar (DAD or ADA) molecules was investigated in detail by the author of this thesis before starting the Ph.D. activity. Combining a molecular description, based on an essential three-state model [89], and electrostatic interactions between extended charge distributions, we demonstrated the failure of common approaches based on point dipole interactions and perturbative treatments. More interestingly, we showed that electrostatic interactions represent a powerful tool to further enhance the strong two-photon absorption of quadrupolar dyes. [90] This work is part of an invited review paper on the effects of electrostatic interaction on nonlinear optical properties of supramolecular systems of DA-based organic chromophores. [83]

We remark that bottom up modeling strategy provides a simple but reliable description of DA-based supramolecular architectures: by combining information on the molecule (obtained from optical spectroscopy and rationalized in term of few state models) with proper models for intermolecular electrostatic interactions, collective and cooperative properties of supramolecular system of (multi)polar and (hyper)polarizable molecules can be fully described. Two alternative bottom up approaches to describe Fc-PTM crystal are provided here: in the first one (presented in the next section), we adopt the standard two-state model for DA molecules. In the second (section 2.4), we introduce a three-model model, in order to better reproduce the spectral properties of Fc-PTM in solution.

2.3 Bottom up with the two-state DA model

2.3.1 Two-state model for Fc-PTM and Me_9Fc-PTM

The low-energy physics of Fc-PTM is governed by the charge resonance shown in figure 2.1. In close analogy with closed shell DA chromophores, we describe the Fc-PTM radical in terms of a minimal model that just accounts for two essential electronic states, D-π-A and D^+-π-A^-, corresponding to the two resonating structures in figure 2.1 [91, 92, 93, 94]. The electronic Hamiltonian reads

$$\hat{h}_{el} = 2z\ \hat{\rho} - \tau\ \hat{\sigma}^x \tag{2.2}$$

where

$$\hat{\rho} = \begin{pmatrix} 0 & 0 \\ 0 & 1 \end{pmatrix} \tag{2.3}$$

is the ionicity operator, $2z$ is the ionization energy, i.e. the energy required to separate the charge in a DA molecule, τ is the hybridization energy, that drives the system toward mixed-valence states and $\hat{\sigma}^x$ is the Pauli matrix that mixes the two basis states. The diagonalization of Hamiltonian (2.2) gives closed expressions for the ground and excited states:

$$\begin{aligned} |g\rangle &= \sqrt{1-\rho}\ |D^+A^-\rangle + \sqrt{\rho}\ |D^+A^-\rangle \\ |e\rangle &= -\sqrt{\rho}\ |D^+A^-\rangle + \sqrt{1-\rho}\ |D^+A^-\rangle \end{aligned} \tag{2.4}$$

where

$$\rho = \frac{1}{2}\left(1 - \frac{z}{\sqrt{z^2+\tau^2}}\right) \tag{2.5}$$

is the expectation value of the ionicity operator and measures the charge transferred from D to A, or, equivalently, the fraction of unpaired spin on the Fc fragment. For positive z/τ the ground-state is neutral (N, $\rho < 0.5$), and becomes ionic (or zwitterionic) (I, $\rho > 0.5$) for negative z/τ.

As recognized by Mulliken [95] the D^+-π-A^- state is characterized by a large dipole moment μ_0, so that all other matrix elements of the dipole moment operator on the chosen basis can be neglected. With this approximation, relevant spectroscopic quantities are written as a function of ρ:

$$\omega_{CT} = \tau \frac{1}{\sqrt{\rho(1-\rho)}} \tag{2.6}$$

$$\mu_{CT} = \mu_0 \sqrt{\rho(1-\rho)} \tag{2.7}$$

$$\mu_g = \mu_0 \rho \tag{2.8}$$

$$\Delta\mu = = \mu_e - \mu_g = \mu_0 (1-2\rho) \tag{2.9}$$

where ω_{CT} is the transition frequency, μ_{CT} the transition dipole moment, μ_g (μ_e) is the ground (excited) state dipole moment and $\Delta\mu$ is the mesomeric transition dipole moment.

To account for the relaxation of the molecular geometry that accompanies the CT and is responsible for the appearance of the Franck-Condon structure in absorption spectra, we introduce an effective adiabatic vibrational coordinate Q. As sketched in the left panel of figure 2.3, harmonic potential energy surfaces (PESs) with same frequency ω_v, but with different equilibrium geometries are assigned to the two basis states. The resulting vibrational relaxation energy ε_v, is defined in the left panel of figure 2.3. In this approximation, the adiabatic Hamiltonian reads

$$\hat{h}(Q) = (2z - \sqrt{2\varepsilon_v}\,\omega_v\, Q)\,\hat{\rho} - \tau\,\hat{\sigma}^x + \frac{1}{2}\omega_v\, Q^2 \tag{2.10}$$

This Hamiltonian can be diagonalized for each Q to get the Q-dependent ground and excited states. The Q-dependence of the relevant energies defines the adiabatic PES in the right panel of figure 2.3. These PES contain all the information needed for the calculation of optical spectra in a nonpolar solvent.

Although adiabatic PES are anharmonic, for not too strong anharmonicity, the absorption spectrum can be calculated in the local harmonic approx-

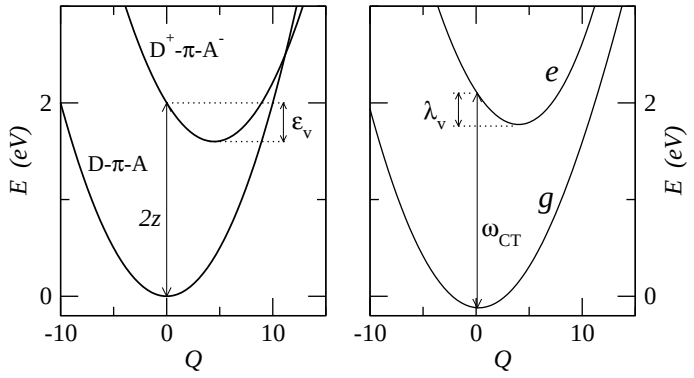

Figure 2.3: Basis states (left) and adiabatic eigenstate PESs (right) obtained from the diagonalization of Hamiltonian in equation (2.10) with $z = 1\ eV$, $\tau = 0.5\ eV$, $\omega_v = 0.2\ eV$ and $\varepsilon_v = 0.4\ eV$. In the left panel, ε_v marks the vibrational relaxation energy relevant to the basis states, while λ_v in the right panel, shows the same quantity for the adiabatic eigenstates.

imation [96, 97]. The absorption spectrum, expressed in terms of the molar absorption coefficient, is calculated as follows:

$$\varepsilon(\omega) = \frac{N_A\,\omega_{CT}\,\mu_{CT}^2}{60\log 10\ \hbar\,c^2\,\varepsilon_0}\,\frac{e^{-S}}{\sigma\sqrt{2\pi}}\,\sum_n \exp\left[-\frac{(\omega_{CT}+(n-S)\omega_v-\omega)^2}{2\sigma^2}\right] \quad (2.11)$$

$S = \lambda_v/(\hbar\omega_v)$ is the Huang-Rhys factor, where $\lambda_v = \varepsilon_v(1-2\rho)^2$ is the vibrational relaxation energy upon transition (see figure 2.3) and σ is the intrinsic linewidth of the Gaussian shape assigned to each vibronic line. N_A, $\hbar$, c and ε_0 are the Avogadro number, the reduced Planck constant, the speed of light and the vacuum dielectric permittivity, respectively. For the sake of simplicity we set the vibrational frequency of the ground and excited state to the same value ω_v. A more rigorous choice does not provide appreciable differences in the calculated spectra. [97]

The large redistribution of the electronic charge that accompanies the optical transition implies a coupling to solvation degrees of freedom. In the framework of the reaction field approximation, the solvent is described as an

elastic polarizable medium that reacts to the presence of solute molecules exerting, at the solute location, an electric field proportional to the solute dipole moment. Different timescales characterize the solvent reaction to the presence of a polar solute. The electronic polarization of solvent molecules occurs on a very fast time scale: the electronic degrees of freedom of solvent molecules react instantaneously to the CT transition and can be accounted for by a renormalization of model parameters. [92] In the simplest approximation only the solvent refractive index enters the renormalization, and in view of the marginal variation of the refractive index in common organic solvents, solvent-independent molecular parameters are safely assumed [92].

The reorientation of the polar solvent molecules around a polar solute is a slow motion that can be accounted for by introducing an effective solvation coordinate, proportional to the orientational component of the reaction field, F. This solvation coordinate couples to the electronic system in the same way as Q. The total Hamiltonian, also accounting for polar solvation, reads [92, 96]:

$$\hat{h}(Q,F) = \left(2z - \sqrt{2\varepsilon_v}\,\omega_v\, Q - \mu_0 F\right)\hat{\rho} - \tau\,\hat{\sigma}^x + \frac{1}{2}\omega_v\, Q^2 + \frac{\mu_0^2}{4\varepsilon_{or}}\,F^2 \quad (2.12)$$

where the solvation relaxation energy ε_{or}, related to the solvent dielectric constant and refractive index, is treated as an adjustable parameter [92, 96, 93]. The vibrational coordinate Q and (the orientational component of) the reaction field F enter the Hamiltonian (2.12) in a similar way, but their different dynamics suggests a different treatment. In particular, F is treated as a classical coordinate: the Hamiltonian (2.12) is diagonalized for several F values, and, for each F, relevant optical spectra are calculated according to equation (2.11). Finally, the total spectrum is obtained as the sum of spectra calculated at different F, weighted according to the Boltzmann distribution [93]. As expected on physical basis, polar solvation is responsible for the appearance of inhomogeneous broadening that smears

out the vibronic structure.

In the following this two state model is applied to reproduce the absorption spectra of Fc-PTM and of its methylated derivative Me_9Fc-PTM. Although there are not available information about the solid state behavior of Me_9Fc-PTM, the simultaneous spectroscopic analysis of both compounds will deepen our understanding and allow for a cross check of the model. Spectra calculated for Fc-PTM and Me_9Fc-PTM are reported in the middle panels of figure 2.4. The spectra have been obtained for the molecular parameters listed in table 2.1, while adjusting ε_{or} for each solvent as shown in figure 2.4. Both compounds present a largely N ground state, as confirmed by the positive solvatochromism typical of DA chromophores with a N ground state: we estimate that ρ increases from 0.068 in cyclohexane (C_6H_6) to 0.077 in dimethyl sulfoxide (DMSO) for Fc-PTM and from 0.103 in *n*-hexane (C_6H_{12}) to 0.132 in nitrobenzene ($ArNO_2$) for Me_9Fc-PTM. The evolution with the solvent polarity of the main CT band of both compounds is well reproduced. This is a non trivial result, because it is obtained by varying, for each compound, just the single parameter ε_{or}, while keeping fixed all other molecular parameters.

Adopting solvent-independent molecular parameters largely reduces the number of free parameters with respect to the standard treatment based on the Marcus-Hush of Jortner models. [98, 99, 100, 101] Despite the reduction of free parameters, the calculated spectra in the bottom panels of figure 2.4 satisfactorily compare with experimental data, confirming the validity of the model. Moreover, the global fit of optical spectra in solvents of different polarity allows for a reliable partitioning of the relaxation energy into a vibrational and a solvation contribution, a delicate issue in the standard treatment where spectra measured in different solvents are analyzed separately.

As expected on physical grounds, we notice that for both compounds

ε_{or} vanishes in the nonpolar solvent and smoothly increases with the solvent polarity. The smaller ε_{or} values estimated for the methylated compound are in line with the larger cavity required to accommodate the bulkier solute [91, 92]. The lower ionization energy of Me_9Fc-PTM is well explained by an inductive effect of the methyl groups on Fc, resulting in a stronger D character of the Me_9Fc group. Other parameters are similar in both compounds. The spectra do not show a resolved vibronic structure, hindering a precise estimate of the vibrational frequencies ω_v and of the intrinsic linewidths σ, which are set to 0.18 and 0.07 eV, respectively, for both compounds. Vibrational relaxation energy ε_v, similar in the two compounds, are relatively small if compared with the values relevant to closed-shell organic DA chromophores. [91, 92, 93, 94, 96] This can be rationalized because in closed-shell organic DA molecules the CT results in a change of the bond order alternation, that has no counterpart in our open-shell systems like Fc-PTM and Me_9Fc-PTM. The parameter μ_0 simply fixes the absolute scale of calculated absorption spectra, while it is irrelevant for band shapes and frequencies. The μ_0 values in table 2.1 are set to reproduce the experimental extinction coefficients and correspond to dipole lengths of 1.56 and 1.77 Å for Fc-PTM and Me_9Fc-PTM, respectively. These values are unreasonably small if compared with geometrical DA distances (the distance from the Fe atom and the central C atom of PTM is 9.5 and 9.7 Å for Fc-PTM and Me_9Fc-PTM, from crystallographic data). It is a very well known that the spectroscopic estimate of μ_0, based on the two-state model, leads in general to too small values, if compared with molecular length. [101, 93, 94, 96, 102, 103, 104, 105, 106] We will face this issue in section 2.4.2.

2.3.2 Bistability in crystals of DA molecules

In the solid state, intermolecular interactions (second term in equation (2.1)) can profoundly alter molecular properties. If the molecular units are modeled

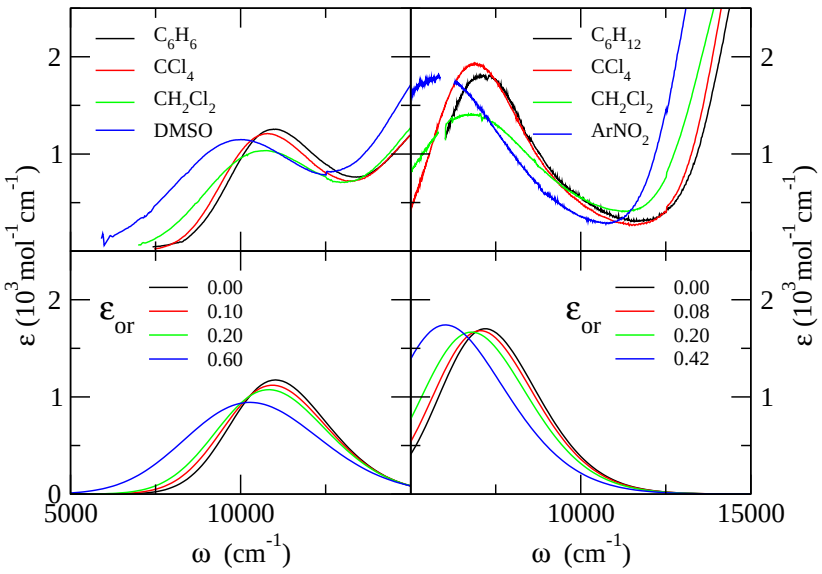

Figure 2.4: Experimental (top panels, from ref. [78]) and calculated (bottom panels) spectra with the two-state model for Fc-PTM (left column) and Me_9Fc-PTM (right column). Calculated spectra are obtained with molecular parameters in table 2.1 and the ε_{or} values in the legend. The intrinsic bandwidth is set to $\sigma = 0.07\ eV$ in all calculated spectra.

parameter	Fc-PTM	Fc_9-PTM
$z\ (eV)$	0.61	0.36
$\tau\ (eV)$	0.35	0.30
$\mu_0\ (D)$	7.5	8.5
$\varepsilon_v\ (eV)$	0.10	0.12
$\omega_v\ (eV)$	0.18	0.18

Table 2.1: Molecular parameters for Fc-PTM and Me_9Fc-PTM described in the two-state model.

by the two-state electronic Hamiltonian (2.2), the charge distribution on each molecule is fully described by the operator $\hat{\rho}$, and the electrostatic intermolecular interaction term in in equation (2.1) can be written as

$$\hat{V}_{ij} = V_{ij}\ \hat{\rho}_i \hat{\rho}_j \tag{2.13}$$

where V_{ij} is the interaction energy between the i-th and j-th molecules both in the D$^+$-π-A$^-$ state [20, 82, 83]. The crystal Hamiltonian obtained from the general Hamiltonian (2.1), with the molecular two state model in equation (2.2) and the interaction term expressed by (2.13) is equivalent to a $S = 1/2$ Heisenberg model with longitudinal and transverse magnetic field. The longitudinal field correspond to the molecular ionization energy, the transverse field to the hybridization energy. Formally the interaction between spins corresponds to the intermolecular electrostatic interactions.

For the sake of clarity, we start considering only the electronic Hamiltonian, while molecular vibrations, that in Fc-PTM play only a marginal role because of the small value of ε_v, will be introduced later. To start with, we first consider the $\tau = 0$ limit. For $\tau = 0$, each molecule can be either in the D-π-A or in the D$^+$-π-A$^-$ state. The energy required to switch the N molecules of the crystal from the D-π-A to the D$^+$-π-A$^-$ is $2N(z + M)$, where M is the (half) Madelung energy of a crystal of zwitterions, defined as:

$$M = \frac{1}{2N} \sum_{i,j} V_{ij} \tag{2.14}$$

When $z + M < 0$ the ground state of the crystal corresponds to a collection of D-π-A molecules, but for $z + M > 0$ it describes a collection of D$^+$-π-A$^-$ molecules. An abrupt N-I crossover is located at $z + M = 0$.

Moving away from the $\tau = 0$ limit opens the way to states with intermediate ionicity, but inevitably leads to a more complex problem. The Hamiltonian (2.1) with electrostatic interactions expressed in equation (2.13)

can be diagonalized exactly on clusters of N molecules, [20, 82] but, since the basis dimension increases as 2^N, it is impossible to obtain exact results on large enough three dimensional clusters as required to understand the role of long-range electrostatic interactions. We therefore adopt the mean field (mf) approximation, a good and powerful approximation to describe the ground-state properties of clusters of interaction DA molecules [20, 82]. In the mf approximation, the Hamiltonian of interacting molecules reduces to the sum of effective molecular Hamiltonians, as follows:

$$H_{mf} = \sum_i [2\,(z + M\rho)\;\hat{\rho}_i \;-\; \tau\,\hat{\sigma}_i^x\;] - NM\rho^2 \tag{2.15}$$

where the effective molecular Hamiltonian is simply obtained from equation (2.2) with a renormalization of the ionization energy: $z_{eff} = z + M\rho$. In other terms, the energy required to ionize a DA molecule is $2z$ for isolated molecules (more precisely for molecules in a nonpolar environment) but in the crystal this energy becomes $2z_{eff}$, and depends on the charge distribution of surrounding molecules ρ. The self consistent nature of the mf Hamiltonian, with the effective ionization energy depending on the average molecular ionicity, is able to capture the cooperative nature of intermolecular interactions. Attractive interactions ($M < 0$) decrease the effective ionization energy, favoring I lattices.

The solution of the mf Hamiltonian (2.15) is found by iteration: an initial guess of ρ enters the definition of the mf Hamiltonian, which is diagonalized to get an updated ρ estimate to be inserted again into the mf Hamiltonian. Convergence is reached upon a few iterations. The resulting $\rho(M)$ curves, calculated for a crystal of molecules with $z = 0.61\ eV$ (as relevant for Fc-PTM) and two different values of τ, are reported in figure 2.5. Only attractive interactions ($M < 0$) are considered. For $\tau = 1\ eV$ (black continuous line) ρ increases smoothly from 0.25 in the limit of non-interacting molecules ($M = 0$), to $\rho \sim 1$ for $M \lesssim -2\ eV$. Attractive interactions push

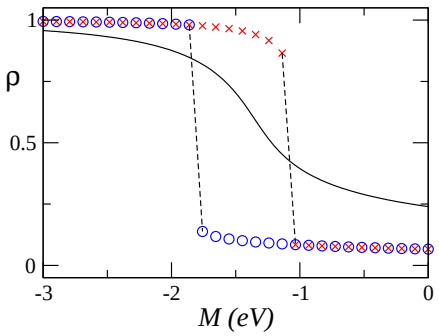

Figure 2.5: M-dependence of ρ for a crystal of DA molecules described by the mf Hamiltonian (2.15). The black continuous line refers to $z = 0.61\ eV$ and $\tau = 1\ eV$. Symbols refer to $z = 0.61\ eV$ and $\tau = 0.35\ eV$. Blue circles are obtained setting the initial guess for the self-consistent solution of the mf Hamiltonian as $\rho \approx 0$, red crosses are obtained with the choice $\rho \approx 1$. The dashed lines are drawn as guide to the eyes.

the system towards I states and the conventional N-I crossover ($\rho = 0.5$) occurs at $M = -2z$. More interesting is the case of smaller $\tau = 0.35\ eV$. In fact, in this case, two stable solutions are found in proximity of the interface, depending on the initial guess for ρ. Specifically, the blue circles in figure 2.5 show results obtained fixing the initial guess as $\rho \approx 0$, while red crosses are obtained setting the guess $\rho \approx 1$. The region, $-1.8 < M < -1.1$, where the two results do not coincide defines the bistability region where a N and an I solution coexist for the same model parameters.

The appearance of bistability also implies the presence of a region of forbidden ρ values for the system ($0.14 < \rho < 0.86$). More specifically, the N-I crossover becomes discontinuous with a sharp ionicity jump from a N to an I state and a wide hysteresis loop. In particular, for isolated molecules ($M = 0$) the unique stable solution has $\rho \approx 0.1$. Increasing attractive interactions barely affects ρ up to $M = -1.75\ eV$ where ρ abruptly jumps

to $\rho \approx 1$. Similarly, starting from the I lattice ($\rho \approx 1$) relevant to the case of large attractive interactions ($M = -3\ eV$), decreasing M has minor effects on ρ up to $M = -1\ eV$ where the ionicity jumps from 0.86 to 0.1. It is worth noting that the hysteresis cycle presented in figure 2.5 is obtained considering the mf Hamiltonian (2.15) in the zero temperature limit, but the result is practically unaffected by temperature. In fact, for Fc-PTM parameters the energy gap between the ground and the excited state (corresponding to the transition frequency in equation (2.6)) is always much larger than the thermal energy and the ground state ionicity ρ barely differs from its thermal averaged value up to 2000 K.

We now introduce the coupling between electronic and vibrational degrees of freedom. As discussed in the previous section, we account for a vibrational coordinate Q on each molecule (see equation (2.10)). A single vibrational coordinate q, corresponding to the in-phase vibration of all the molecules of the crystal is introduced here. To simplify notation the new vibrational coordinate is defined in energy units as follows:

$$q = \sqrt{\frac{2\varepsilon_v}{N}}\,\omega_v \sum_i Q_i \tag{2.16}$$

With this definition, the adiabatic mf Hamiltonian becomes

$$H_{mf}(q) = \sum_i \left[2\left(z + M\rho - \frac{q}{2}\right)\,\hat{\rho}_i \;-\; \tau\,\hat{\sigma}_i^x \right] - NM\rho^2 + \; N\frac{q^2}{4\varepsilon_v} \tag{2.17}$$

The mf Hamiltonian again coincides with the two-state Hamiltonian in equation (2.2) but with a ρ and q-dependent $z_{eff} = z + M\rho - q/2$. By substituting q with its equilibrium value $q_{eq} = 2\varepsilon_v\rho$ (obtained by applying the Hellmann-Feynman theorem) we get a simple expression for the effective ionization energy, $z_{eff} = z + (M - \varepsilon_v)\rho$, accounting for both electrostatic intermolecular interactions and molecular vibrations. The coupling between electronic and vibrational degrees of freedom plays the same role as attractive electrostatic intermolecular interactions [33]. The $\rho(M)$ curves in figure 2.5, then

also apply in the presence of vibrational coupling, but with M replaced by $M - \varepsilon_v$. For Fc-PTM $\varepsilon_v = 0.1\ eV$ and the vibrational contribution to M represents just a minor correction.

More interesting is the calculation of the q-dependent ground state energy, obtained by the diagonalization of the q-dependent mf Hamiltonian in equation (2.17). Panels **a-d** of figure 2.6 show the ground state potential energy surfaces (PES) calculated for a system with $z = 0.61\ eV$, $\tau = 0.35\ eV$, $\varepsilon_v = 0.1\ eV$, as relevant for Fc-PTM, and different M values. For relatively weak interactions ($M - \varepsilon_v = -0.9\ eV$, corresponding to a large and negative z_{eff}), the $\rho(z)$ curve in figure 2.5 leads to a single solution corresponding to a N ground state with $\rho(z) \approx 0.1$. The corresponding PES (panel **a** of figure 2.6) is almost harmonic with a minimum located at $q_{eq} = 0.01\ eV$. Similarly, for strong interactions ($M - \varepsilon_v = -2.0\ eV$, corresponding to a large and negative z_{eff}) a single solution is found, corresponding to an I state with $\rho(z) \approx 1$. The relevant PES (panel **d** of figure 2.6) is centered at $q_{eq} = 0.2\ eV$. For $M - \varepsilon_v$ within the bistability region two stable states, with different ρ, are found. For $M - \varepsilon_v = -1.2\ eV$, a N ($\rho = 0.09$) and an I state ($\rho = 0.9$) are both stable. The corresponding PES in panel **b** of figure 2.6 are almost harmonic with minima located at $q_{eq} = 0.018$ and $0.18\ eV$. Of course just one of the two states, the lowest energy one, is thermodynamically stable, while the other state is metastable. For $M - \varepsilon_v = -1.3\ eV$ (cf. panel **c**, figure 2.6), again in the bistability region, the situation is reversed with the stable state corresponding to an I state ($\rho = 0.93$), while the metastable state corresponds in this case to a N state ($\rho = 0.1$).

The ground state properties of mf Hamiltonian in equation (2.15) (or equivalently of Hamiltonian (2.17), by substituting in the following discussion $M \to M - \varepsilon_v$) are finally summarized in its zero temperature phase diagram in in figure 2.7. Bistability is expected for crystals of largely N (closed or open shell) molecules with strong attractive electrostatic intermolecular

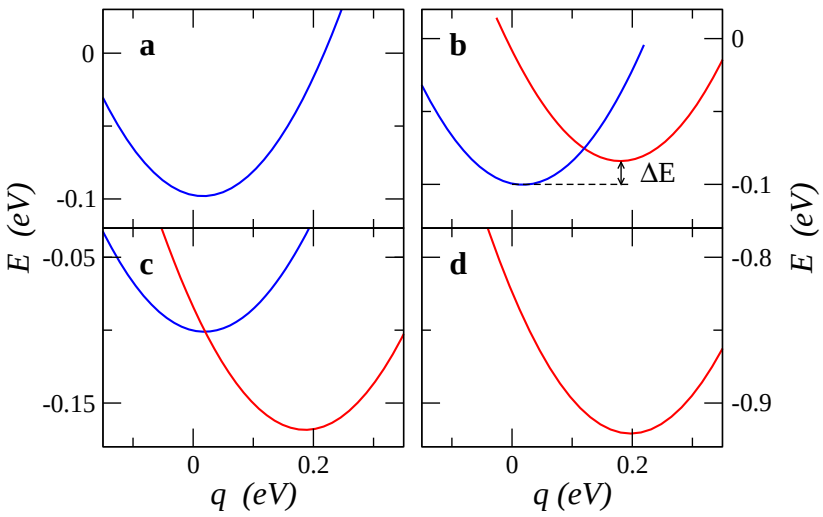

Figure 2.6: Ground state PESs obtained from the diagonalization of mf Hamiltonian in equation (2.17), calculated for Fc-PTM molecular parameters in table 2.1, and $M = -0.8$, -1.1, -1.2 and $2.0\ eV$, in panels from **a** to **d** respectively.

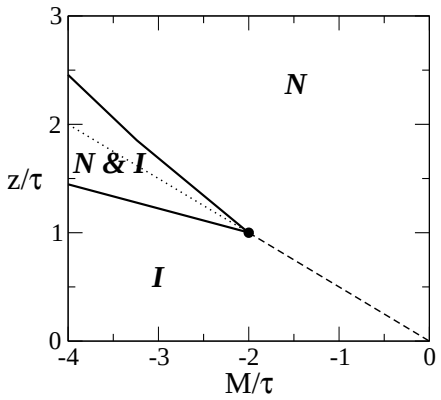

Figure 2.7: Zero temperature phase diagram of mf Hamiltonian (2.15). Monostable phases (N and I) and bistability region (N&I) are indicated. The black dot marks the quantum critical point. The $z = -M/2$ line below the critical point (dashed line) marks states with $\rho = 0.5$ and above the critical point (dotted line) indicates the degeneracy of N and I stable phases.

interactions; for this reason the phase diagram in figure 2.7 is drawn only for positive z and negative M. For large molecular ionization energies (i.e. large z) and weak intermolecular electrostatic interactions (small $|M|$) the crystal is composed by N molecules (region marked as N in the figure), while, for large $|M|$ and small z values the molecules become I (region marked by I in the figure). Below the (quantum) critical point ($z/\tau < 1$), marked with a black dot in the figure, the N-I crossover is continuous: ρ varies with continuity around the crossover value $\rho = 0.5$ (cf. the black continuous curve in figure 2.5). The dashed line $z = -M/2$ in the figure marks the conventional N-I crossover $\rho = 0.5$, separating systems with a N ground state ($\rho < 0.5$, $z > -M/2$) from those with an I ground state ($\rho > 0.5$, $z < -M/2$). For $z/\tau > 1$, states with intermediate ionicity ($\rho \sim 0.5$) become unstable and the N-I crossover becomes discontinuous with the appearance of a bistability region (N&I region within continuous lines in figure 2.7). In this region,

two (meta)stable states are accessible to the crystal: a N and an I ground state are both possible, in general with different energies. In particular, in the bistability region located above the dotted line $z = -M/2$, the lowest energy state, corresponding to the thermodynamically stable phase, is N ($\rho < 0.5$), while the I state is metastable. The opposite situation occurs in the bistability region below the dotted line. The two stable states are exactly degenerate along the dotted line and they coalesce towards the same state with $\rho = 0.5$ at the critical point. The continuous/discontinuous character of the N-I crossover, and therefore the possibility to observe bistability, is governed by the hybridization energy τ. In the proximity of the N-I crossover, i.e. for $z \approx -M/2$, for large hybridization energy, i.e. $\tau > z$, the system prefers to delocalize the electron within each molecular unit leading to states of intermediate ionicity. On the opposite, if the hybridization energy is small ($\tau < z$) mixed-valence states are unstable and the system is forced to choose either one of the two (meta)stable states. [20]

2.3.3 The bistability of Fc-PTM

Results presented in the previous section demonstrate that a discontinuous N-I crossover can be induced in crystals of DA chromophores by electrostatic intermolecular interactions, and that, for the molecular parameters relevant to Fc-PTM, the bistability region can be fairly large. In fact, in the spirit of the bottom up approach, [86, 87, 83] all molecular parameters entering the mf Hamiltonian in equation (2.17) are obtained from the analysis of solution spectra of Fc-PTM, in the reasonable hypothesis that the two-state model that describes Fc-PTM in solution also applies to the same molecule in the crystal.

To support our hypothesis of electrostatically induced bistability in Fc-PTM crystals we need a reliable estimate of M, defined in equation (2.14) as the half Madelung energy of a lattice of fully I D^+-π-A^-molecules. In

the crudest approximation [20, 82, 83], M can be estimated modeling the charge distribution on the zwitterionic Fc-PTM in terms of a positive and a negative electron charge located at the center of the D and A groups, respectively. In this approximation, locating the charges at the positions of the Fe atom and of the central C-atom of the PTM, we estimate $M = -0.72\ eV$, an encouraging result. However this approximation is too rough for large molecules as Fc-PTM. An improved estimate of M can be obtained modeling the charge distribution on each molecule as a collection of point atomic charges as obtained by quantum chemical calculations [107]. The calculation is not trivial, however, because we need electrostatic interactions among Fc-PTM molecules in the D^+-π-A^- form, and not in the almost N ground state that results from gas-phase calculations.

To overcome this subtle problem we perform calculations on a molecule subject to an external static electric field as to force the charge transfer from the D to the A unit. Figure 2.8 summarizes the results of restricted Hartree-Fock PM6 calculations (MOPAC2007 package [108]) on an isolated Fc-PTM molecule in the experimental crystallographic geometry [79]. A static electric field F is directed along the x-axis that connects the central C-atom of the PTM to the Fe-atom of the Fc. The top panel shows the F-dependence of μ_x, the x-component of the molecular dipole moment, defined as $\mu_x = e\sum_p q_p x_p$, where e is the electronic charge, x_p is the x-coordinate of the p-th atom, and q_p is the Coulson net atomic charge [108]. The S-shaped $\mu_x(F)$ curve in figure 2.8 clearly points to two different regimes: a low and a high field regime separated by a region at $F \approx 0.4\ V/\text{Å}$ where charges rearrange dramatically. In the central panel of figure 2.8 the dielectric polarizability, $\alpha \propto \partial\mu_x/\partial F$, shows a large peak at the interface that separates two regions of almost constant polarizability, whose boundaries are marked by dotted and dash-dotted vertical lines. These two regions correspond to two different regimes for Fc-PTM: an almost N regime with the ground state largely

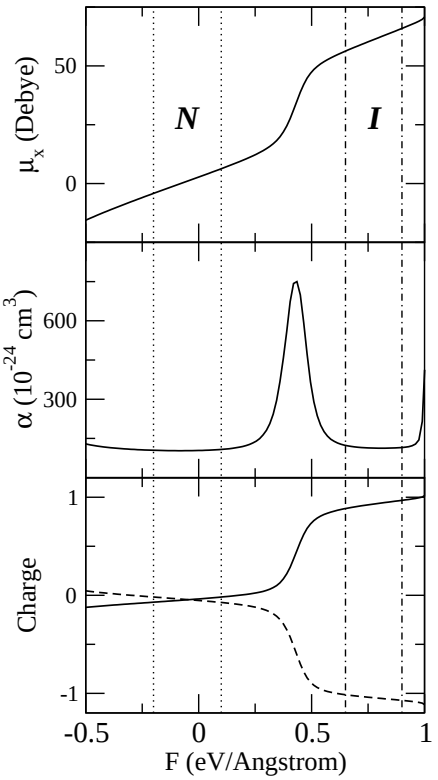

Figure 2.8: Results of PM6 calculations for Fc-PTM under an external static electric field, F. F-dependence of the molecular dipole moment μ_x (top panel), molecular polarizability α (central panel), and total net charges (bottom panel) on the Fc (continuous line) and PTM (dashed line) units. Regions within dotted and dash-dotted vertical lines approximately mark the N and the I regimes, corresponding to flat regions of α.

dominated by the D-π-A state and an I regime, dominated by the D^+-π-A^- state. To further support this interpretation, the bottom panel of figure 2.8 shows the total charges on the Fc (continuous line) and PTM (dotted line) units. The sum of the charges on the two units is approximately zero, confirming the picture of a charge transfer from D to A with an electrically neutral π-bridge. Moreover, in the small F regime the charge transferred from D to A is approximately zero, while the region of the second plateau corresponds to a system where approximately one electron is transferred. A reasonable estimate of the charge distribution of the Fc-PTM D^+-π-A^- state is therefore given by the Coulson net point atomic charges, obtained with PM6 calculations on the Fc-PTM molecule in an electric field $0.65 < F < 0.9$ $V/$Å, corresponding to region delimited by dash-dotted lines in figure 2.8.

We can now estimate M on the basis of the molecular charge distribution obtained for Fc-PTM in the I regime of figure 2.8. To ensure at least two significant digits in the estimate of M, we sum all interactions among ∼19000 molecular sites ($17 \times 17 \times 33$ unit cells). For F values corresponding to the I regime (region within dash-dotted lines in figure 2.8) we estimate M ranging between -1.0 eV (for $F = 0.65$ $V/$Å) to -1.5 eV (for $F = 0.9$ $V/$Å). This result safely locates Fc-PTM crystals in the bistability region of figure 2.5. For comparison, in the N regime (region within dotted lines in figure 2.8) $|M| < 0.05$ eV, i.e. confirming that electrostatic interactions between fully N molecules are negligible.

The specific bottom up model built for Fc-PTM crystal explains the temperature dependence of Mössbauer spectra reported in figure 2.9 (from ref. [79]). In the 4.2 K spectrum only the doublet assigned to the Fc appears, indicating that the neutral D-π-A form of Fc-PTM largely dominates at low temperature. With increasing temperature, an additional doublet appears in Mössbauer spectra, characteristic of the ferrocinium ion (Fc^+), signaling

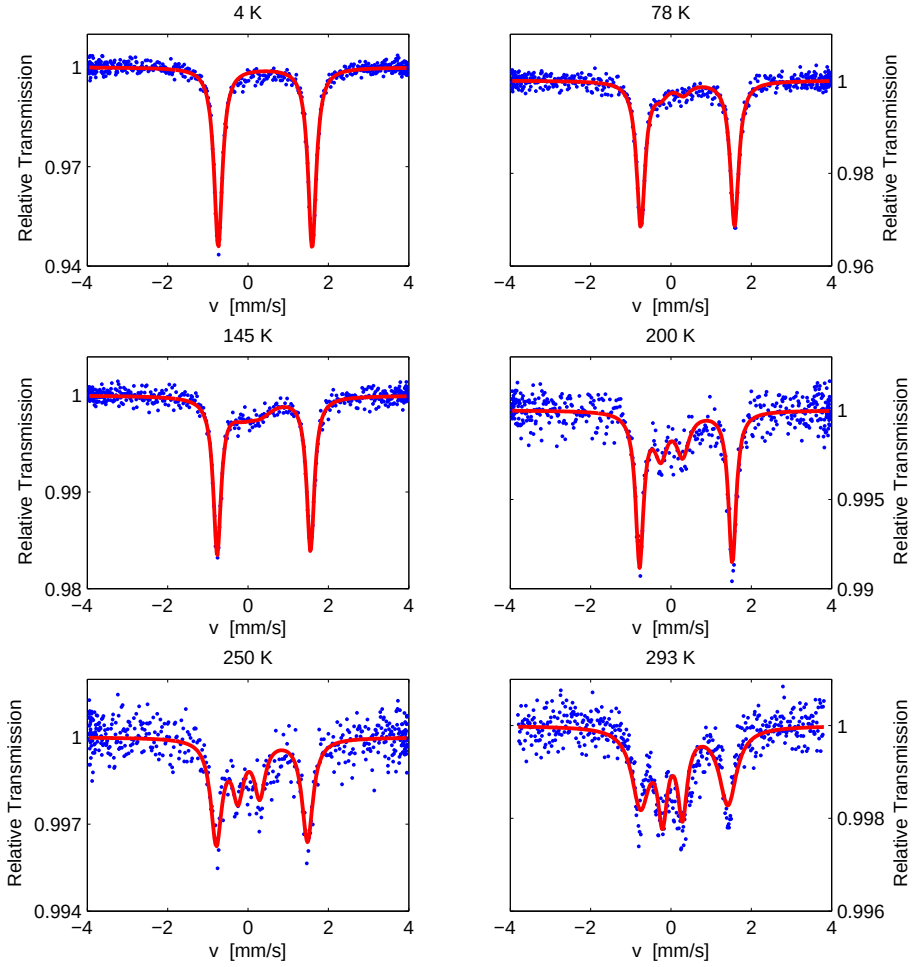

Figure 2.9: Temperature dependence of Mössbauer spectra of Fc-PTM. Dots are experimental data from ref. [79]. Red lines are fittings of experimental data based on the proposed model for bistability and fitting parameters in table 2.2.

the presence of the D^+-π-A^- form of Fc-PTM. The intensity of the Fc^+ doublet increases with temperature at the expense of the intensity of the Fc signal, suggesting an increasing population of the D^+-π-A^- form. At 293 K the relative intensity of the two signals is comparable, pointing to similar populations of the two species. This behavior can be rationalized in term of the thermal population on an I metastable state, as described by the mf treatment of electrostatic interactions. In fact Mössbauer spectra in figure 2.9 can be satisfactorily reproduced in term of the Boltzmann population of an I metastable state separated from a N stable state by a temperature independent energy gap $\Delta E = 14\ meV \approx 160\ K$. This energy gap is obtained with the mf Hamiltonian in equation (2.17), adopting Fc-PTM molecular parameters obtained from solution spectra and $M = -1.1\ eV$, consistent with the estimate from PM6 calculation (see panel **b** of figure 2.6). Experimental Mössbauer spectra in figure 2.9 are fitted as a Boltzmann-weighted sum of two couples of Lorentzian bands (for Fc and Fc^+ doublets) with adjustable positions and widths reported in table 2.2. In view of the many approximations involved in the model, the overall quality of the fit (red lines in figure 2.9) is good, as it can be appreciated from the agreement with experimental data (blue dots) in figure 2.9.

$T(K)$	v_1^{II}	v_2^{II}	γ^{II}	v_1^{III}	v_2^{III}	γ^{III}
4.2	-0.76	1.58	0.12	-0.24	0.24	0.12
78	-0.76	1.58	0.12	-0.24	0.24	0.12
145	-0.80	1.55	0.10	-0.24	0.24	0.16
200	-0.80	1.50	0.11	-0.22	0.28	0.14
250	-0.80	1.44	0.14	-0.22	0.28	0.12
293	-0.80	1.40	0.17	-0.22	0.28	0.11

Table 2.2: Parameters of the T-dependent Mössbauer spectra fit (red lines in figure 2.9) expressed in mms^{-1}. Spectra shapes are obtained as the sum of 4 Lorentzian peaks: v_1^{II} and v_2^{II} represent the peaks positions of the Fc doublet and γ^{II} theirs half width at half maximum. Same notation is adopted for Fc^+. Fc and Fc^+ doublets are weighted by relative thermal populations, obtained with a T-independent energy gap $\Delta E = 14\ meV$.

2.4 Bottom up with a three-state model

2.4.1 Three state model for Fc-PTM and Me_9Fc-PTM

A deeper analysis of Me_9Fc-PTM optical absorption spectra, reported in the right upper panel of figure 2.11, reveals the presence of a shoulder around 15000 cm^{-1}, that is safely assigned to a secondary CT absorption implying a π-bridge to A transition [78]. This assignment is supported by the absence of any absorption feature in this spectral range in either the methylated Fc unit or in the PTM unit and is further corroborated by the weak solvatochromism of this band [78]. Similar features are observed for Fc-PTM around 15000-17000 cm^{-1} (see left upper panel of figure 2.11), but in this case, the overlap with the localized absorption of the Fc unit makes the analysis delicate.

To account for the secondary CT bands involving the π-bridge, at least the three resonating structures D-π-A $\leftrightarrow$ D-π^+-A^- $\leftrightarrow$ D^+-π-A^-, must be accounted for, where the first and the latter structures (corresponding to the fully N and fully I structures of the previous section) largely dominate over the third, higher energy (virtual) state. The CT occurs through the bridge, so on the basis of the three states, D-π-A, D-π^+-A^- and D^+-π-A^-, the electronic Hamiltonian reads

$$\hat{h}_{el}^{(3)} = 2\tilde{z}\ \hat{\rho}^D + 2\tilde{x}\ \hat{\rho}^\pi - \tilde{\tau}\ \hat{\sigma}^{(3)} \tag{2.18}$$

where the operators

$$\hat{\rho}^D = \begin{pmatrix} 0 & 0 & 0 \\ 0 & 0 & 0 \\ 0 & 0 & 1 \end{pmatrix} \quad \text{and} \quad \hat{\rho}^\pi = \begin{pmatrix} 0 & 0 & 0 \\ 0 & 1 & 0 \\ 0 & 0 & 0 \end{pmatrix} \tag{2.19}$$

measures the charge transferred from the D and from the π-bridge to the A

respectively, and

$$\hat{\sigma}^{(3)} = \begin{pmatrix} 0 & 1 & 0 \\ 1 & 0 & 1 \\ 0 & 1 & 0 \end{pmatrix} \tag{2.20}$$

accounts for the mixing between the D-π-A and the D^+-π-A^-states, mediated by the bridge state; $2\tilde{x}$ and $2\tilde{z}$ measure the energy of the states D-π^+-A^- and D^+-π-A^- respectively, having set to zero the energy of the D-π-A state (the tilde identifies the three-state model parameters with respect to the two-state model parameters in the previous section). As discussed above, the CT state involving the bridge is higher in energy that the main CT state, i.e. $\tilde{x} > \tilde{z}$.

A detailed parametrization of the three-state model is difficult, particularly because of the large overlap of the second absorption band with higher energy absorptions in both compounds. In the absence of additional data, as fluorescence or absorption from the first excited state, in order to avoid the proliferation of free parameters, the same matrix element $\tilde{\tau}$ describes the electron hopping from the bridge to the acceptor and from the donor to the bridge. With the same spirit, the dipole moment of the D-π^+-A^- state is set to the reasonable value $\tilde{\mu}_0/2$, where $\tilde{\mu}_0$ is the dipole moment of the D^+-π-A^-state. This choice locates the centroid of positive charge of the bridge state just halfway between the D and A centers.

As in the two-state model, the coupling to an effective molecular vibration is introduced assigning harmonic PESs with same frequency but different equilibrium geometries to the basis states, as shown in the left panels of figure 2.10. In principle, different geometries are expected for each of the three basis states leading to two independent vibrational relaxation energies for D-π^+-A^- and D^+-π-A^- states. However, getting reliable information on the vibrational coupling of the third state is difficult, and we impose the same geometry on the two charge-separated states (see figure 2.10, left panel), so

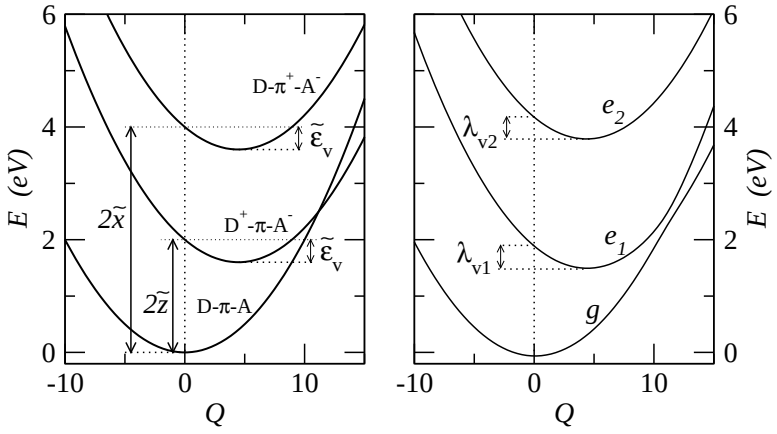

Figure 2.10: Basis states (left panels) and eigenstate (right panel) PES for the three-state model in equation (2.21) with $\tilde{z}$= 1 eV, $\tilde{x}$= 2 eV, $\tilde{\tau}$= 0.5 eV $\tilde{\omega}_v$= 0.2 eV, $\tilde{\varepsilon}_v$= 0.4 eV and $\tilde{\varepsilon}_{or}$= 0 eV.

that the same relaxation energy, $\tilde{\varepsilon}_v$, applies to both states. Different choices are of course possible but do not alter the main results.

Polar solvation is treated again in the framework of the reaction field model, with the reaction field proportional to the molecular dipole moment. Since the dipole moment of the third state is set to a fixed fraction of $\tilde{\mu}_0$, polar solvation is described by the single parameter $\tilde{\varepsilon}_{or}$. The total Hamiltonian, accounting for both vibrational coupling and polar solvation, then reads

$$\begin{aligned}\hat{h}^{(3)}(q,F) = &\left(2\tilde{z} - \sqrt{2\tilde{\varepsilon}_v}\,\omega_v\; Q - \tilde{\mu}_0 F\right)\hat{\rho}^D \\ &+ \left(2\tilde{x} - \sqrt{2\tilde{\varepsilon}_v}\,\omega_v\; Q - \frac{\tilde{\mu}_0}{2}F\right)\hat{\rho}^\pi \\ &- \tilde{\tau}\;\hat{\sigma}^{(3)} + \frac{1}{2}\tilde{\omega}_v\, Q^2 + \frac{\tilde{\mu}_0^2}{4\tilde{\varepsilon}_{or}}F^2\end{aligned} \tag{2.21}$$

where again the tilde marks symbols relevant to the three-state model. For each F, the diagonalization of the Q-dependent Hamiltonian leads to three Q-dependent eigenstates, that describe the PES relevant to the ground state,

parameter	Fc-PTM	Fc_9-PTM
$\tilde{z}$ (eV)	0.78	0.50
$\tilde{x}$ (eV)	0.87	0.69
$\tilde{\tau}$ (eV)	0.47	0.47
$\tilde{\mu}_0$ (D)	15.0	15.5
$\tilde{\varepsilon}_v$ (eV)	0.06	0.07
$\tilde{\omega}_v$ (eV)	0.18	0.18

Table 2.3: Molecular parameters for Fc-PTM and Me_9Fc-PTM described in the three-state model.

g, and to the first and second excited states, e_1 and e_2, respectively. Right panel of figure 2.10 shows the PES obtained for the specific set of parameters reported in the figure caption. Absorption spectra are calculated extending the summation in equation (2.11) to the n and n' vibrational states of the first and second excited states, accounting for the relevant Huang-Rhys factors, $S_i = \lambda_{vi}/(\hbar\tilde{\omega}_v)$, with λ_{vi} defined in the left panel of figure 2.10 and $i = 1, 2$. The calculation is repeated for different F, and the calculated spectra, Boltzmann-weighted on the total ground-state energy, are summed up to give the absorption spectrum.

The spectra calculated within the three-state model are reported in bottom panels of figure 2.11. Spectra are calculated for the molecular parameters in table 2.3 and the $\tilde{\varepsilon}_{or}$ values in the legends. The vibrational frequencies and the intrinsic line width are set to the same values as in the two-state model. To facilitate the comparison, experimental spectra are reported in the upper panels of the same figure. As expected, the three-state model results in two absorption bands, which reproduce the experimental observation of two solvatochromic CT absorption bands. A detailed comparison of calculated and experimental spectra is hindered, particularly for Fc-PTM,

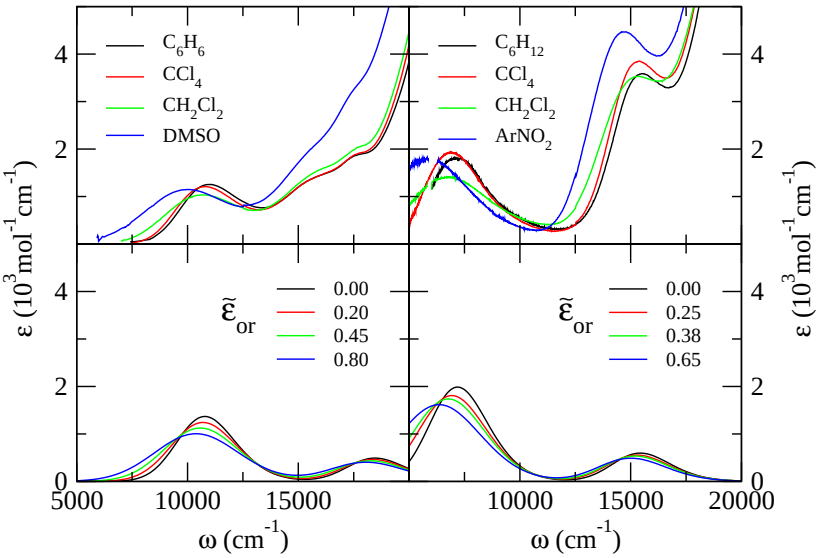

Figure 2.11: Experimental (top panels, from ref. [78]) and calculated (bottom panels) spectra with the three-state model for Fc-PTM (left column) and Me_9Fc-PTM (right column). Calculated spectra are obtained with molecular parameters in table 2.3 and the $\tilde{\varepsilon}_{or}$ values in the legend. The intrinsic bandwidth is set to $\sigma = 0.07\ eV$ in all calculated spectra.

by the overlap of the secondary CT band with nearby localized absorption bands. It is certain possible to improve the quality of calculated spectra by increasing the number of parameters, however the basic role of the bridge state is captured already in the simplest model.

From table 2.3, it turns out that $\tilde{x} > \tilde{z}$ for both compounds, as required on physical basis. Moreover $\tilde{\tau}$, which measures the direct charge hopping from either the D or the A site to the bridge, is larger than the bridge-mediated hopping, τ, in the two-state model (cf. table 2.1). The effective strength of the vibrational coupling is roughly halved in the three-state model, suggesting that the effective ε_v estimated in the two-state model is roughly the sum of the contributions from the two excited states. The values of the solvent relaxation energy in the three-state, reported in the legend of figure 2.11 model are instead larger than the corresponding two-state model results (cf. figure 2.4). This increase compensates for the reduction of the mesomeric dipole moment in the three-state model. The sizable weight of the D-π^+-A^- in the first excited state in fact leads to a decrease of the relevant dipole moment with respect to the two-state model, so that larger solvent relaxation energies are required in the three-state model to reproduce the same solvatochromism. While microscopic models relate the solvation relaxation energy to the solvent dielectric constant and refractive index and to the size and shape of the cavity occupied by the solute [109, 94], this analysis demonstrates that ε_{or} is best treated as an adjustable parameter, whose specific value also depends on the model adopted to describe the solute electronic structure.

More important to understand the role of the π-bridge in the intramolecular CT is the observation that the effective dipole length extracted in the three-state model, $\tilde{\mu}_0$ in table 2.3, is about twice the corresponding estimate in the two-state model (c.f. table 2.1) and corresponds to a DA distance of 3.1 and 3.3 Å for Fc-PTM and Me_9Fc-PTM, respectively. These values are still

small compared with the geometrical DA distance (9.5 and 9.7 Å for Fc-PTM and Me_9Fc-PTM), but they considerably improve over the corresponding estimates obtained in the two state approach, leading to a ratio between the geometrical and spectroscopic estimate of the DA distance in line with similar results for other DA molecules. [101, 93, 94, 96, 102, 103, 104, 105, 106]

2.4.2 Dipole length: the role of the bridge

The three-state model described above does not add much to our understanding of the main (low-energy) CT absorption band whose basic features are already well captured by the two-state model. However, the three-state model leads to a more reasonable estimate of the dipole length compared with the unphysically small values obtained for both Fc-PTM and Me_9Fc-PTM within the two-state approximation. This result suggests that the well-documented discrepancy between geometrical DA distance and its spectroscopic estimate within the two-state model, results from the presence of low-lying π-bridge states. To generalize this result and to set it on a firmer basis, we discuss here an electronic model for a D-π-A dye where several bridge states are accounted for.

The model, recently introduced in the literature [110], describes the electron transfer from D to A as the result of several successive hops through the bridge sites. The bridge states are virtual states, since they present higher energy than the relevant CT state. We limit attention to the purely electronic model. Specifically, we consider a N-site molecule, where the electron is transferred from D to A via $N-1$ hops involving only adjacent sites. The resulting N states are schematically shown in figure 2.12 for $N = 5$. The same energy $\tilde{x}$ is assigned to all bridge states, while the D^+-π-A^- state has energy $\tilde{z} < \tilde{x}$. The same hopping integral $\tilde{\tau}$ describes the CT between all adjacent sites along the chain. The relevant Hamiltonian is a trivial extension

Basis states	*Energy*	*Dipole*
D - b_1 - b_2 - b_3 - A	0	0
D - b_1 - b_2 - b_3^+ - A^-	$2\tilde{x}$	$1/4\ \tilde{\mu}_0$
D - b_1 - b_2^+ - b_3 - A^-	$2\tilde{x}$	$1/2\ \tilde{\mu}_0$
D - b_1^+ - b_2 - b_3 - A^-	$2\tilde{x}$	$3/4\ \tilde{\mu}_0$
D^+ - b_1 - b_2 - b_3 - A^-	$2\tilde{z}$	$\tilde{\mu}_0$

Figure 2.12: Schematic representation of the basis state for a 5-state molecule with corresponding energies and dipole moments.

of the three-state electronic Hamiltonian in equation (2.18):

$$\hat{h}_N = \begin{pmatrix} 0 & -\tilde{\tau} & 0 & 0 & \cdots & 0 & 0 \\ -\tilde{\tau} & 2\tilde{x} & -\tilde{\tau} & 0 & \cdots & 0 & 0 \\ 0 & -\tilde{\tau} & 2\tilde{x} & -\tilde{\tau} & \ddots & 0 & 0 \\ 0 & 0 & -\tilde{\tau} & 2\tilde{x} & \ddots & \vdots & \vdots \\ \vdots & \vdots & \vdots & \ddots & \ddots & -\tilde{\tau} & 0 \\ 0 & 0 & 0 & \cdots & -\tilde{\tau} & 2\tilde{x} & -\tilde{\tau} \\ 0 & 0 & 0 & \cdots & 0 & -\tilde{\tau} & 2\tilde{z} \end{pmatrix} \tag{2.22}$$

Consistent with the three-state model described in the previous section, the dipole moment of the D^+-π-A^-state is set to $\tilde{\mu}_0$, while the dipole moments of bridge states are fractions of $\tilde{\mu}_0$, as relevant to a system with equally spaced sites (see figure 2.12), leading, for the general case in equation (2.22), to the following values: 0, $\tilde{\mu}_0/(N-1)$, $2\tilde{\mu}_0/(N-1)$, $3\tilde{\mu}_0/(N-1)$ ... $(N-2)\tilde{\mu}_0/(N-1)$.

We limit our attention to a systems with an almost neutral ground state, in which bridge sites are weaker donors than D, so that $0 < \tilde{z} < \tilde{x}$. For $\tilde{x} - \tilde{z} >> \tilde{\tau}$ bridge states become very high in energy and a perturbative treatment on $\tilde{\tau}/(2\tilde{x} - 2\tilde{z})$ reduces the N-state model to an effective two-

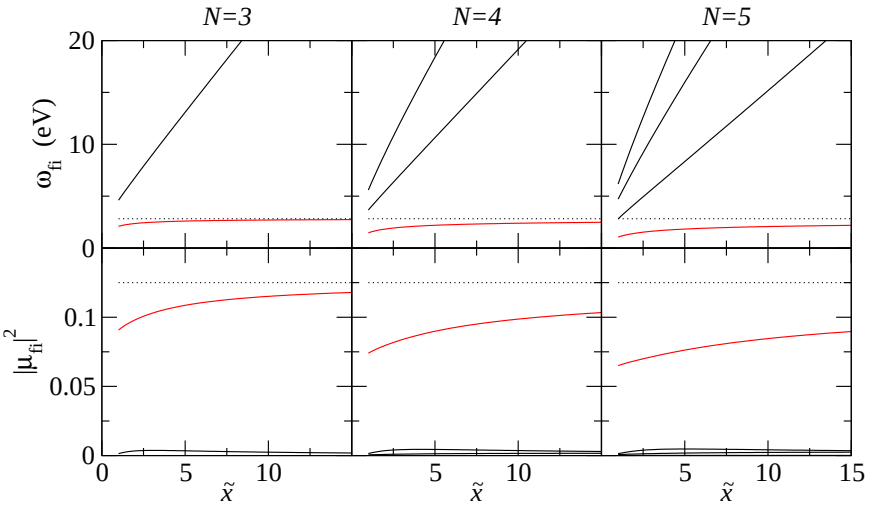

Figure 2.13: Transition energies (top panels) and squared transition dipole moments (bottom panels) calculated for $N = 3$, 4 and 5 state models (panels from left to right) with $\tilde{z}$= 1, $\tilde{\mu}_0$= 1, variable $\tilde{x}$ and $\tilde{\tau}$= $\left(\tau(2\tilde{x})^{N-2}\right)^{\frac{1}{N-1}}$. Red lines refer to the lowest energy (main CT) transition. Dotted lines show the ($\tilde{x}$-independent) results relevant to the limiting two-state model (see text).

state model with $z = \tilde{z}$, $\mu_0 = \tilde{\mu}_0$ and

$$\tau = \frac{\tilde{\tau}^{N-1}}{(2\tilde{x} - 2\tilde{z})^{N-2}} \tag{2.23}$$

where, as before, the tilde applies to symbols relevant to the N-state model, while bare symbols refer to the two-state model.

N-site (or N-state) molecules have $N-1$ optical excitations whose energies and transition dipole moments are shown in figure 2.13 as a function of $\tilde{x}-\tilde{z}$ for systems with $N = 3$, 4, and 5 sites. In all cases, model parameters have been chosen as to converge, in the large $\tilde{x}$ limit, to the two-state model with $z = \tau = 1$, and $\mu_0 = 1$ (in this section, we work with dimensionless quantities, fixing τ as the energy unit and μ_0 as the unit dipole moment). With this choice, we expect convergence, in the large $\tilde{x}$ limit, to a two-

state model with $\rho \approx 0.15$ (see equation (2.5)). The corresponding limiting values of the transition frequency and squared transition dipole moments ($\omega_{CT} \approx 2.8$ and $\mu_{CT} \approx 0.13$; see equations (2.6) and (2.7)) are shown as dotted lines in figure 2.13. The lowest energy or main CT transition (marked by red lines in figure 2.13) is well separated from higher energy transitions involving bridge states and has by far the largest intensity: the main CT transition dominates the low energy portion of the spectrum. The corresponding energies and transition dipole moments (red lines in figure 2.13) properly converge toward the two-state limit (dotted lines) for $\tilde{x} - \tilde{z} \rightarrow \infty$ (or equivalently $\tilde{x} \rightarrow \infty$). The convergence becomes slower with increasing N.

To investigate the effect of bridge states in the definition of an effective two-state model and in particular on the estimate of the relevant dipole length, we focus attention on this lowest energy main CT absorption, disregarding higher energy transitions involving the bridge. In other terms, we analyze the data relevant to the main CT transition, obtained from the diagonalization of the N-state model, to extract an effective two-state model in an analogous way as usually done by analyzing experimental absorption spectra. In particular, the parameters of the effective two-state model, τ, z (or equivalently ρ), and μ_0, can be estimated from three spectral properties. Equations (2.6), (2.7) and (2.9) are therefore used to extract ρ, τ, and μ_0 out of the transition frequency, transition and mesomeric dipole moment (difference between ground and excited state dipoles, i.e. the quantity directly related to solvatochromism) calculated in the N-state model. The right panel of figure 2.14 shows the $(\tilde{x} - \tilde{z})$ dependence of the effective μ_0 estimated along these lines for the $N = 3$, 4, and 5 state models in figure 2.13. In all cases, the effective μ_0 converges toward the exact limit, $\mu_0 = 1$, for $\tilde{x} \rightarrow \infty$, but it is always underestimated for any finite $\tilde{x}$, i.e. when bridge states are closer in energy to the D^+-π-A^- state. It is worth noting that the

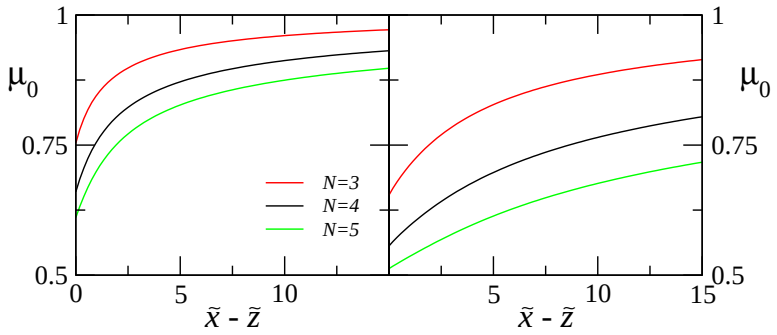

Figure 2.14: Dipole length extracted from the two-state analysis of the main CT band of the N-state models described in figure 2.13. Left panel shows results obtained by extracting the two-state model parameters (x, τ and μ_0) from the frequency, the squared transition dipole moment and the mesomeric dipole moment; right panel shows similar results obtained using the ground state dipole moment instead of the mesomeric dipole moment.

μ_0 underestimate increases with the number of bridge state involved in the D to A CT mechanism. Different estimates of the effective two-state model parameters can be obtained if a different choice is made about the reference spectral properties. In fact, using equations (2.6), (2.7) and (2.8), the parameters of the effective two-state model can be extracted by reproducing the transition frequency, transition dipole moment and ground state dipole moment (instead of mesomeric dipole moment). The effective μ_0 obtained according to this alternative procedure (right panel of figure 2.14) shows a qualitatively similar behavior to the previous one and even larger deviations from the limiting value than before.

This discussion clearly demonstrates that the unphysically small DA distances, extracted from the two-state model analysis of optical spectra of DA molecules, results from the presence of low-lying bridge states, playing an active role in the D to A CT. The larger discrepancy between the geomet-

rical and spectroscopic values of μ_0 obtained for Fc-PTM and Me_9Fc-PTM with respect to common organic DA chromophores, is then naturally explained by the presence of (at least) a secondary low-lying CT transition in the absorption spectra. Moreover this picture explains why this discrepancy is not observed in the μ_0 values obtained from the optical spectra of CT complexes and crystals. In fact the optical properties of CT complex and crystals, where an intermolecular CT occur trough space because of the direct overlap of frontier orbitals, can be described by the same two state model of DA molecules. However in these systems, where the D to A CT is not mediated by any virtual state, the dipole lengths obtained from the intensity of the CT bands are well comparable with geometrical distances. [111, 112, 113, 114]

2.4.3 Bistability in crystals of three-state molecules

In the previous section we introduced a specific three-state model for the description of the low energy physics of Fc-PTM (and Me_9Fc-PTM), governed by intermolecular CT. Following the bottom up modeling approach presented in section 2.2 and in strict analogy with the model for a crystal of two-state molecules presented in section 2.3.2, we now develop a model for a crystal of three-state molecules. When molecular units are modeled by the three-state electronic Hamiltonian (2.18), the charge distribution on each molecule is described by the two operators $\hat{\rho}^D$ and $\hat{\rho}^\pi$, defined in equation (2.19). The electrostatic intermolecular interaction term in in equation (2.1) is written as

$$\hat{V}_{ij} = V_{ij}\,\hat{\rho}_i^D\hat{\rho}_j^D \;+\; V'_{ij}\,\hat{\rho}_i^\pi\hat{\rho}_j^\pi \;+\; V''_{ij}\,\left(\hat{\rho}_i^D\hat{\rho}_j^\pi + \hat{\rho}_i^\pi\hat{\rho}_j^D\right) \tag{2.24}$$

where the coefficients measure the electrostatic interaction energy between i-th and j-th molecules with different charge distributions. Specifically, V_{ij} measures the interaction between the i-th and j-th molecules both in the

D^+-π-A^- state and coincides with the V_{ij} parameter introduced in equation (2.13) for the two-state model; V'_{ij} is instead the interaction between the i-th and j-th molecules both in the D-π^+-A^- state, while V''_{ij} is a mixed term that describes the interaction between the i-th molecule in the D^+-π-A^- state and the j-th molecule in the D-π^+-A^- state or vice versa. We only account for electronic degrees of freedom, since, as discussed in section 2.3.2, molecular vibrations in Fc-PTM play only a marginal role, and can be implicitly considered with a renormalization of the interaction parameters.

In the mean field (mf) approximation the crystal Hamiltonian reduces to

$$H^{(3)}_{mf} = \sum_i \Big[2(\tilde{z} + M\rho^D + M''\rho^\pi)\hat{\rho}^D_i + 2(\tilde{x} + M'\rho^\pi + M''\rho^D)\hat{\rho}^\pi_i - \tilde{\tau}\hat{\sigma}^{(3)}_i \Big] - N\left(M(\rho^D)^2 + M'(\rho^\pi)^2 + 2M''\rho^D\rho^\pi\right) \tag{2.25}$$

where M is the half Madelung energy as defined in equation (2.14),

$$M' = \frac{1}{2N}\sum_{i,j} V'_{ij} \tag{2.26}$$

is the interaction energy of a molecule in the D-π^+-A^- state with the surrounding molecules in the same state, and similarly

$$M'' = \frac{1}{2N}\sum_{i,j} V''_{ij} \tag{2.27}$$

is the interaction energy of a molecule in the D-π^+-A^-state with surrounding molecules in the D^+-π-A^- state (or vice versa). As it is always the case, the mf Hamiltonian leads to a self consistent problem whose solution can be found iterating on the two parameters, ρ^D and ρ^π, corresponding to the ground state expectation values of the $\hat{\rho}^D$ and $\hat{\rho}^\pi$ operators, respectively.

The estimate of the generalized Madelung energies M' and M'', entering the three-state mf Hamiltonian in equation (2.25) (or equivalently of the V'_{ij} and V''_{ij} terms entering the interaction Hamiltonian in equation (2.24)), is a delicate issue. In fact, it requires information about the charge distribution

in the D-π^+-A$^-$ state. As discussed in section 2.3.3, we can force the Fc-PTM molecule into a D$^+$-π-A$^-$ state by applying a static electric field, but there is no numerical way to force the Fc-PTM molecule in the D-π^+-A$^-$ state. We therefore use the crudest approximation, and estimate the interactions accounting for unit charges located at the centroids of the D, A and π-bridge. Locating the centroids of the D group on the Fe atom and that of the A sites on the central C atom of PTM, one estimates $M = -0.72\ eV$. Locating the π-bridge centroid midway between the D and A centroids, we get $M' = 0.41\ eV$ and $M'' = 0.41\ eV$. These values of the generalized Madelung energies are very rough and probably represent a lower limit to the actual values. Therefore we use these values just to set the relative magnitude of the three energies as $M' = M'' = 0.6M$. With these ratios fixed, we solve by iteration the self consistent mf Hamiltonian in equation (2.25) for the (electronic) molecular parameters obtained from the three-state analysis of the two CT bands of Fc-PTM, reported in table 2.3.

Figure 2.15 shows the calculated M-dependence of ρ^D, the charge residing on the D site. Blue circles in the figure refer to a self-consistent iterative solution obtained starting with a N guess ($\rho^D \approx 0$, $\rho^\pi \approx 0$), while red crosses refer to solutions obtained starting from an I guess ($\rho^D \approx 1$, $\rho^\pi \approx 0$). The results are similar to those obtained with the two state molecular model (cf. figure 2.5). For $M > -1.2\ eV$ the ground state of the crystal corresponds to a collection of largely N molecules ($\rho^D \approx 0$) that turn I ($\rho^D \approx 1$) for $M < -2.9\ eV$. On the other hand, starting from the I side and decreasing $|M|$, the molecules stay I down to $M < -1.2\ eV$. For $-2.9 < M < -1.2\ eV$, a wide bistability region is found where a largely N and a largely I are both accessible to the system. The width of the bistability window depends on the M'/M and M''/M ratios, and increases when the two ratios decrease. In any case, apart from quantitative aspects, bistability is a robust phenomenon, and survives for reasonable choices of the generalized Madelung energies.

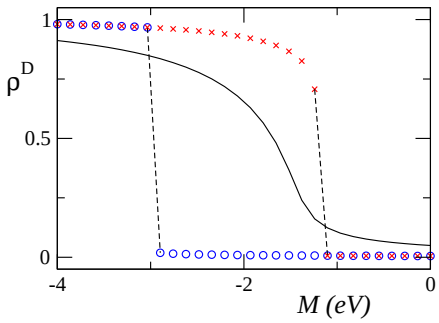

Figure 2.15: The M-dependence of ρ^D for a crystal of three-state molecules described by mf Hamiltonian (2.25), calculated for $\tilde{z} = 0.78\ eV$, $\tilde{x} = 0.87\ eV$, attractive intermolecular interactions ($M' = M'' = 0.6M < 0$) and two different $\tilde{\tau}$. Black continuous line refers to $\tilde{\tau} = 1\ eV$. Blue circles and red crosses correspond to the two solutions obtained for $\tilde{\tau} = 0.47\ eV$, via a self-consistent iterative procedure with the initial choice of ρ^D set to 0 and 1, respectively (the initial values of ρ^π is set to 0 in both cases). Dashed lines are drawn as guide for the eyes.

As observed for the two-state model, bistability is suppressed by increasing the hybridization energy (cf. continuous curve in figure 2.15 obtained for $\tau = 1\ eV$).

2.5 Discussion and conclusions

Electrostatic interactions in molecular materials with low-lying CT degrees of freedom are responsible for an interesting and rich physics, eventually resulting in extreme cooperative phenomena as the occurrence of first order phase transitions and the related phenomena of multistability. [20, 82] The most impressive example of the coupling between CT and electrostatic interaction, is surely provided by the N-I phase transition (NIT) in mixed stack CT crystals [26, 27], as extensively discussed in chapter 1. The fundamental role of intermolecular electrostatic interactions was early recognized by McConnell, that about 15 years before the discovery of NIT, predicted the possibility of discontinuous N-I crossovers and suggested the phenomenon of phase coexistence [24].

Mixed stack CT crystals share some basic physics with crystals of DA chromophores, but, while in CT crystals the intermolecular CT leads to delocalized electrons in 1D, in crystals of DA molecules electrons are completely localized within each molecular unit. The strict confinement of electrons greatly simplifies the description of these systems, without spoiling the cooperative nature of electrostatic intermolecular interactions. [20, 82] The possible appearance of discontinuous charge crossovers and bistability in crystals of DA molecules has been proposed a few years ago, [20] but so far this suggestion has not found experimental demonstration. Here, a detailed analysis of optical spectra of Fc-PTM in solution, and the specific modeling of electrostatic intermolecular interactions in the crystal, quantitatively explains the coexistence of N and I Fc-PTM species, in terms of bistability induced by electrostatic interactions.

The basic physics of interacting DA molecules can be described adopting a two state model for the molecular units, that can be reliably parametrized for specific compounds from a detailed analysis of solution spectra. The

procedure, called bottom up modeling, is simple and exploits the important solvatochromism shown by absorption spectra of DA chromophores to define an environment independent molecular model that is then transferred to describe the molecule in the crystal. [86, 87, 90, 83] Specific and reliable description of intermolecular electrostatic interactions can be obtained by combining structural data with molecular charge distribution, obtained from quantum chemical calculations.

The two state model captures the basic physics of intramolecular CT in DA molecules, and provides an adequate description of optical spectra of Fc-PTM and several chromophores. [91, 92, 93, 94, 96] Quite unavoidably, however, it leads to an oversimplified description of the molecular properties. In section 2.4.1 we have shown that, the presence of a secondary CT absorption in Fc-PTM and Me_9Fc-PTM, suggests the introduction of a third state in the electronic molecular model, to account for the active role of the π-bridge. The three-state model description enable us to better describe the spectroscopic properties of Fc-PTM and Me_9Fc-PTM. Moreover, by introducing the three-state model and its N-state generalization, we were able to solve the long-standing problem of the underestimation of DA distances, as obtained on a two-state interpretation of spectroscopic data. While spectral properties are largely affected by the presence of low-lying bridge states, the bistability induced by electrostatic interactions is a robust phenomenon that does not depend on the specific model adopted to describe molecular units. The basic physics of bistability in crystals of DA molecules is already captured in the simplest two-state molecular model: more refined models may change some details, but do not alter the global picture.

The mf treatment of electrostatic intermolecular interactions leads to a very simple picture of intramolecular CT degrees of freedom coupled by electrostatic intermolecular interactions. The mf approximation, not accounting for many-body correlations, most probably overestimates the bistability re-

gion. However, the comparison with exact results obtained for linear clusters of DA molecules [20] gives us confidence on the reliability of the mf for the ground state properties of these kind of system. Moreover, exact diagonalization can be performed only on small finite size clusters that can hardly reproduce the long range nature of electrostatic interactions. On more general grounds, it is well known that in discontinuous transitions, involving the simultaneous switching of a macroscopic number of molecules, cooperative interactions provide kinetic barriers between the two phases and the relaxation from metastable states towards thermal equilibrium can be a very slow process.

Bistability in crystal of DA molecules induced by electrostatic interactions is a new and interesting finding that opens the way to many future perspectives. A priority, in order to confirm or refuse the predicted mechanism, is represented by the study of pressure effects. In fact, the application of pressure and the consequent lattice contractions are expected to alter the strength of the electrostatic interactions. Measurement of Mössbauer spectra under pressure have already been planned. The possibility to photoinduce the transition will be also investigated.

More generally, we hope that our work will trigger systematic studies on other compounds, looking for other bistable systems. The phase diagram in figure 2.7 provides simple guidelines, setting molecular and supramolecular requirements to observe bistability induced by electrostatic interactions in crystals of valence tautomeric molecules. Bistability requires largely N molecules and a delicate balance between molecular ionization energy and electrostatic interactions. The analysis of optical spectra of DA molecules in solution offers a handy procedure to select suitable molecules. Largely N molecules ($z/\tau > 1$ or equivalently $\rho < 0.15$) can be recognized by a CT absorption band showing a weak positive solvatochromism (red shift of the absorption band with the increase of the solvent polarity). For fluorescent

molecules an even more prominent solvatochromism of the fluorescence band is predicted. [91, 92, 93, 94, 96] The second requirement for bistability is related to electrostatic intermolecular interactions in the solid state, that must be attractive and of a comparable strength with the molecular ionization energy ($M \approx -2z$). [20] The Madelung energy of the crystal is a measure of the overall strength of electrostatic intermolecular interactions but unfortunately it is not experimentally accessible, nor easily tuned from the synthetic point of view. In the specific case of Fc-PTM, we estimated M from the crystal structure and a non standard application of quantum chemical calculations. However, useful information on the nature of the interactions can be in general obtained from the analysis of structural data.

To conclude, we mention that a temperature-dependence valence tautomerism, very similar to those observed for Fc-PTM, was recently observed by Kondo *et al.* in a ferrocenyloxodihydrodibenzochromenylium salt (Fc-Pyl$^+$ X$^-$, with X$^-$=TFSI$^-$,PF$_6^-$,BF$_4^-$). [115] Fc-Pyl$^+$ is a Fc-based DA molecular cation characterized by the charge resonance Fc-Pyl$^+$ $\leftrightarrow$ Fc$^+$-Pyl. Quite interestingly the valence tautomerism of Fc-Pyl$^+$, detected also in this case by Mössbauer spectroscopy, depends on the counterion. In particular, while with two counterions (TFSI$^-$ and PF$_6^-$) a growing intensity of the Fc$^+$ doublet is observed with increasing temperature, the Mössbauer spectra of the third compound (counterion BF$_4^-$) presents only the Fc doublet at all the temperature. The counterion-dependent behavior suggests that also in this case electrostatic interactions play an important role. However the model presented here for crystal of DA molecules does not apply to crystals of molecular ions. In fact, while the molecular two-state model apply quite irrespective to the net molecular charge, the treatment of intermolecular interactions in a crystal of molecular ions requires a specific modeling. More effort is therefore needed to understand this intriguing behavior.

Chapter 3

Vibronic Model for Spin Crossover Complexes

3.1 Introduction: spin crossover in metal complexes

The term spin crossover (SC) generally refers to the thermal conversion from a low spin (LS) to a high spin (HS) electronic configuration, observed in some octahedrally coordinated transition metal complexes. [116, 14] The SC phenomenon, discovered by Cambi *et al.* in 1931 [116], results from the presence of two low-lying electronic states, due to the competition between the ligand (or crystal) field and electronic repulsions. In fact an octahedral ligand field splits of the five d orbitals of the metal into a subset of three orbitals (t_{2g} symmetry) and a subset of two orbitals (e_g symmetry) of higher energy. [117] Figure 3.1 shows the LS and HS states for a d^6 configuration in an octahedral field, as relevant for iron(II) complexes. For a strong ligand field, the energy separation between the two manifolds is large and electrons occupy the orbitals of the three lowest energy states, leading to a LS state ($S = 0$, in the specific d^6 case). On the other hand, for weak ligand fields the splitting

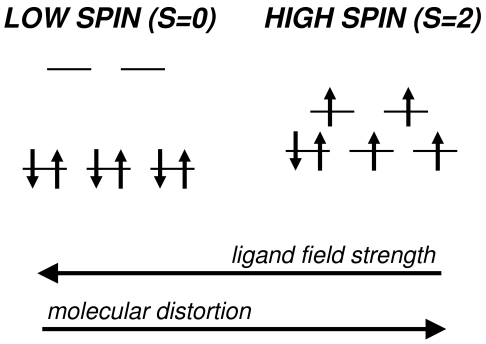

Figure 3.1: Schematic representation on the electronic configurations of the LS and HS state of a transition metal with d^6 configuration in a octahedral ligand field.

is small and electronic repulsions favor a HS state ($S = 2$). The strength of the ligand field, unlike electronic repulsions, is largely affected by the metal-ligand distances and in SC complexes both the electronic configurations are stable, corresponding to different molecular geometries. [118, 117]

The SC phenomenon can be described as a thermal equilibrium between the LS and the HS (meta)stable forms. The LS to HS conversion with increasing temperature is entropically driven, due to higher density of states of the HS state. This higher density of states partially results from the higher spin degeneracy of the HS state, but a major contribution comes from vibrational degrees of freedom. [119, 120] In the HS state, in fact, the metal-ligand bonds are weaker, and the the LS-HS conversion is accompanied by the softening of many vibrations, resulting in a higher density of vibrational levels. The SC is fairly common and was observed in many transition metal complexes with electronic configurations from d^4 to d^7. [14] Among them, the iron(II) complexes are by far the most studied.

For almost isolated SC molecules (such as complexes in solution or in diluted crystals) the temperature dependence of the fraction of complexes

in the HS is gradual and follows a Boltzmann distribution between the two states. More interestingly, in neat SC crystals cooperative interactions of elastic origin, due to the large differences in metal-ligand bond lengths (0.12-0.2 Å), [121, 122, 123] result in steeper transition curves, up to the occurrence of first order phase transitions. Moreover, a large variety of intriguing behaviors, including abrupt transitions, hysteresis loops, transitions with and without accompanying structural transformations, stepwise and partial transitions, have been reported. [14] The application of external pressure strongly affects the spin transition and generally stabilize the LS state. [124] The spin transition is also affected by the application of high magnetic fields. [125]

SC systems represent one of the most representative and promising examples of bistability in molecular crystals, as evidenced by the presence of hysteresis loops and photoinduced phase transitions (light induced excited spin state trapping, LIESST). [9, 126] In particular the possibility to reversibly switch between two phases [127, 126, 128], characterized by different optical and magnetic properties, makes SC systems suitable candidates for multifunctional molecular materials. [129, 130] Interesting applications as molecular switches, memory devices and displays have already been demonstrated. [130]

Several models have been proposed to explain the cooperativity in SC systems. [131, 132, 133, 134, 135, 136, 137] These models allowed to understand the cooperative nature of the spin transition and provided quantitative explanations of most of its features. However, the development of microscopic models based on a realistic quantomechanic description of SC molecules, has not been pursued yet.

A microscopic model for SC complexes was developed by Biernacki and Clerjaud [138] by introducing an adiabatic linear dependence of the strength of crystal field on a totally symmetrical molecular vibration (breathing mode).

Following the basic idea in ref. [138], here we present a quantomechanic model for the coupling between electronic and vibrational degrees of freedom. More specifically, we introduce linear and quadratic coupling to the breathing mode, to explicitly account for different equilibrium geometries and vibrational frequencies of LS and HS states. Moreover, we explicitly introduce the mixing between LS and HS states, provided by higher order spin-orbit coupling and responsible for the relaxation (tunneling) from the photoexcited HS state. [139] The quantomechanical and thermal properties of the model are obtained via exact (non-adiabatic) diagonalization for a physically reasonable set of parameters. These results are discussed and compared with the results obtained in the adiabatic approximation in section 3.2. The molecular model is then adopted to study the cooperative effects of intermolecular interactions. The effects of different phenomenological interaction terms, treated within the mean field approximation, are discussed in section 3.3.

3.2 The vibronic model for spin crossover molecules

3.2.1 The model

The electronic structures of a SC complex can be described on the basis of one LS state and g degenerate HS states, where g is the multiplicity of the HS state. Being 2Δ the energy gap between the LS and the HS states and J the corresponding mixing matrix element, the electronic Hamiltonian reads

$$H = \Delta\ \hat{\sigma}_g + J\ \hat{\sigma}_g^x \tag{3.1}$$

where

$$\hat{\sigma}_g\ = -|LS\rangle\langle LS| + \sum_{k=0}^{g-1} |HS_k\rangle\langle HS_k| \tag{3.2}$$

$$\hat{\sigma}_g^x\ = \sum_{k=0}^{g-1} (|LS\rangle\langle HS_k| + |HS_k\rangle\langle LS|) \tag{3.3}$$

For the sake of simplicity, and in the lack of specific experimental data, we assume that the same matrix element, J, couples the LS state to all the g HS states. Although the assumption of the same J for all HS states is probably a rough approximation, it represent, at least, a useful starting point for subsequent perturbative treatments. With this assumption, the g HS states are equivalent and Hamiltonian (3.1) is invariant with respect to their permutations. We introduce the symmetry adapted linear combinations of the HS states:

$$|HS_k^*\rangle = \frac{1}{\sqrt{g}} \sum_{l=0}^{g-1} e^{2\pi i \frac{kl}{g}}\ |HS_l\rangle \qquad \text{with}\ \ k = 0, 1, 2...g-1 \tag{3.4}$$

The representation of Hamiltonian (3.1) on the basis of LS state and of the g symmetry adapted HS states is a block diagonal matrix: the original Hamiltonian matrix of dimension $g+1$ factorizes in a bidimensional block plus $g-1$ monodimensional blocks.

The bidimensional block mixes the $|LS\rangle$ and $|HS_0^*\rangle = \frac{1}{\sqrt{g}}(|HS_0\rangle + |HS_1\rangle + |HS_2\rangle + ... + |HS_{g-1}\rangle)$, and in this subspace the electronic Hamiltonian can be written as

$$H_2 = \Delta\ \hat{\sigma}^z + J'\ \hat{\sigma}^x \tag{3.5}$$

where $\hat{\sigma}^z$ and $\hat{\sigma}^x$ are the Pauli matrices and $J' = \sqrt{g}J$. The energy spectrum of Hamiltonian (3.1) is constituted by energies $\pm\sqrt{\Delta^2 + J'^2}$, obtained diagonalizing the bidimensional block, and $g-1$ unperturbed levels of energy Δ, due to uncoupled HS states.

Molecular vibrations (mv) are introduced to account for the different equilibrium geometries [121, 122, 123] and vibrational frequencies [140, 141, 142, 120] in the LS and HS states. We consider a single effective mv, corresponding to the totally symmetric deformation of the molecule (breathing mode). Harmonic potentials are assigned to the electronic basis states, with equilibrium positions and force constants depending on the spin state. The resulting electron-mv (e-mv) Hamiltonian includes both linear and quadratic coupling:

$$H = \left(\Delta - l\hat{q} - \lambda\hat{q}^2\right)\hat{\sigma}_g + J\hat{\sigma}_g^x + \frac{1}{2}k\hat{q}^2 + \frac{\hat{p}^2}{2m} \tag{3.6}$$

where $\hat{q}$ is the position operator of the coupled mv, with conjugated momentum $\hat{p}$ and effective mass m. k is the force constant of the uncoupled system while l and λ are the linear and quadratic e-mv coupling constants, respectively. The harmonic potential of the $|LS\rangle$ state is characterized by a force constants $k_{LS} = k + 2\lambda$ and an equilibrium position $q_{LS}^{eq} = -l/k_{LS}$, while the potential of the $|HS_0^*\rangle$ state has $k_{HS} = k - 2\lambda$ and $q_{HS}^{eq} = l/k_{HS}$.

Hamiltonian (3.6) is still invariant with respect to permutations of the HS states and with the implementation of symmetry the problem factorizes and becomes easier to handle. In the subspace $\{|LS\rangle, |HS_0^*\rangle\}$ Hamiltonian (3.6) describes two displaced harmonic oscillators with different frequencies

coupled by J', as follows:

$$H_2 = \left(\Delta - l\hat{q} - \lambda\hat{q}^2\right)\hat{\sigma}^z + J'\hat{\sigma}^x + \frac{1}{2}k\hat{q}^2 + \frac{\hat{p}^2}{2m} \tag{3.7}$$

The vibronic Hamiltonian for each of the states $|HS_k^*\rangle$, with $k = 1, 2 \ldots g-1$, describes a displaced harmonic oscillator

$$H_{HS} = \Delta + \frac{1}{2}k_{HS}\hat{q}^2 - l\hat{q} + \frac{\hat{p}^2}{2m} \tag{3.8}$$

The energies of vibronic levels are

$$E_n^{HS} = \Delta + \hbar\omega_{HS}\left(n + \frac{1}{2}\right) - \frac{l^2}{2k_{HS}} \tag{3.9}$$

where $\omega_{HS} = \sqrt{k_{HS}/m}$. Eigenstates of Hamiltonian (3.8) are purely HS states, i.e. $\langle\hat{\sigma}_g\rangle = 1$ and $\langle\hat{q}\rangle = l/k_{HS}$. Since Hamiltonian (3.8) is already diagonal on its natural basis, in the following we will concentrate on Hamiltonian (3.7), relevant to the subspace $\{|LS\rangle, |HS_0^*\rangle\}$.

3.2.2 Exact and adiabatic solution of the vibronic problem

Hamiltonian (3.7) can be solved either exactly or within the adiabatic approximation. The non-adiabatic problem can be set up by writing the Hamiltonian on a basis obtained as the direct product of the two electronic states $\{|LS\rangle, |HS_0^*\rangle\}$ times the eigenstates $|n\rangle$ of an undisplaced harmonic oscillator:

$$H_{basis} = \frac{\hat{p}^2}{2m} + \frac{1}{2}k\,\hat{q}^2 \tag{3.10}$$

The vibronic basis set then reads

$$\begin{aligned} |LS, n\rangle &= |LS\rangle \otimes |n\rangle \\ |HS_0^*, n\rangle &= |HS_0^*\rangle \otimes |n\rangle \end{aligned} \tag{3.11}$$

The vibronic basis is infinite and, to maintain the problem tractable, we truncate the basis to large enough n values as not to affect the quantities of interest.

The eigenfunctions of (3.7) are expressed as a linear combinations of the basis states

$$\Psi_k = \sum_n c_{nk}^{LS} \; |LS, n\rangle + c_{nk}^{HS} \; |HS_0^*, n\rangle \tag{3.12}$$

The expectation values of the operators $\hat{\sigma}^z$ and $\hat{q}$ of the k-th vibronic level are calculated as follow

$$\langle \Psi_k | \hat{\sigma}^z | \Psi_k \rangle = \sum_n \left| c_{nk}^{HS} \right|^2 - \left| c_{nk}^{LS} \right|^2 \tag{3.13}$$

$$\begin{aligned} \langle \Psi_k | \; \hat{q} \; | \Psi_k \rangle = & \sqrt{\frac{\hbar}{2m\omega}} \sum_n \Big[\sqrt{n} \left(c_{n,k}^{LS} \; c_{n-1,k}^{LS} + c_{n,k}^{HS} \; c_{n-1,k}^{HS} \right) + \\ & \sqrt{n+1} \left(c_{n,k}^{LS} \; c_{n+1,k}^{LS} + c_{n,k}^{HS} \; c_{n+1,k}^{HS} \right) \Big] \end{aligned} \tag{3.14}$$

The density of probability in the q-space of the k-th level is calculated summing up the densities of probability of its LS and HS components:

$$\begin{aligned} P_k(q) = & |\langle LS | \Psi_k \rangle|^2 + |\langle HS_0^* | \Psi_k \rangle|^2 = \\ = & \Big| \sum_n c_{n,k}^{LS} \; \chi_n(q) \Big|^2 + \Big| \sum_n c_{n,k}^{HS} \; \chi_n(q) \Big|^2 \end{aligned} \tag{3.15}$$

where $\chi_n(q)$ is the wavefunction of the state $|n\rangle$.

The adiabatic or Born-Oppenheimer approximation separates the electronic and vibrational motion on the basis of the different timescales that characterize theirs dynamics. The basic assumption is that the electronic motion is fast enough to react instantaneously to molecular vibrations. Within the adiabatic approximation the wavefunction is written as the product of an electronic and a vibrational part. The electronic adiabatic Hamiltonian is obtained from the exact Hamiltonian (3.7) neglecting the vibrational kinetic energy, so that the position operator $\hat{q}$ becomes a classic variable. The adiabatic q-dependent electronic Hamiltonian matrix is

$$H_2^{BO} = \begin{pmatrix} -\Delta + lq + \lambda q^2 & J' \\ J' & \Delta - lq - \lambda q^2 \end{pmatrix} + \frac{1}{2} k \, q^2 \tag{3.16}$$

The diagonalization of Hamiltonian (3.16) gives the q-dependent adiabatic energies or potential energy surfaces (PES) of the two electronic states

$$E_{\pm}(q) = \frac{1}{2}kq^2 \pm \sqrt{(\,\Delta - lq - \lambda q^2\,)^2 + J'^2} \tag{3.17}$$

and the corresponding eigenvectors

$$\begin{aligned} \psi^{-}(q) &= \sqrt{1-\xi(q)}\;|LS\rangle + \sqrt{\xi(q)}\;|HS_0^*\rangle \\ \psi^{+}(q) &= \sqrt{\xi(q)}\;|LS\rangle - \sqrt{1-\xi(q)}\;|HS_0^*\rangle \end{aligned} \tag{3.18}$$

where

$$\xi(q) = \frac{1}{2}\left(1 - \frac{(\Delta - lq - \lambda q^2)}{\sqrt{(\Delta - lq - \lambda q^2\,)^2 + J'^2}}\right) \tag{3.19}$$

measures the q-dependent weight of $|HS_0^*\rangle$ in the ground state ψ^{-}. The Hellmann-Feynman theorem provides the equilibrium position of the ground state PES:

$$q_{eq} = \frac{l\,\langle\hat{\sigma}^z\rangle}{k - 2\lambda\langle\hat{\sigma}^z\rangle} \tag{3.20}$$

Figure 3.2 shows the adiabatic PES calculated for different J' valued and the set of parameters reported in the caption. In panel **a** ($J' = 0$) the two harmonic potential assigned to the $|LS\rangle$ and $|HS_0^*\rangle$ state are drawn. The LS (HS) oscillator is characterized by equilibrium position $q_{LS}^{eq} = -l/k_{LS}$ ($q_{HS}^{eq} = l/k_{HS}$) and force constant $k_{LS} = k + 2\lambda$ ($k_{HS} = k - 2\lambda$). For finite values of J' (panels **b**-**d**) the mixing term is effective. For relatively small J' ($J' = 10\ meV$ and $J' = 25\ meV$, panels **b** and **c**, respectively), a bistable ground state is obtained. Increasing J' the energy barrier between the two stable geometries lowers, and for large J' the energy barrier vanishes and the PES present a single minimum, as shown in panel **d** for $J' = 55\ meV$.

Vibronic levels and corresponding wavefunctions are obtained by solving, for each electronic eigenstate, the corresponding Schrödinger equation:

$$\left(E_{\pm}(q) + \frac{\hat{p}^2}{2m}\right) X_k^{\pm}(q) = E_k^{\pm}\; X_k^{\pm}(q) \tag{3.21}$$

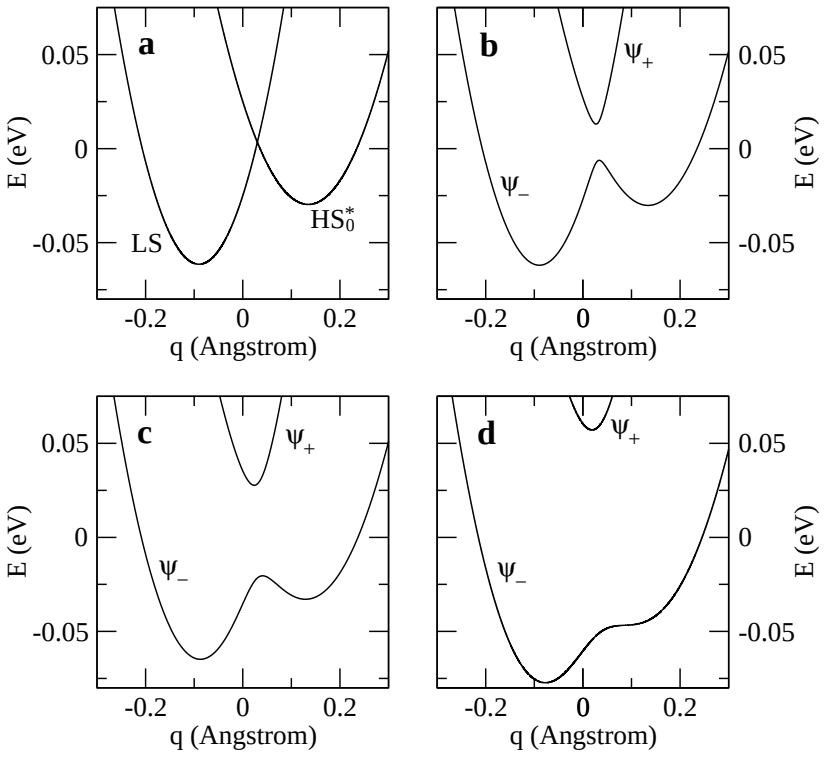

Figure 3.2: Adiabatic PES from equation (3.17) calculated for $\Delta = 25\ meV$, $k = 7.5\ eV/\text{Å}^2$, $l = 0.81\ eV/\text{Å}$, $\lambda = 0.75\ eV/\text{Å}^2$ and $J' = 0$ (panel **a**), $10\ meV$ (panel **b**), $25\ meV$ (panel **c**) and $55\ meV$ (panel **d**).

The adiabatic vibrational Hamiltonian in equation (3.21) is represented on the basis of the eigenfunctions of Hamiltonian (3.10) and numerically diagonalized. Vibrational wavefunctions can be expressed as a linear combinations of the basis states

$$X_k^{\pm}(q) = \sum_n c_{nk}^{\pm}\ \chi_n(q) \tag{3.22}$$

where $\chi_n(q)$ is the wavefunction corresponding to $|n\rangle$. The adiabatic wavefunction is the product of the electronic state in equation (3.18) and of the vibrational wavefunction

$$\Psi_k^{\pm}(q) = \psi^{\pm}(q)\ X_k^{\pm}(q) \tag{3.23}$$

Expectation values of $\hat{\sigma}^z$ and $\hat{q}$ in the k-th vibronic level of the $\psi^{\pm}$ electronic adiabatic state are calculated as follows

$$\langle \Psi_k^{\pm} | \hat{\sigma}^z | \Psi_k^{\pm} \rangle = \pm \int X_k^{\pm}(q)\ (1 - 2\,\xi(q))\ X_k^{\pm}(q)\ dq \tag{3.24}$$

$$\langle \Psi_k^{\pm} | \hat{q} | \Psi_k^{\pm} \rangle = \sqrt{\frac{\hbar}{2m\omega}} \sum_n \Big(\sqrt{n}\ c_{n,k}^{\pm}\ c_{n-1,k}^{\pm} + \tag{3.25}$$

$$+\ \sqrt{n+1}\ c_{n,k}^{\pm}\ c_{n+1,k}^{\pm} \Big) \tag{3.26}$$

The density of probability of the k-th level of the $\psi^{\pm}$ electronic state is the square modulus of the corresponding vibrational wavefunction:

$$P_k^{\pm}(q) = \left| X_k^{\pm}(q) \right|^2 \tag{3.27}$$

It is worth noting that the eigenstates of the the vibronic problem relative to the $|HS_k^*\rangle$, with $k = 1, 2 \ldots g-1$ are exactly adiabatic. In fact, since these states are uncoupled, their wavefunctions are always the product of an electronic HS state and a vibrational wavefunctions.

3.2.3 Model parameters

Experimental data fix reliable estimates of the parameters entering the Hamiltonian (3.6). Information on the LS-HS energy gap 2Δ are obtained from calorimetric measurements and, more specifically, from the enthalpy variation accompanying the spin conversion. Typical values are $5 - 20\ kJ/mol$. [143] The mixing term, J, originated from higher order spin-orbit coupling, is difficult to estimate. Buhks and coworkers, on the basis of ligand field arguments, estimated, for a d^6 configuration, J of the order of 20 meV. [139] The electronic degeneracy of HS states of a metal with d^6 configuration in an octahedral ligand field, including spin and orbital contribution, is $g = 15$. However, because of the lower symmetry of actual geometries, the value $g = 5$, due to only spin multiplicity, is probably a safer estimate. [139]

Vibrational frequencies are directly accessible from spectroscopy. Important variations of the frequencies of the coupled modes upon SC were detected in the wide spectral range $200 - 2000\ cm^{-1}$. [141, 120] However, the most important modes are the lower frequencies ones, that present the larger relative softening, and give the most important contributions to the variation of vibrational entropy. [141, 120, 119] Reasonable values of the ratio between the vibrational frequencies in the HS and LS state are around $0.5 - 0.8$ [119]. This ratio fixes the quadratic coupling constant λ. Force constants of octahedrally coordinated iron complexes, have values in the range $5 - 15\ eV/\text{Å}^2$. [144, 145, 146] With these values for the force constant and a frequency of 300 cm^{-1} the effective mass ranges between 10^{-24} and $2\ 10^{-23}\ Kg$. Finally, the value of the linear coupling constant l is chosen in order to have, according to structural data, a difference of about 0.2 Å between LS and HS equilibrium geometries. [121, 122, 123]

Table 3.1 summarizes the values of the model parameters that will be adopted in most of the following calculations. These values are obtained on the basis of the previous considerations. Parameters J and g are not listed in

Δ (meV)	k $(eV/\text{Å}^2)$	l $(eV/\text{Å})$	λ $(eV/\text{Å}^2)$	m (Kg)
25	7.5	0.81	0.75	1.78 10^{-24}

Table 3.1: Molecular parameters entering Hamiltonian (3.6).

the table. In the following section, where the quantomechanical properties of the model are discussed, we will present results for different values of the relevant parameter $J' = \sqrt{g}J$. In the discussion of thermodynamic properties in section 3.2.5, the effects of g and J are treated separately.

3.2.4 Quantum mechanical properties of a SC molecule

In this section we present results from the exact and adiabatic diagonalization of Hamiltonian (3.7), relevant to the subspace $\{|LS\rangle, |HS_0^*\rangle\}$. The results are obtained for the set of parameters reported in table 3.1 and $J' = 0$, 10, 25 and 55 meV.

Hamiltonian (3.8), for the $|HS_k^*\rangle$ (with $k = 1, 2 \ldots g$–1) uncoupled states, simply describes displaced harmonic oscillators. The vibronic levels of uncoupled HS states are equivalent to those of the $|HS_0^*\rangle$ basis state and will not be further discussed.

We start with the trivial case of unmixed LS and HS states ($J' = 0$). In this case Hamiltonian (3.7) describes two uncoupled harmonic oscillators and the energy spectrum is

$$E_n^{LS} = -\Delta + \hbar\omega_{LS}\left(n + \frac{1}{2}\right) - \frac{l^2}{2k_{LS}} \tag{3.28}$$

$$E_n^{HS} = \Delta + \hbar\omega_{HS}\left(n + \frac{1}{2}\right) - \frac{l^2}{2k_{HS}} \tag{3.29}$$

where $\omega_{LS} = \sqrt{k_{LS}/m}$ and $\omega_{HS} = \sqrt{k_{HS}/m}$ are the vibrational frequencies of LS and HS state, respectively. The left panel of figure 3.3 shows the adiabatic PES (black thick line), that for $J' = 0$ coincide with the diagonal

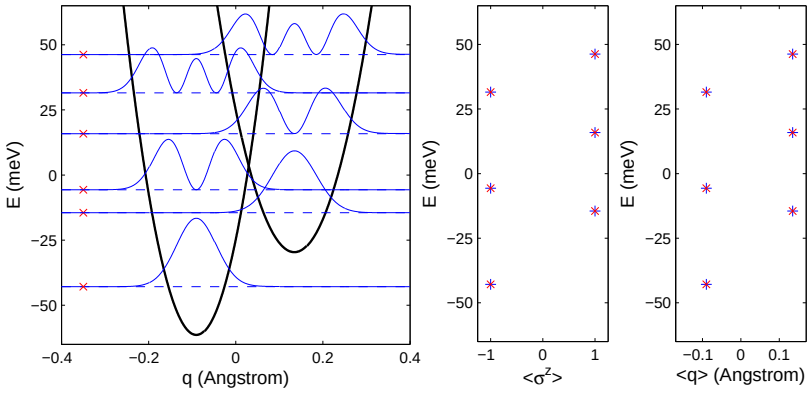

Figure 3.3: Left panel: adiabatic PES (black thick lines), exact (blue dashed lines) and adiabatic (red crosses) vibronic levels and the corresponding exact density of probability (blue continuous lines). Central panel: exact (blue plus) and adiabatic (red crosses) values of $\langle\hat{\sigma}^z\rangle$. Right panel: exact (blue plus) and adiabatic (red crosses) values of $\langle\hat{q}\rangle$. Results obtained for from Hamiltonian (3.7) with parameters of table 3.1 and $J' = 0$.

energies of Hamiltonian (3.16). Superimposed in the same figure are shown the exact energies of vibronic levels (blue dashed lines) and the corresponding densities of probability (blue continuous line). Red crosses on the left side of the figure mark the energy of vibronic levels calculated in the adiabatic approximation. Central and right panels report exact (blue plus) and adiabatic (red crosses) values of $\langle\hat{\sigma}^z\rangle$ and $\langle\hat{q}\rangle$, respectively. In the absence of mixing, the two oscillators coincide with the basis states and the adiabatic solution is exact.

For finite J', Hamiltonian (3.7) ((3.21) in the adiabatic case) cannot be solved analytically, and the analysis relies on numerical diagonalization. Results presented in the following are obtained with a phonon basis truncated at $n = 19$ (20 states). The dimension of basis basis set is large enough as

not to affect the energies of the thermodynamically relevant levels.

Figure 3.4 shows results obtained for a system with $J' = 10\ meV$. Same quantities of figure 3.3 are shown and same symbols are adopted. In this case J' is small compared with the energy gap 2Δ, and the level scheme does not differ too much from the case $J' = 0$ (c.f. left panel of figure 3.3). The density of probability of vibronic levels still resembles the case of two uncoupled oscillators. However, levels with comparable or higher energy with respect to the top of the energy barrier are more delocalized, showing a small but finite probability in the whole domain of q. The minimal degree of mixing between the electronic states is confirmed by the expectation values of $\langle \hat{\sigma}^z \rangle$ (blue plus, central panel of figure 3.4) that are very close to the values ± 1 of pure LS/HS states. Same argument holds also for $\langle q \rangle$ (blue plus, right panel of figure 3.4) that barely differs from the values of pure LS and HS states.

The adiabatic approximation, with the exception of the ground state, provides energy levels that are significantly different from exact values (red crosses, left panel of figure 3.4) and fails, even more clearly, in the calculation of the expectation values $\langle \sigma^x \rangle$ and $\langle q \rangle$ (red crosses, central and right panels of figure 3.4). In general, adiabatic eigenstates overestimate the mixing between LS and HS (see expectation values of $\langle \hat{\sigma}^z \rangle$ in the central panel of figure 3.4). The higher LS-HS mixing obtained in the adiabatic approximation results in more delocalized densities of probability with respect to exact results, as shown in detail for the first four vibronic levels in figure 3.5. The failure of the adiabatic approximation is not surprising: in fact when the differences between electronic energies are comparable to the vibrational frequencies the separation of the two motions is no more a valid approximation.

Figure 3.6 shows the results for a system with $J' = 25\ meV$. The energy levels now substantially differ from the case of uncoupled oscillators (c.f. left

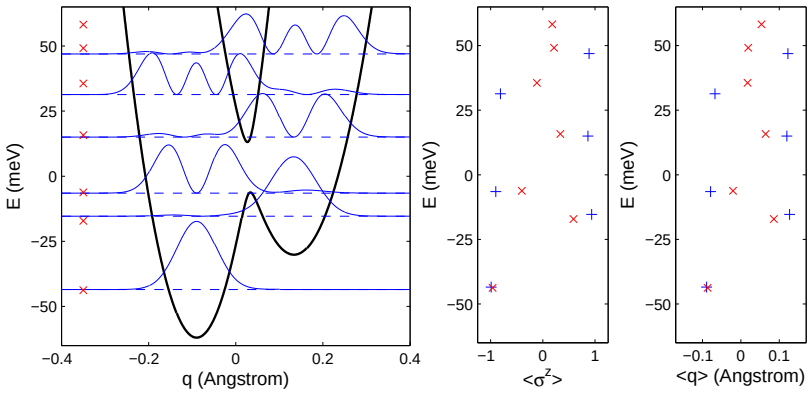

Figure 3.4: Same quantities reported in figure 3.3, obtained for parameters of table 3.1 and $J' = 10\ meV$.

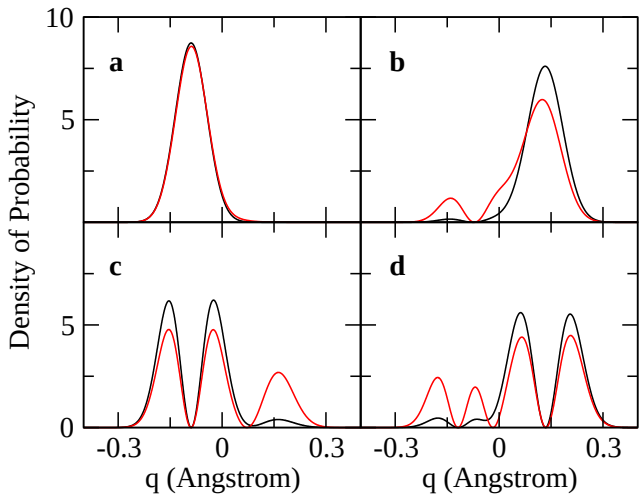

Figure 3.5: Exact (black lines) and adiabatic (red lines) density of probability of the ground state (panel **a**) and of the first three excited vibronic levels (panels **b-d**) obtained for parameters in table 3.1 and $J' = 10\ meV$.

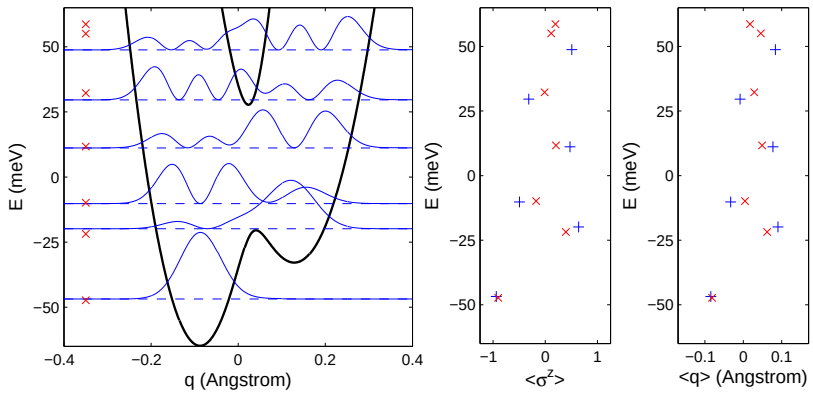

Figure 3.6: Same quantities reported in figure 3.3, obtained for parameters of table 3.1 and $J' = 25\ meV$.

panel of figure 3.3) and the corresponding densities of probability, with the exception of the ground state, extend in a larger q region. As shown in the central and right panels of figure 3.6, the values of $\langle\hat{\sigma}^z\rangle$ and $\langle\hat{q}\rangle$ indicates that, although the ground state still resembles a pure LS state, higher energy states are a mixture of LS and HS states, with comparable weights. The adiabatic approximation fails both for energy levels and expectation values (see figure 3.6). The failure of the adiabatic approximation, although less evident than for $J' = 10\ meV$, is recognized also in the probability distributions, shown in figure 3.7.

Figure 3.8 refers to a system with $J' = 55\ meV$. In this case J' is large enough to completely remove the energy barrier so that the ground state PES (black thick lines in left panel of figure 3.8) presents a single minimum. The shape of the ground state PES is qualitatively different from the previous cases and the energy levels are completely different than for the uncoupled oscillators (notice different energy scales in figures 3.8 and 3.3). Densities of probability, with the exception of the ground state, are completely delocalized in the q-space (see continuous blue lines in left

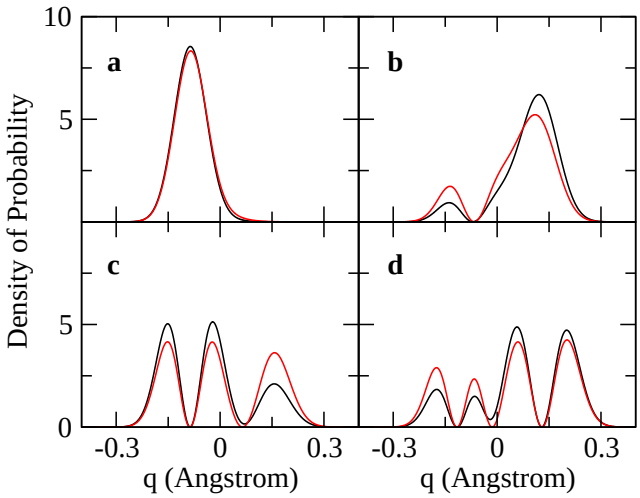

Figure 3.7: Exact (black lines) and adiabatic (red lines) density of probability of ground state (panel **a**) and the first three excited vibronic levels (panels **b-d**) obtained for parameters in table 3.1 and $J' = 25\ meV$.

panel of figure 3.8). As shown in the central and right panels of figure 3.8, the values of $\langle\hat{\sigma}^z\rangle$ and $\langle\hat{q}\rangle$ indicates that, although the ground state still resembles to a LS state, higher energy states are mixtures, with almost equal proportions, of LS and HS states. The adiabatic approximation provides in this case reliable results: adiabatic energy levels, expectation values (central and right panels of figure 3.8) and densities of probability (figure 3.9) are extremely similar to exact results. In fact, for large J', the energy gap between the ground and the excited state is larger than the vibrational frequencies and the adiabatic approximation works pretty well.

We notice that for $\lambda = 0$, independently of other model parameters, for each of the vibronic levels we have $\langle\hat{q}\rangle = (l/k)\langle\hat{\sigma}^z\rangle$. Although the e-mv coupling naturally leads to a correlation between spin state and molecular distortion, this result is quite unexpected since the two operators are intrinsically different and the corresponding expectation values are obtained

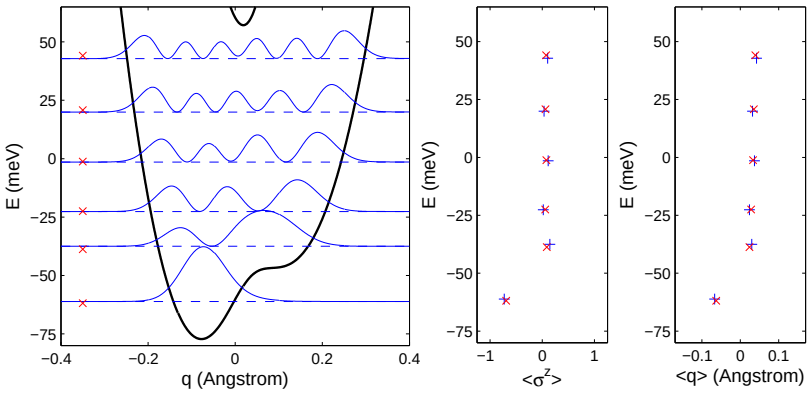

Figure 3.8: Same quantities reported in figure 3.3, obtained for parameters of table 3.1 and $J' = 55\ meV$.

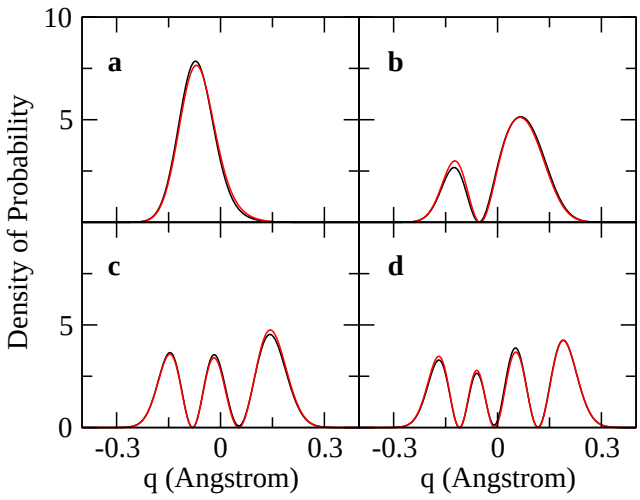

Figure 3.9: Exact (black lines) and adiabatic (red lines) density of probability of ground state (panel **a**) and the first three excited vibronic levels (panels **b-d**) obtained for parameters in table 3.1 and $J' = 55\ meV$.

from different expressions (c.f. equations 3.14 and 3.13). It is worth noting that this result is not a consequence of the Helmann-Feynman theorem, that relates the equilibrium points of the *adiabatic* PES to the expectation value of the electronic operator.

3.2.5 Thermodynamic properties of a SC molecule

The vibronic model presented in section 3.2.1 (non-adiabatic results) is applied here to describe the thermal LS to HS conversion observed in solvated complex or diluted crystals. The thermal behavior of non interacting SC complexes, described by the model Hamiltonian in equation (3.6), is calculated in the standard framework of the canonical ensemble. [71] The partition function of the system is

$$Z = \sum_i e^{-\frac{E_i}{k_B T}} \tag{3.30}$$

where E_i are the eigenvalues of Hamiltonian (3.6), T is the absolute temperature and k_B is the Boltzmann constant. The thermal average of a generic observable, described by the operator $\hat{A}$, is calculated as

$$\langle \hat{A} \rangle = \frac{1}{Z} \sum_i A_i \; e^{-E_i/k_B T} \tag{3.31}$$

where A_i is the expectation value of operator $\hat{A}$ in the i-th eigenstates. With the vibronic model Hamiltonian in equation (3.6) we have access both to the spin state, described by the electronic operator $\hat{\sigma}_g$, and to the molecular geometry, described by the operator $\hat{q}$. Hereafter the macrospic spin state will be expressed in term of the HS fractions, i.e. the experimentally accessible quantity, defined as

$$n_{HS} = \frac{1}{2}(\langle \sigma_g \rangle + 1) \tag{3.32}$$

The thermal evolution of n_{HS} (transition curve) and $\langle q \rangle$ for a SC complex described by parameters in table 3.1, $g = 15$ and different J are reported

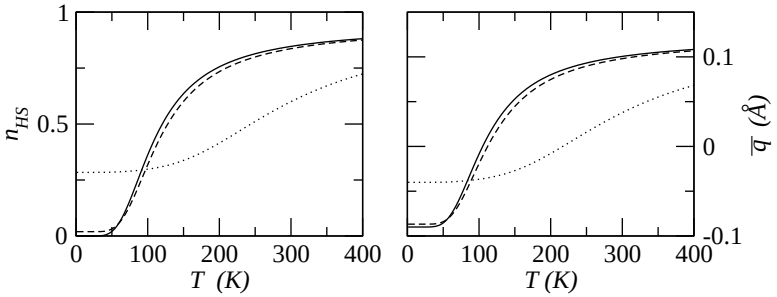

Figure 3.10: n_{HS} and $\langle q \rangle$ calculated for the parameters in table 3.1, $g = 15$ and $J = 0$ eV (continuous line), $J = 5$ meV (dashed line) and $J = 25$ meV (dotted line).

in figure 3.10. The behaviors obtained for $J = 0$ (continuous line) and $J = 5$ meV (dashed line), are similar, corresponding to a gradual and almost complete conversion from a macroscopically LS state to a macroscopically HS state. The change of the spin state is accompanied by an increase of molecular distortion of ~ 0.2 Å. The main difference between $J = 0$ and $J = 5$ meV transition curves appears in the low temperature limit, where only the quantomechanic ground state is relevant. In fact, while for $J = 0$ the ground state is a pure LS state ($n_{HS} = 0$), for finite J a non vanishing HS component in the ground state is always present ($n_{HS} > 0$). This effect is more evident in the $J = 25$ meV curves, where $n_{HS} \approx 0.3$ for $T \rightarrow 0$.

The effect of the different vibrational frequencies in LS and HS is considered in figure 3.11, where are shown the $n_{HS}(T)$ and $\langle q \rangle(T)$ curves for systems characterized by different force constants of the HS state (see figure caption). By lowering k_{HS}, and hence the HS vibrational frequency, we notice a decrease of the equilibrium temperature $T_{1/2}$, defined as the temperature where $n_{HS} = 0.5$. To understand how different vibrational frequencies of LS and HS state affect the equilibrium, we consider the analytical solution for uncoupled oscillators. Specifically, for $J = 0$ the partition function can

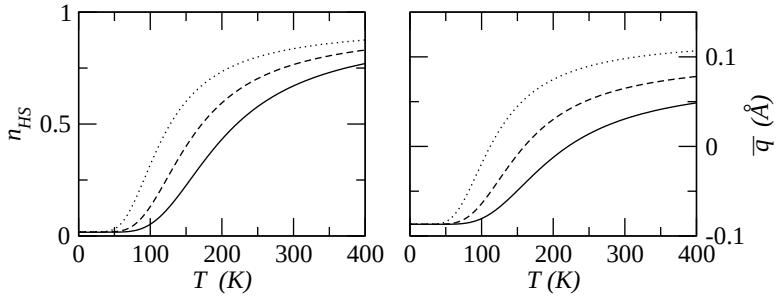

Figure 3.11: n_{HS} and $\langle q \rangle$ calculated for $\Delta = 25\ meV$, $J = 5\ meV$, $g = 15$, $l = 0.81\ eV/\text{Å}$, $m = 1.78\,10^{-24} Kg$, $k_{LS} = 9\ eV/\text{Å}^2$ and $k_{HS} = 9\ eV/\text{Å}^2$ (continuous line), $k_{HS} = 7.2\ eV/\text{Å}^2$ (dashed line) and $k_{HS} = 6\ eV/\text{Å}^2$ (dotted line).

be written as

$$Z = \ e^{\Delta/k_B T} + g_{eff}(T)\ e^{-\Delta/k_B T} \tag{3.33}$$

where

$$g_{eff}(T) = g\ g_{vib}(T)\ \exp\left[\frac{l^2}{2k_B T}\left(\frac{1}{k_{LS}} - \frac{1}{k_{HS}}\right)\right] \tag{3.34}$$

is a T-dependent effective degeneracy of a fictitious HS states in a two-state (Ising-like) picture. The first factor in equation (3.34) is the multiplicity of the HS state g, while the third factor is due to the different zero point energies of the LS and HS oscillators and can be treated as a renormalization of Δ. More interesting is the second term

$$g_{vib}(T) = \frac{\sinh\left(\hbar\omega_{LS}/2k_B T\right)}{\sinh\left(\hbar\omega_{HS}/2k_B T\right)} \tag{3.35}$$

originated by the different vibrational frequencies of LS and HS state. The higher density of vibronic levels in the HS state is therefore responsible for the vibrational contribution to the entropy variation upon SC ($g_{vib} > 1$ for $\omega_{LS} > \omega_{HS}$), as results from figure 3.11. Such a vibrational contribution

favors the conversion to a macroscopic HS state and lowers the equilibrium temperature. The vibrational entropy represents the main contribution to the total entropy variation, because the spin conversion is accompanied by the softening of several vibrational modes. [141, 120, 119] In the hypothesis of many uncoupled modes, in fact, the total g_{vib} is the product of the partial contributions from each vibration.

For the sake of completeness, figure 3.12 shows the temperature dependence of the free energy F, internal energy U, entropy S and heat capacity C, calculated for parameter values in table 3.1, $J = 5\ meV$ and $g = 15$, within the standard framework of the canonical ensemble. [71] The thermodynamic properties of our model, are in qualitative agreement within experimental data. [140, 143] A quantitative agreement cannot be achieved with a single mode picture. In order to show a system presenting an almost complete conversion at room temperature, we compensate for the lack in the vibrational entropy setting the electronic degeneracy to its upper limit $g = 15$.

Figure 3.13 shows the thermal densities of probability in the q-space calculated at different temperatures. The thermal density of probability is calculated by summing up the quantum densities of probabilities of vibronic levels weighted by their Boltzmann factors. At 50 K (continuous line) the system is macroscopically LS ($n_{HS} \sim 0.03$) and the oscillator is localized around the equilibrium position of the pure LS state. With increasing temperature, the HS vibronic levels become populated and the system delocalizes. For $T_{1/2} = 128\ K$ (dashed line) the thermal density of probability is completely delocalized in the q-space. When the spin conversion is almost complete, as for $T = 300\ K$ ($n_{HS} \sim 0.85$, dotted line), the system is mainly localized at the equilibrium position of a HS state.

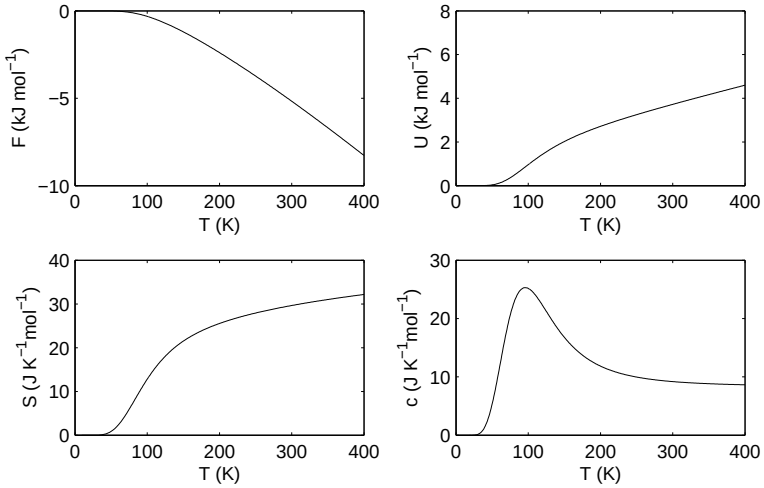

Figure 3.12: Temperature dependence of Helmholtz free energy F, internal energy U, entropy S and heat capacity C, calculated for the parameters in table 3.1, $J = 5\ meV$ and $g = 15$.

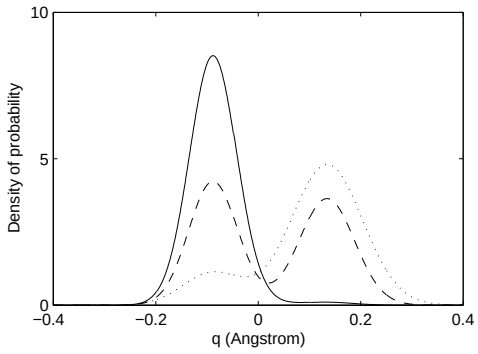

Figure 3.13: Thermal densities of probability along the vibrational coordinate q, calculated for the parameters in table 3.1, $J = 5\ meV$ and $g = 15$ at $T = 50\ K$ (continuous line), $T = T_{1/2} = 128\ K$ (dashed line) and $T = 300\ K$ (dotted line).

3.3 Intermolecular interactions and cooperativity

3.3.1 Phenomenological model for intermolecular interactions

The simple and general model for SC molecules presented in section 3.2.1, is now adopted to describe interacting SC complexes. Cooperativity in SC systems results from elastic interactions, due to the large changes of molecular geometries that accompany the change of spin state. The molecular Hamiltonian in equation (3.6), represents a reliable starting point for the development of a model for interacting systems. A microscopic description of the coupling between spin state, mv and lattice phonons is needed to shed light on the origin of interactions. However the development of a vibronic model for SC crystals goes beyond the scopes of this work. Here we shortly address a phenomenological treatment of intermolecular interactions.

The molecular Hamiltonian in equation (3.6) is defined in terms of two operators, $\hat{\sigma}_g$ (hereafter replaced by $\hat{\sigma}$), characterizing the spin state, and $\hat{q}$, measuring the molecular distortion. In this work spin-spin and distortion-distortion interactions between nearest neighboring SC units are considered. The crystal Hamiltonian is

$$H = \sum_i \hat{h}_i - J^\sigma \sum_{\langle i,j \rangle} \hat{\sigma}_i \hat{\sigma}_j - J^q \sum_{\langle i,j \rangle} \hat{q}_i \hat{q}_j \tag{3.36}$$

where $\hat{h}_i$ is the Hamiltonian of the i-th molecule, defined in equation (3.6), and J^σ (J^q) is the spin-spin (distortion-distortion) interaction term.

Hamiltonian (3.36) is solved within the mean field (mf) approximation. The mf Hamiltonian reads

$$H_{MF} = \sum_i \left(\hat{h}_i - z J^\sigma \langle \sigma \rangle \ \hat{\sigma}_i - z J^q \langle q \rangle \ \hat{q}_i \right) + \frac{Nz}{2} \left(J^\sigma \langle \sigma \rangle^2 + J^q \langle q \rangle^2 \right) \tag{3.37}$$

where z is the number of nearest neighbors and $\langle \sigma \rangle$ and $\langle q \rangle$ are the thermal averages of spin state and molecular distortion. The macroscopic spin state is again expressed in term of the HS fraction $n_{HS} = (\langle \sigma \rangle + 1)/2$.

3.3.2 Interactions between SC molecules: results

The mf Hamiltonian in equation (3.37), self consistently depends on two order parameters $\langle\sigma\rangle$ (or equivalently n_{HS}) and $\langle q\rangle$. Self consistency is achieved by minimizing the difference between input (entering the Hamiltonian (3.37)) and output (obtained after diagonalization) values of the order parameters. The minimization is performed using a Newton optimization algorithm for functions of two variables. Imposing self consistency corresponds to localize the minima of the free energy function $F(n_{HS}, \langle q\rangle)$. Results reported in the following are referred to molecular parameters in table 3.1, $J = 5\ meV$, $g = 15$ and $z = 6$ nearest neighbors.

We consider first the case of spin-spin interaction ($J^q = 0$ in Hamiltonian (3.37)), so that the only relevant order parameter is n_{HS}. Figure 3.14 shows the T-dependence of the n_{HS} and $\langle q\rangle$ for different strength of the spin-spin interactions. Upon increasing J^σ, the transition curves $n_{HS}(T)$ (left panel) becomes steeper and steeper (c.f. black and red lines, calculated for $J^\sigma = 0$ and $J^\sigma = 1\ meV$, respectively). The increase of J^σ does not affect the equilibrium temperature $T_{1/2} = 128\ K$ and all the continuous $n_{HS}(T)$ curves cross at $T_{1/2}$. For $J^\sigma > J^\sigma_{cr} \approx 1.9\ meV$ the crossover becomes discontinuous. For $J^\sigma = 2.5\ meV$, within the temperature interval 102-136 K, the mf Hamiltonian has two stable solutions, corresponding to LS and HS phases. Molecular distortion $\langle q\rangle$ (right panel of figure 3.14) follows the change in the spin state, both in gradual and in abrupt crossovers.

The free energy dependence on n_{HS} is shown in figure 3.15. The left panel refers to a system with weak interactions ($J^\sigma = 1\ meV$), showing a gradual SC. In this case the single minimum of the free energy (corresponding to the solution of mf Hamiltonian (3.37)), moves from $n_{HS} = 0$ toward 1 with increasing temperature, describing the LS to HS conversion. For a discontinuous transition ($J^\sigma = 2.5\ meV$), as shown in the right panel of figure 3.15, for T values within the bistability region, F shows two minima,

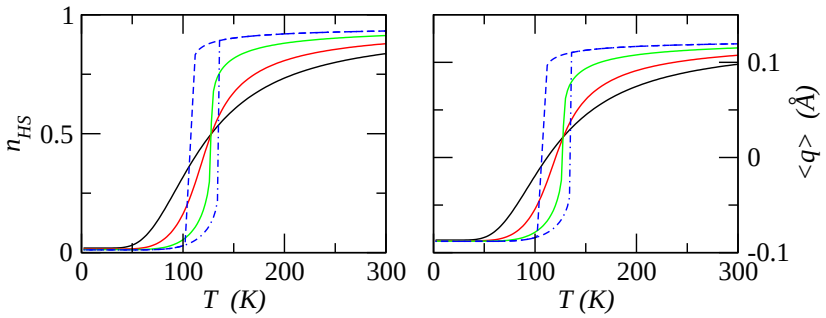

Figure 3.14: T-dependence of n_{HS} and $\langle q \rangle$ for a non-interacting system ($J^\sigma = 0$, black line) and interacting systems with $J^\sigma = 1\ meV$ (red curve), $J^\sigma = 1.9\ meV \approx J^\sigma_{cr}$ (green line) and $J^\sigma = 2.5\ meV$ on cooling (blue dashed line) and on heating (blue dot-dashed line). $J^q = 0$ for all calculations.

corresponding to two stable solutions of Hamiltonian (3.37).

Figure 3.16 shows the energies (upper panels) and the expectation values of $\hat{\sigma}$ (lower panels) of the four lowest energy vibronic levels. For clarity the quantities referred to the $\{|LS\rangle, |HS_0^*\rangle\}$ subspace are plotted in black, while quantities associated with the uncoupled HS states in red (each red curve refers to $g-1$ identical states). The case of a continuous crossover ($J^\sigma = 1.5\ meV$, c.f. red transition curve in the left panel of figure 3.14) is reported in the left column of figure 3.16. The increase of the HS fraction with temperature lowers the energy difference between HS and LS levels. As for the $\{|LS\rangle, |HS_0^*\rangle\}$ subspace, this change of the energy levels causes significant variations in the composition of the states ($|LS\rangle$-$|HS_0^*\rangle$ mixing), as can be observed from the corresponding σ_i values (black lines in left bottom panel). The ground state (marked with **1**) remain a largely LS state ($\sigma_1 \approx -1$) even at high temperatures, while the states **2** and **3** are strongly mixed. The presence of a LS ground state in a macroscopic HS state, is a natural consequence of the higher degeneracy of the HS state. This feature persists also in the discontinuous crossover, as for the case $J^\sigma = 2.5\ meV$,

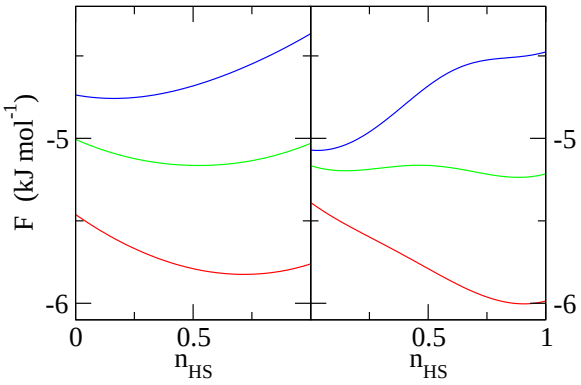

Figure 3.15: Free energy profiles calculated for $J^\sigma = 1\ meV$ (left panel) and $J^\sigma = 2.5\ meV$ (right panel) at $T = 100$, 130 and 160 K (blue, green and red lines respectively). $J^q = 0$ for all calculations.

considered in the middle panels of figure 3.16. T-dependence of E_i and σ_i (top and bottom panels respectively) refer to the heating curve (c.f. dot-dashed transition curve in the left panel of figure 3.14). The discontinuity in the $n_{HS}(T)$ curve at $T = 128\ K$ results in an abrupt change in the vibronic levels. However, also in the HS phase, the quantomechanic ground state (**1**) remains an almost LS state. For stronger interaction, as for $J^\sigma = 4\ meV$ (right panels of figure 3.16), the abrupt change of the vibronic energy levels causes the switch to a HS ground state.

In the presence of only distortion-distortion interactions ($J^\sigma = 0$), Hamiltonian (3.37) self-consistently depends on the order parameter $\langle q \rangle$. In figure 3.17 are shown the thermal evolution of the equilibrium n_{HS} and $\langle q \rangle$, in left and right panels respectively. The results are very similar to the previous case: distortion-distortion interactions induce a LS-HS transition accompanied by an increase of molecular distortion. With the increase of J^q the LS-HS transition becomes steeper and for $J^q > J^q_{cr} \approx 118\ meV$ an hysteresis loop appears. The dependence of the free energy on the order parameter

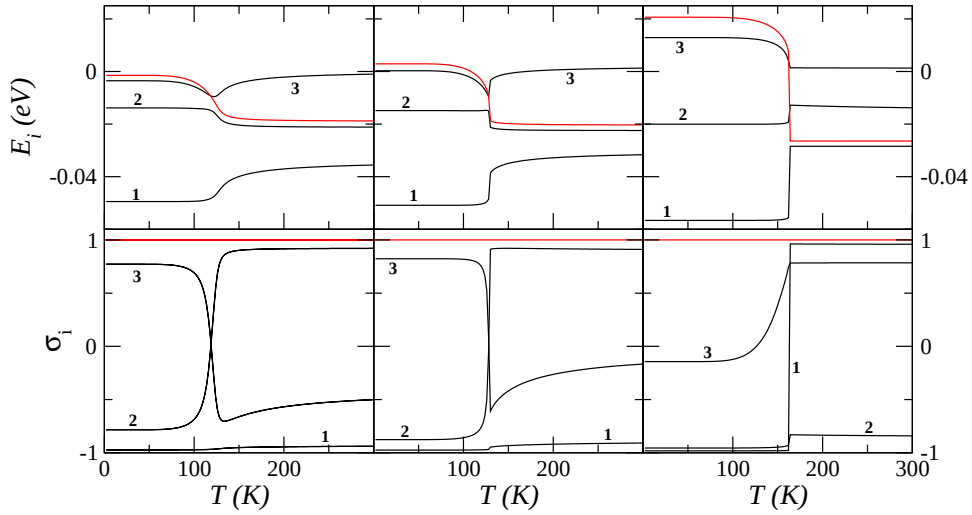

Figure 3.16: T-dependence of lowest energy levels (upper panels) and of the respective expectation value of σ_i (lower panels) calculated for $J^\sigma = 1\ meV$ (left panels), $J^\sigma = 2.5\ meV$ on heating (central panels) and $J^\sigma = 4\ meV$ on heating (right panels). Black lines refer to levels of the $\{|LS\rangle, |HS_0^*\rangle\}$ subspace, red lines to levels from HS subspace. $J^q = 0$ for all calculations.

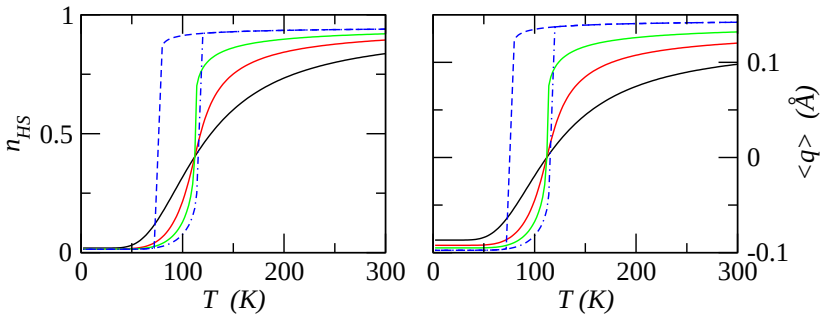

Figure 3.17: Temperature dependence of n_{HS} and $\langle q \rangle$ calculated for $J^q = 0$ (black line), $J^q = 80\ meV$ (red line), $J^q = J^q_{cr} = 118\ meV$ (green line) and $J^q = 150\ meV$ on cooling (blue dashed line) and on heating (blue dot-dashed line). $J^\sigma = 0$ for all calculations.

$\langle q \rangle$ is shown in figure 3.18, for a continuous ($J^q = 80\ meV$) and a discontinuous crossover ($J^q = 150\ meV$), in left and right panels respectively. The F behavior is, *mutatis mutandis*, analogous that obtained in the case spin-spin interactions (c.f. figure 3.15). Spin-spin and distortion-distortion interaction terms are responsible for extremely similar effects. This similarity is due to the e-mv coupling in the molecular Hamiltonian (3.6), that assumes different equilibrium geometries for LS and HS states.

We now consider Hamiltonian (3.37) in its general form ($J^\sigma \neq 0$ and $J^q \neq 0$). In this case the Hamiltonian self-consistently depends on the two order parameters n_{HS} and $\langle q \rangle$. Figure 3.19 shows the dependence of n_{HS} and $\langle q \rangle$ with temperature. Results are analogous to those observed when single interactions are introduced separately (c.f. figures 3.14 and 3.17). An approximately additive effect of the two interactions is observed.

In figure 3.20 are shown the contour plot of the free energy versus the two order parameters n_{HS} and $\langle q \rangle$. The free energy in the case of a continuous crossover ($J^\sigma = 1\ meV$, $J^q = 50\ meV$, red transition curve in figure 3.19) is plotted in the upper panels with increasing temperature from left to right.

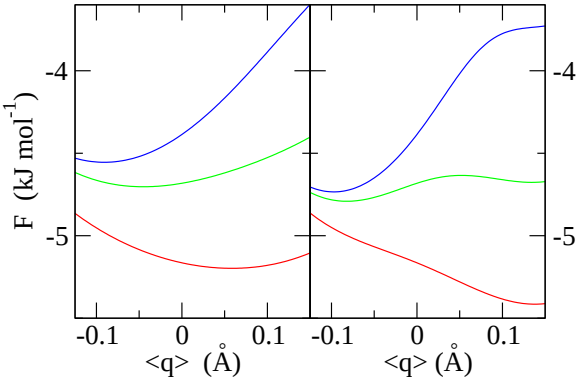

Figure 3.18: Free energy profiles calculated for $J^q = 80\ meV$ (left panel) and $J^q = 150\ meV$ (right panel) at $T = 60$, 100 and 130 K (blue, green and red lines respectively). $J^\sigma = 0$ for all calculations.

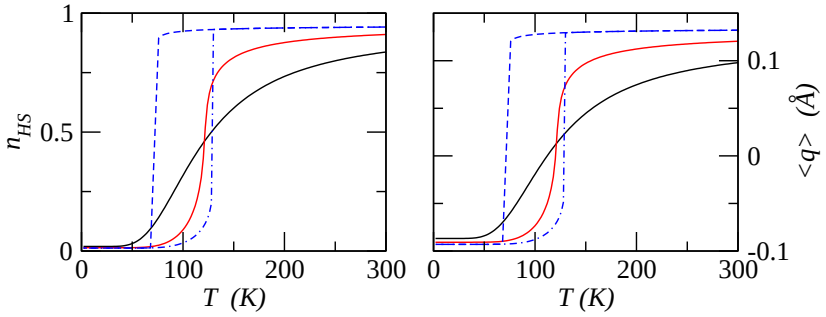

Figure 3.19: Temperature dependence of n_{HS} and of $\langle q \rangle$ calculated for a non-interacting ($J^\sigma = J^q = 0$, black line), a weakly interacting ($J^\sigma = 1\ meV$, $J^q = 50\ meV$, red line) and a strongly interacting ($J^\sigma = 15\ meV$, $J^q = 80\ meV$, blue dashed and dot-dashed line on cooling and on heating respectively) system.

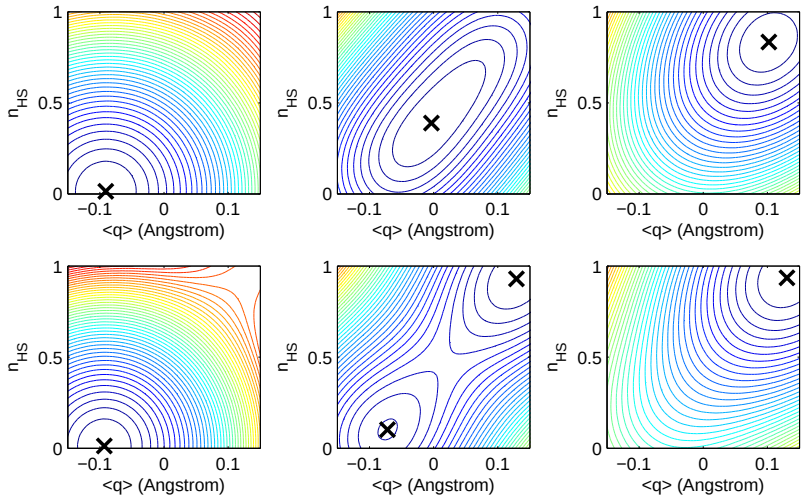

Figure 3.20: Free energy contour plots calculated for a weakly-interacting system ($J^\sigma = 1\ meV$, $J^q = 50\ meV$, upper panels) and a strongly-interacting system ($J^\sigma = 1.5\ meV$, $J^q = 80\ meV$, lower panels) at $T = 50$, 120 and 160 K (left, central and right columns respectively). Equilibrium positions (minima) of $F(\langle q \rangle, n_{HS})$ are marked with black crosses.

In this case F always presents a single minimum (marked with a cross) that moves gradually from a macroscopic LS state to a macroscopic HS state upon increasing T. The free energy surfaces for a discontinuous transition ($J^\sigma = 15\ meV$, $J^q = 80\ meV$, blue lines in figure 3.19) are plotted in the bottom panels of figure 3.20. In this case for temperatures outside the bistability region (hysteresis loop) F presents a single minimum, corresponding to a LS phase (left bottom panel) at low temperature and to a HS phase at high temperature (right bottom panel). Within the bistability region F presents two minima, corresponding to a LS and a HS phase (middle bottom panel).

3.4 Discussion and Conclusions

In this chapter we presented a simple microscopic model, that describes the basics physics of SC molecules. The model describes a LS state and g degenerate HS states, as relevant for a d^6 configuration, coupled to a vibrational coordinate, corresponding to the breathing mode of the ligand cage. Linear (Holstein) and quadratic e-mv coupling is considered to account for the different equilibrium geometries and vibrational frequencies in the LS and HS states. The effect of the mixing between LS and HS states, due to higher order spin-orbit coupling, is introduced with an off-diagonal matrix element J. Although the thermal properties cannot be quantitatively reproduced by our model, because of the single vibrational mode approximation, it provides a reliable description of the quantomechanics of SC molecule.

Our approach, based on a rigorous distinction between electronic (spin state) and vibrational (molecular distortion) degrees of freedom, represents the first study of e-mv coupling in SC complexes beyond the adiabatic approximation. The comparison with adiabatic results demonstrates that, apart from the two unrealistic limits of uncoupled oscillators ($J = 0$) and of very large J, the adiabatic approximation fails. This result is not surprising since in SC complexes the electronic energies are comparable with vibrational frequencies and raises the issue of the applicability to SC problems of quantum chemical electronic structure calculations.

The model for SC molecules sets a solid basis for the development of models for interacting system. In this chapter we consider intermolecular interactions between spin states and molecular distortions. As well established from the study of the Ising-like model, ferromagnetic-like interactions between fictitious spins create macroscopic barriers between LS and HS phases, leading to bistability. Analogous effects are obtained considering the interaction between molecular distortions. The development of a

microscopic model for elastic intermolecular interactions, that explicitly introduces lattice vibrations represents an interesting further development of the present work.

Conclusions and Perspectives

Molecular materials for advanced applications combine interesting functionalities with the versatility of chemical synthesis and the processability and low-cost and of organic materials. To fully exploit the potential offered by functional molecular materials, the understanding of molecular properties is, however, not enough. In fact, intermolecular interactions in condensed phases can profoundly alter molecular properties and, in some cases, are responsible for the emergence of brand new phenomena, not supported at the molecular level. Emergent phenomena are typically cooperative in nature, phase transitions and multistability being the most representative examples. A deep understanding of cooperativity or, more generally, of non-additive and non-linear behavior in molecular materials, is therefore a basic requirement for the optimization of materials properties.

The research work described in this thesis represents a contribution to the understanding of cooperative phenomena in switchable molecular materials due to the complex interplay between charge and/or spin degrees of freedom, phonons (including molecular and lattice vibrations) and/or electrostatic interactions. Our contribution is mainly in the development and exploitation of general microscopic models to describe the essential physics governing functional molecular materials. The investigated systems include mixed stack charge transfer (CT) crystals, crystals of valence tautomeric molecules and spin crossover (SC) complexes.

In mixed stack CT crystals electron-donor (D) and acceptor (A) molecules pack face to face forming stacks, leading to delocalized electrons in one-dimension. In these intrinsically cooperative systems, electrostatic interactions, molecular vibrations and lattice phonons drive the neutral-ionic phase transition (NIT), a collective electron transfer from D to A molecules, always accompanied by lattice dimerization. NIT is the subject of active research since decades [26] and in recent years the field attracted renewed attention. NIT in fact offers an intriguing example of a quantum phase transition, [25] leading to ferroelectric [2] and potentially multiferroic states. [21]

A coherent picture of the rich and complex phenomenology of NIT is emerging, based on a modified Hubbard model accounting for Peierls coupling to lattice phonons and Holstein coupling to molecular vibrations. Indeed, most of the intriguing phenomenology of mixed stack CT crystals can be quantitatively explained in terms of an amplified response of the electronic system in the proximity of NIT, due to electron-phonon coupling. In this thesis we modeled the dispersion of lattice phonons in mixed stack CT crystals and proved that a Kohn-like anomaly develops in the optical phonon branch at NIT. This anomaly quantitatively explains the sharp diffuse X-ray profiles experimentally observed in the pretrantional regime in TTF-CA and DMTTF-CA crystals. [59, 58] Moreover, an original implementation of the time correlation function approach to spectroscopy, based on the modern theory of polarization and polarizability in insulators, allowed us to calculate infrared and Raman spectra of mixed stack systems without invoking the harmonic approximation. The results confirm the current interpretation of experimental data, including the softening of coupled modes, and the increase of IR intensity of the Peierls mode upon approaching NIT. More interestingly, this approach fully rationalizes more subtle phenomena governed by anharmonicity, as the appearance in the IR spectra of bands due to combinations of molecular and lattice modes and the enhancement of the

low frequency Raman signal in the close proximity of NIT, recently observed in the guest laboratory.

Crystals of valence tautomeric DA molecules share some basic physics with mixed-stack CT crystals, with the difference that D and A sites now correspond to chemical groups located on the same molecule. Electrons are now strictly confined on each molecular unit, but delocalized between the D and the A group. The Hamiltonian of a crystal of DA molecules corresponds the $\delta = 1$ limit of the modified Hubbard Hamiltonian for mixed stack CT crystals. The charge instability in crystals of DA molecules and the related phenomenon of bistability were theoretically predicted a few years ago in the guest laboratory. [20, 82] In this thesis we demonstrate that the proposed mechanism for bistability quantitatively explains the temperature dependent valence tautomerism observed in Fc-PTM crystals. [79] Following a bottom up modeling procedure, [83] the basic physics of interacting DA molecules is described adopting a two state model for the molecular units, that is reliably parametrized for the specific compound at hand from a detailed analysis of its solution spectra. A reliable description of intermolecular electrostatic interactions is obtained with the support of quantum chemical calculations. Moreover, the development of a three-state model for DA molecules, that explicitly accounts for an active role of the π-bridge in the CT, allowed us to solve a long-standing problem in the field of optical spectroscopy, and, at the same time, demonstrates the robustness of our model for bistability.

The final part of this thesis is devoted to SC complexes, one of the most striking examples of bistable molecular material. [14] Cooperativity in SC has an elastic origin and results from the interplay between the molecular spins and intramolecular and intermolecular vibrational degrees of freedom. In this thesis we develop a vibronic model for SC molecules, that accounts for the coupling between the molecular spin and an effective molecular vibration in a non-adiabatic picture. The model is simple but describes the basic

physics of SC. In particular it accounts for the different equilibrium geometries and vibrational frequencies of the two spin states, and for the mixing of LS and HS states provided by spin-orbit coupling. The comparison between exact and adiabatic results demonstrates that in SC molecules, as expected in systems where electronic energies are comparable with vibrational frequencies, the adiabatic approximation fails. This result raises the issue of the reliability of standard quantum chemical calculations for SC complexes. Preliminary results on cooperative effects of intermolecular interactions in SC crystals demonstrate the possibility to describe cooperative phenomena, while fully accounting for the non-adiabatic coupling of molecular vibrations to spin degrees of freedom.

The theoretical study of multistability in different families of molecular materials, adopting different models and techniques, leads to a thorough understanding of the highly nontrivial physics underlying cooperativity in these systems. Contrasting and comparing the behavior of the different classes of materials allows to identify unifying features as well as more specific characteristics. The charge instabilities in mixed stack CT crystals and in crystals of valence tautomeric molecules are quantum phase transitions, where temperature plays only a marginal role, because excited states are not thermally relevant. In these systems, strong intermolecular interactions not only lead to multistability, but are also required to stabilize states with different charge distributions. In SC systems, instead, the low energy of spin excitations and the large degeneracy of high spin states, make SC a true thermal process that does not require intermolecular interactions. Weak intermolecular interactions are enough to create kinetic barriers between stable phases, leading to bistability.

To conclude with, we remark the interplay between charge and/or spin degrees of freedom, electrostatic interactions, molecular vibrations and lattice phonons is a primary source of cooperativity in molecular materials.

With particular focus on mixed stack CT crystals, crystals of DA molecules and SC complexes, we demonstrate that simple microscopic models are able to catch and quantitatively describe complex cooperative phenomena. The models we propose are simple and general enough to provide deep insight in the physical origin of the material properties. In this respect, this work can be extended in several directions. The original approach developed for the calculation of vibrational spectra of CT crystals can prove extremely useful if applied to other systems where the interaction between electronic and vibrational degrees of freedom drives the systems towards instabilities: charge ordering and ferroelectric phase transitions are of course the immediate target. The model for crystals of DA molecules yields to simple guidelines for the search of bistable systems: we really hope that our results will trigger some work in this direction, while additional measurements on the system at hand can deepen our understanding of this fascinating phenomenon. Our work on SC systems provides a first detailed description of the coupling between spin and molecular vibrations, opening the way to new families of models where subtle phenomena, including relaxation dynamics, can find a microscopic description.

Bibliography

[1] S. Forrest, Nature **428** (2004)

[2] S. Horiuchi and Y. Tokura, Nature Materials **7**, 3567 (2008)

[3] G. Malliaras and R. Friend, Phys. Today **5** (2005)

[4] A. J. Heeger, S. Kivelson, J. R. Schrieffer, and W. P. Su, Rev. Mod. Phys. **60**, 781 (1988)

[5] M. Muccini, Nature Materials **5**, 605 (2006)

[6] J. R. Health and M. Ratner, Phys. Today **5** (2003)

[7] S. R. Marder, B. Kippelen, A. K.-J. Jen, and N. Peyghambarian, Nature **388** (1997)

[8] E. Collet, M. H. Lemée-Cailleau, M. Buron-Le Cointe, H. Cailleau, M. Wulff, T. Luty, S.-Y. Koshihara, M. Meyer, L. Toupet, P. Rabiller, and S. Techert, Science **300**, 612 (2003)

[9] S. Decurtins, P. Gütlich, C. P. Köhler, H. Spiering, and A. Hauser, Chem. Phys. Lett. **105**, 1 (1984)

[10] P. Gütlich, Y. Garcia, and T. Woike, Coord. Chem. Rev. **219**, 839 (2001)

[11] A. Dei, D. Gatteschi, C. Sangregorio, and L. Sorace, Acc. Chem. Res. **37**, 827 (2004)

[12] O. Sato, J. Tao, and Y. Z. Zhang, Angew. Chem. Int. Ed. **46**, 2152 (2007)

[13] A. Hauser, J. Jeftić, H. Romstedt, R. Hinek, and H. Spiering, Coord. Chem. Rev. **190**, 471 (1999)

[14] P. Gütlich and H. A. Goodwin, Top. Curr. Chem. **233**, 1 (2004)

[15] R. M. Metzger, Chem. Rev. **103**, 3803 (2003)

[16] O. Kahn, C. Jay, and C. Martinez, Science **279** (1998)

[17] M. Tlidi, P. Mandel, and R. Lefever, Phys. Rev. Lett. **73**, 640 (1994)

[18] P. Gutlich and A. Dei, Angew. Chem. Int. Ed. **36**, 273 (1997)

[19] A. Caneschi, A. Cornia, and A. Dei, Inorg. Chem. **37**, 3419 (1998)

[20] F. Terenziani and A. Painelli, Phys. Rev. B **68**, 165405 (2003)

[21] G. Giovannetti, S. Kumar, A. Stroppa, J. van den Brink, and S. Picozzi, Phys. Rev. Lett. **103**, 266401 (2009)

[22] Z. G. Soos and D. J. Klein, in *Treatize on Solid State Chemistry*, Vol. III (Plenum Press, New York, 1976) p. 689

[23] A. Girlando, A. Painelli, S. A. Bewick, and Z. G. Soos, Synth. Metals **141**, 129 (2004)

[24] H. M. McConnel, B. M. Hoffman, and R. M. Metzger, Proc. Natl. Acad. Sci. U.S.A. **53**, 46 (1965)

[25] S. Horiuchi, Y. Okimoto, R. Kumai, and Y. Tokura, Science **299**, 229 (2003)

[26] J. B. Torrance, J. E. Vazquez, J. J. Mayerle, and V. Y. Lee, Phys. Rev. Lett. **46**, 253 (1981)

[27] J. B. Torrance, A. Girlando, J. J. Mayerle, J. I. Crowley, V. Y. Lee, P. Batail, and S. J. LaPlaca, Phys. Rev. Lett. **47**, 1747 (1981)

[28] P. Ranzieri, M. Masino, A. Girlando, and M. H. Lemée-Cailleau, Phys. Rev. B **76**, 134115 (2007)

[29] P. J. Strebel and Z. G. Soos, J. Chem Phys. **53**, 4077 (1970)

[30] N. Nagaosa and J.-I. Takimoto, J. Phys. Soc. Jp. **55**, 2735 (1986)

[31] N. Nagaosa and J.-I. Takimoto, J. Phys. Soc. Jp. **55**, 2745 (1986)

[32] A. Girlando and A. Painelli, Phys. Rev. B **34**, 2131 (1986)

[33] A. Painelli and A. Girlando, Phys. Rev. B **37**, 5748 (1988)

[34] A. Painelli and A. Girlando, Phys. Rev. B **45**, 8913 (1992)

[35] H. Katsura, M. Sato, and N. Nagaosa, Phys. Rev. Lett. **103**, 177402 (2009)

[36] Y. Anusooya-Pati, Z. G. Soos, and A. Painelli, Phys. Rev. B **63**, 205118 (2001)

[37] Z. G. Soos and A. Painelli, Phys. Rev. B **75**, 155119 (2007)

[38] Z. G. Soos, S. Bewick, A. Peri, and A. Painelli, J. Chem. Phys. **120**, 6712 (2004)

[39] M. J. Rice and E. J. Mele, Phys. Rev. Lett. **49**, 1455 (1982)

[40] A. Painelli, L. D. Freo, and Z. G. Soos, Synth. Metals **133-134**, 619 (2003)

[41] Z. G. Soos and S. Ramasesha, in *Valence Bond Theory and Chemical Structure* (Elsevier, Amsterdam, 1989) p. 81

[42] S. Ramasesha and Z. G. Soos, in *Theoretical and Computational Chemistry*, Vol. 10, edited by D. L. Cooper (Elsevier, Amsterdam, 2002) p. 635

[43] S. Rettrup, J. Comp. Phys. **45**, 100 (1982)

[44] R. Resta, Phys. Rev. Lett. **80**, 1800 (1998)

[45] R. W. Nunes and X. Gonze, Phys. Rev. B **63**, 155107 (2001)

[46] L. D. Freo, A. Painelli, and Z. G. Soos, Phys. Rev. Lett. **89**, 027402 (2002)

[47] W. H. Press, B. P. Flannery, S. A. Teukolsky, and W. T. Vetterling, *Numerical Recipes in Fortran 77* (Cambridge University Press, Cambridge, 1986)

[48] A. Painelli and A. Girlando, J. Chem. Phys. **87**, 1705 (1987)

[49] A. Girlando, A. Painelli, C. Pecile, G. Calestani, C. Rizzoli, and R. M. Metzger, The Journal of Chemical Physics **98**, 7692 (1993)

[50] K. Takaoka, Y. Kaneko, H. Okamoto, Y. Tokura, T. Koda, T. Mitani, and G. Saito, Phys. Rev. B **36**, 3884 (1987)

[51] M. Masino, A. Girlando, A. Brillante, R. G. Dalla Valle, and E. Venuti, Mater. Sci. Poland **22**, 333 (2004)

[52] A. Girlando, F. Marzola, C. Pecile, and J. B. Torrance, J. Chem. Phys. **79**, 1075 (1983)

[53] S. Horiuchi, Y. Okimoto, R. Kumai, and Y. Tokura, J. Soc. Phys. Jpn. **69**, 1302 (2000)

[54] S. Horiuchi, Y. Okimoto, R. Kumai, and Y. Tokura, J. Am. Chem. Soc. **123**, 665 (2001)

[55] M. Masino, A. Girlando, and Z. G. Soos, Chem Phys. Lett. **369**, 428 (2003)

[56] E. Collet, M. H. Lemée-Cailleau, M. Buron-Le Cointe, S. Ravy, T., J. F. Bérar, P. Czarnecki, and N. Karl, Europhys. Lett. **57**, 67 (2002)

[57] M. Masino and A. Girlando, private communication

[58] M. Buron-Le Cointe, M. H. Lemée-Cailleau, H. Cailleau, B. Toudic, L. Troupet, G. Heger, F. Moussa, P. Schweiss, K. H. Kraft, and N. Karl, Europhys. Lett. **57**, 67 (2002)

[59] M. Buron-Le Cointe, M. H. Lemée-Cailleau, S. Ravy, J. F. Bérar, S. Rouzière, E. Elkaim, and E. Collet, Phys. Rev. Lett. **96**, 205503 (2006)

[60] T. Mitani, Y. Kaneko, Y. Tanuma, S. Tokura, T. Koda, and G. Saito, Phys. Rev. B **35**, 427 (1987)

[61] N. Nagaosa, J. Phys. Soc. Jp. **55**, 2754 (1986)

[62] Y. Okimoto, S. Horiuchi, E. Saitoh, R. Kumai, and Y. Tokura, Phys. Rev. Lett. **87**, 187401 (2001)

[63] A. Girlando, M. Masino, A. Painelli, N. Drichko, M. Dressel, A. Brillante, R. G. Della Valle, and E. Venuti, Phys. Rev. B **78** (2008)

[64] R. G. Gordon, Advances in Magnetic Resonance **3**, 1 (1968)

[65] M.-P. Gaigeot and M. Sprik, J. Chem. Phys. **107**, 10344 (2003)

[66] R. Car and M. Parrinello, Phys. Rev. Lett. **55**, 2471 (1985)

[67] M. Bernasconi, P. L. Silvestrelli, and M. Parrinello, Phys. Rev. Lett. **81**, 1235 (1998)

[68] A. Putrino and M. Parrinello, Phys. Rev. Lett. **88**, 176401 (2002)

[69] M. Pagliai, C. Cavazzoni, G. Cardini, G. Erbacci, M. Parrinello, and V. Schettino, J. Chem. Phys. **128**, 224514 (2008)

[70] L. Verlet, Phys. Rev. **159**, 98 (1967)

[71] D. Chandler, *Introduction to Modern Statistical Mechanics* (Oxford University Press, New York, 1987)

[72] S. Nosé, J. Chem. Phys. **81**, 511 (1984)

[73] W. G. Hoover, Phys. Rev. A **31**, 1695 (1985)

[74] S. Ravy, Chem. Rev. **104**, 5609 (2004)

[75] J. P. Pouget, in *Semiconductors and semimetals*, edited by E. M. Conwell (Academic Press, 1988) p. 88

[76] N. W. Ashcroft and N. D. Mermin, *Solid State Physics* (Holt-Saunders International Editions, 1976)

[77] S. N. Dixit and S. Mazumdar, Phys. Rev. B **29**, 1824 (1984)

[78] I. Ratera, C. Sporer, D. Ruiz-Molina, N. Ventosa, J. Baggerman, A. Brouwer, C. Rovira, and J. Veciana, J. Am. Chem. Soc. **129**, 6117 (2007)

[79] I. Ratera, D. Ruiz-Molina, F. Renz, J. Ensling, K. Wurst, C. Rovira, P. Gütlich, and J. Veciana, J. Am. Chem. Soc. **125**, 1462 (2003)

[80] O. Elsner, D. Ruiz-Molina, J. Vidal-Gancedo, C. Rovira, and J. Veciana, Chem. Comm. **7**, 579 (1999)

[81] N. N. Greenwood and T. C. Gibb, *Mössbauer Spectroscopy* (Chapman and Hall Ltd., London, 1971)

[82] A. Painelli and F. Terenziani, J. Am. Chem. Soc. **125**, 5624 (2003)

[83] F. Terenziani, G. D'Avino, and A. Painelli, ChemPhysChem **8**, 2433 (2007)

[84] F. Terenziani, A. Painelli, C. Katan, M. Charlot, and M. Blanchard-Desce, J. Am. Chem. Soc. **128**, 15742 (2006)

[85] F. Terenziani, C. Sissa, and A. Painelli, J. Phys. Chem. B **112**, 5079 (2008)

[86] F. Terenziani, A. Painelli, A. Girlando, and M. R. M., J. Phys. Chem. B **108**, 10743 (2004)

[87] A. Painelli, F. Terenziani, L. Angiolini, T. Benelli, and L. Giorgini, Chem. Eur. J. **11**, 6053 (2005)

[88] A. Painelli and F. Terenziani, in *Nonlinear optical properties of matter: from molecules to condensed phases*, edited by M. G. Papadopulos, A. J. Sadlej, and J. Leszczynski (Springer, 2006) p. 251

[89] F. Terenziani, A. Painelli, C. Katan, M. Charlot, and M. Blanchard-Desce, J. Am. Chem. Soc. **128**, 15742 (2006)

[90] G. D'Avino, F. Terenziani, and A. Painelli, J. Phys. Chem. B **110**, 25590 (2006)

[91] A. Painelli, Chem. Phys. Lett. **285**, 352 (1998)

[92] A. Painelli, Chem. Phys. **245**, 185 (1999)

[93] A. Painelli and F. Terenziani, J.Phys. Chem. A **104**, 11041 (2000)

[94] B. Boldrini, E. Cavalli, A. Painelli, and F. Terenziani, J. Phys. Chem. A **106**, 6286 (2002)

[95] R. S. Mulliken, J. Am. Chem. Soc. **74**, 811 (1952)

[96] A. Painelli and F. Terenziani, Chem. Phys. Lett. **312**, 211 (1999)

[97] L. Del Freo and A. Painelli, Chem. Phys. Lett. **338**, 208 (2001)

[98] R. A. Marcus, Rev. Mod. Phys. **65**, 599 (1993)

[99] N. S. Hush, Prog. Inorg. Chem. **64**, 135 (1985)

[100] N. S. Hush and J. R. Reimers, Chem. Rev **100**, 775 (2000)

[101] M. Bixon and J. Jortner, Adv. Chem. Phys. **106**, 35 (1999)

[102] R. J. Cave and M. D. Newton, Chem. Phys. Lett. **249**, 15 (1996)

[103] S. F. Nelsen and M. D. Newton, J. Chem. Phys. A **104**, 10023 (2000)

[104] L.-T. Zhang and M. J. Ondrechen, Inorg. Chem Acta **226**, 43 (1994)

[105] V. Coropceanu, J. M. Andre, M. Malagoli, and J. L. Bredas, Theor. Chem. Acc. **110**, 59 (2003)

[106] V. Coropceanu, N. E. Gruhn, S. Barlow, C. Lambert, J. C. Durivage, T. G. Bill, G. Noll, S. R. Marder, and J.-L. Bredas, J. Am. Chem. Soc. **126**, 2727 (2004)

[107] E. V. Tsiper and Z. G. Soos, Phys. Rev. B **64**, 195124 (2001)

[108] J. P. Stewart, J. Mol. Model. **13**, 1173 (2007)

[109] C. Reichardt, Chem. Rev. **94**, 2319 (1994)

[110] Y. A. Berlin, F. C. Grozema, L. D. A. Siebbeles, and M. A. Ratner, J. Phys. Chem. C **112**, 10988 (2008)

[111] M. Tanaka, Bull. Chem. Soc. Jpn. **50**, 2881 (1977)

[112] C. S. Jacobsen and J. B. Torrance, J. Chem. Phys. **78**, 112 (1983)

[113] K. Yakushi and H. Kuroda, Chem. Phys. Lett. **111**, 165 (1984)

[114] A. Painelli and A. Girlando, J. Chem. Phys. **84**, 5655 (1986)

[115] M. Kondo, M. Uchikawa, K. Namiki, W.-W. Zhang, S. Kume, E. Nishibori, H. Suwa, S. Aoyagi, M. Sakata, M. Murata, Y. Kobayashi, and H. Nishihara, J. Am. Chem. Soc. **131**, 12112 (2009)

[116] L. Cambi, L. Szego, and A. Cagnasso, Atti Accad. Lincei **13**, 168 (1936)

[117] A. Hauser, Top. Curr. Chem. **233**, 49 (2004)

[118] A. H. Ewald, R. L. Martin, and W. A. H., Proc. Roy. Soc. A **280**, 235 (1964)

[119] J. A. Nasser, S. Topçu, L. Chassagne, A. Bousseksou, T. Guillon, and Y. Alayli, Chem. Phys. Lett. **446**, 385 (2007)

[120] J.-P. Tuchagues, A. Bousseksou, G. Molnár, and J. J. McGarvey, Top. Curr. Chem. **235**, 85 (2004)

[121] M. A. Hoselton, L. J. Wilson, and R. S. Drago, J. Am. Chem. Soc. **97**, 1722 (1975)

[122] B. A. Katz and C. E. Strouse, J. Am. Chem. Soc. **101**, 6214 (1979)

[123] J. F. Letard, P. Guinneau, E. Codjovi, G. Bravic, D. Chasseau, and O. Kahn, J. Am. Chem. Soc. **119**, 10861 (1997)

[124] V. Ksenofontov, A. B. Gaspar, and P. Gütlich, Top. Curr. Chem. **235**, 23 (2004)

[125] A. Bousseksou, F. Varret, M. Goiran, K. Boukheddaden, and J.-P. Tuchagues, Top. Curr. Chem. **235**, 65 (2004)

[126] A. Hauser, Top. Curr. Chem. **234**, 155 (2004)

[127] A. Hauser, Chem. Phys. Lett. **124**, 543 (1986)

[128] S. Cobo, D. Ostrowskii, S. Bonhommeau, G. Molnár, L. Salmon, K. Tanaka, and A. Bousseksou, J. Am. Chem. Soc. **130**, 9019 (2008)

[129] P. Gütlich and A. Hauser, Angew. Chem. Int. Ed. **33**, 2024 (1994)

[130] J.-F. Létard, F. Guionneau, and L. Goux-Capes, Top. Curr. Chem. **235**, 221 (2004)

[131] J. Wajnflasz, Phys. Status Solidi **40**, 537 (1970)

[132] J. Wajnflasz and R. Pick, J. Phys. Colloq. **32**, C1 (1971)

[133] M. Nishino, K. Boukheddaden, Y. Konishi, and S. Miyashita, Phys. Rev. Lett. **98**, 247203 (2007)

[134] Y. Konishi, H. Tokoro, M. Nishino, and S. Miyashita, Phys. Rev. Lett. **100**, 067206 (2008)

[135] H. Spiering, Top. Curr. Chem. **235**, 171 (2004)

[136] R. Stoleriu, C. Enachescu, A. Stancu, and A. Hauser, IEEE Trans. Magn. **44**, 3052 (2008)

[137] C. Enachescu, R. Stoleriu, A. Stancu, and A. Hauser, Phys. Rev. Lett. **102**, 257204 (2009)

[138] S. W. Biernacki and B. Clerjaud, Phys. Rev. B **72**, 024406 (2005)

[139] E. Buhks, M. Bixon, and J. Jortner, J. Am. Chem. Soc. **102**, 2918 (1980)

[140] M. Sorai and S. Seki, J. Phys. Chem. Solids. **35**, 555 (1974)

[141] A. Bousseksou, J. McGarvey, F. Varret, J. A. Real, J.-P. Tuchagues, A. C. Dennis, and M. L. Boillot, Chem. Phys. Lett. **318**, 409 (2000)

[142] G. Molnár, V. Niel, A. B. Gaspar, J. A. Real, A. Zwick, A. Bousseksou, and J. J. McGarvey, J. Phys. Chem. B **106**, 9701 (2002)

[143] M. Sorai, Top. Curr. Chem. **235**, 153 (2004)

[144] D. M. A. Smith, M. Dupuis, E. R. Vorpagel, and T. P. Straatsma, J. Am. Chem. Soc. **125**, 2711 (2003)

[145] B. D. Alexander, T. J. Dines, and R. W. Longhurst, Inorg. Chem. **352**, 19 (2008)

[146] S. Schenker and A. Hauser, J. Am. Chem. Soc. **116**, 5497 (1994)

List of Publications

1. G. D'Avino, F. Terenziani and A. Painelli, *Aggregates of quadrupolar dyes: Giant two-photon absorption from, biexcitonic states*, J. Phys. Chem. B 110, 25590 (2006), letter.

2. G. D'Avino, A. Girlando, A. Painelli, M. H. Lemée-Cailleau and Z. G. Soos, *Anomalous dispersion of Optical Phonons at the Neutral-Ionic transition: Evidence from diffuse X-ray scattering*, Phys. Rev. Lett. 99, 156407 (2007).

3. F. Terenziani, G. D'Avino and A. Painelli, *Multichromophores for NLO: designing the material properties by electrostatic interactions*, ChemPhysChem 8, 2433 (2007), invited minireview.

4. G. D'Avino, L. Grisanti, J. Guasch, I. Ratera, J. Veciana and A. Painelli, *Bistability in Fc-PTM Crystals: The Role of Intermolecular Electrostatic Interactions*, J. Am. Chem. Soc, 130 (36), 12064 (2008), article.

5. L. Grisanti, G. D'Avino, A. Painelli, J. Guasch, I. Ratera and J. Veciana, *Essential State Models for Solvatochromism in Donor-Acceptor Molecules: The Role of the Bridge*, J. Phys. Chem. B, 2009, 113 (14), article.

6. G. D'Avino, L. Grisanti, A. Painelli, J. Guasch, I. Ratera and J.

Veciana, *Cooperativity from electrostatic interactions: understanding bistability in molecular crystals*, CrystEngComm, 2009, 11, 2040, invited highlight article.

Acknowledgements

First and foremost I wish to express my deep gratitude to my supervisor, Prof. Anna Painelli, for the constant and stimulating presence during this Ph.D. training.

I am grateful to all people of the Parma research team for fruitful collaborations and useful discussions: Prof. Alberto Girlando, Prof. Francesca Terenziani, Prof. Matteo Masino, Dr. Cristina Sissa and Dr. Luca Grisanti.

I wish to express my gratitude to all people I have collaborated with: Prof. Kamel Boukheddaden and François Varret of the University of Versailles UVSQ. Prof. Jaume Veciana, Dr. Imma Ratera and Dr. Judith Guasch of the ICMAB-CSIC of Barcelona. Prof. Zoltán G. Soos of Princeton University and Marie-Hélène Lemée-Cailleaux of ILL of Grenoble.

Finally I wish to thank the European Network of Excellence MAGMANet (NMP3-CT2005-515767) and the Italian MIUR (FIRB-RBNE01P4JF) for financial support.